Summer 2015

Computational Investigation of Pernicious Compounds: Arsenic and High Energy Density Materials and Their relevant Mechanisms

Lenora Kathleen Harper
Old Dominion University

COMPUTATIONAL INVESTIGATION OF PERNICIOUS COMPOUNDS: ARSENIC AND HIGH ENERGY DENSITY MATERIALS AND THEIR RELEVANT MECHANISMS

by

Lenora Kathleen Harper
B.S. Chemistry May 2009, Christopher Newport University

A Dissertation Submitted to the Faculty of
Old Dominion University in Partial Fulfillment of the
Requirements for the Degree of

DOCTOR OF PHILOSOPHY

CHEMISTRY

OLD DOMINION UNIVERSITY
August 2015

Approved by:

Craig A. Bayse (Director)

Patricia Pleban (Member)

Bala Ramjee (Member)

Marie Melzer (Member)

Lepsha Vuskovic (Member)

ABSTRACT

COMPUTATIONAL INVESTIGATION OF PERNICIOUS COMPOUNDS: ARSENIC AND HIGH ENERGY DENSITY MATERIALS AND THEIR RELEVANT MECHANISMS

Lenora Kathleen Harper
Old Dominion University, 2015
Director: Dr. Craig A. Bayse

The underlying mechanisms of chemical warfare agents (CWAs) and high energy density materials (HEDMs) are poorly understood, yet important to the development of chemical applications in military science and technology. The reactivity of arsenite and arsenic-based CWA lewisite with biological thiols plays an important role in toxicity of these elements. Toxic effects of arsenite are eliminated when arsenite and selenite are co-administered, due to their antagonistic relationship. The arsenic-based CWA lewisite is detoxified by the dithiol-containing British anti-lewisite (BAL). The reduction of arsenous acid by thiol, the formation of an As-Se species, and the detoxification of lewisite with BAL have been modeled using density functional theory (DFT) and solvent-assisted proton exchange (SAPE), a microsolvation technique that uses a network of water molecules to mimic the participation of bulk solvent in proton transfer processes. Several pathways were explored for the formation of an As-Se bond with the nucleophilic attack of selenide on $(RS)_2AsOH$ to form $(RS)_2AsSeH$ as the most likely, consistent with previous experimental studies. DFT-SAPE activation barriers for the two-step detoxification of lewisite with BAL predict rapid formation of a ring product, also observed experimentally.

The initial step in the decomposition of HEDMs is not yet understood due to the rapid rate at which the reaction takes place. Trigger bonds, or bonds that break to initiate explosive decomposition, were characterized using Wiberg bond indices (WBIs) for known HEDMs RDX, HMX, TNT, PETN, for comparison to recently-synthesized tetrazole-based explosives. WBIs were compared to reference compounds to determine the degree of weakening in bond strength (ΔWBI) to show that N-NO_2, C-NO_2, and O-NO_2 bonds are likely to cleave initially, consistent with previous experimental and theoretical results. Tetrazole-based molecules with small side chains and one –NO_2 group are predicted to have an N-NO_2 trigger bond. Larger side chains with one –NO_2 group are predicted to break in the C-N side chain backbone. Molecules with more than one –NO_2 will cleave at the C-N bond from tetrazole.

This dissertation is dedicated to my parents, Leonard and Tamrae Harper

ACKNOWLEDGMENTS

I would first like to thank my parents for all of their support. They taught me to trust God, work hard and always do the best I can, and to never give up. I am extremely grateful for all that you do and have done for me. I would like to thank Geoff for always keeping my head on my shoulders, making me laugh even through the hard times, and reminding me to never to be too hard on myself. My close friends Jessica, Bailey, Keith, and Katie have been a constant source of encouragement and my biggest cheerleaders. I would also like to thank my Jungle Gym family, who have supported and encouraged me along the way.

I would like to thank the Chemistry department at Old Dominion University for allowing me this opportunity. Alicia, Janice, Tammy, Valerie, and Kristi, you have always been very helpful and friendly throughout this process. Also, to my former labmates in Dr. Bayse's lab, Patricia (office mom) and Sonia, thank you for the encouragement and camaraderie throughout the years. I would like to thank my current labmate, Ashley, for constant support.

Finally, I would like to thank my committee members, Dr. Bala Ramjee, Dr. Patricia Pleban, Dr. Marie Melzer, and Dr. Lepsha Vuskovic. Most importantly, I would like to thank my advisor, Dr. Craig Bayse, for all of his guidance throughout the years.

TABLE OF CONTENTS

Page

LIST OF TABLES

LIST OF FIGURES

CHAPTER 1

INTRODUCTION

Chemistry in Military Applications

Chemistry is an important aspect in the development of military science and technology with a wide range of use from aeronautical to warfare applications. Research on chemicals such as explosives and propellants, also known as high energy density materials (HEDMs) and chemical warfare agents (CWAs) are instrumental in development of newer, safer materials which can be used for national security purposes.[3] It is important in the development of these types of pernicious compounds to understand the underlying mechanisms at the molecular level in order to develop new materials. Specifically, the mechanism which arsenic-containing compounds arsenite[4-6] and lewisite[7, 8] react with biomolecules remains unknown and the initial decomposition pathway upon detonation in explosives[9] is poorly understood. DFT is a computational tool that allows us to predict reaction barriers as well as other molecular properties accurately. It is ideal to use methods which do not require the handling of harmful chemicals and DFT allows us to study these systems safely. Therefore, in order to develop stable materials with greater efficacy, decomposition mechanisms of explosive materials need to be better understood. However, experimental mechanistic studies are limited by the explosive nature of the reaction.

This dissertation follows the format of *Chemical Research In Toxicology*.

Arsenic-based CWAs

CWAs are classified by their target organs/tissues and include nerve, vesicant, choking, blood, and vomiting agents; incapacitating psychochemicals; and lachrymators.[10] Vesicant agents, also known as blistering agents, cause eye, skin, and mucous membrane irritation and damage.[11] Common blistering agents including mustard gas (sulfur mustard) and several organic arsenicals, like lewisite, and methyl-, ethyl-, and phenyldichlorarsine (known as the "Dicks") were developed during World War I.[12] In 1915, the first major use of CWAs was conducted by the Germans at the Second Battle of Ypres, where massive quantities of chlorine gas was deployed to stop French advancements.[13] Arsenicals like lewisite, the "Dicks", and toxic arsenite are known to be harmful through physical contact or ingestion.[10, 14, 15] Arsenite, the most toxic form of arsenic, can cause various forms of cancer, hair loss, and skin lesions[14, 15] whereas lewisite causes physical burns and damage to mucous membranes in the lung, nose, eyes, and mouth.[10] Lewisite was discovered in World War-I and has the ability to affect a vast amount people with more severe injuries than other common CWAs, like sarin.[16] Lewisite, the more severe vesicant of all the organic arsenicals, is a blue-black dark colored liquid that has the smell of geraniums[11] (Figure 1).

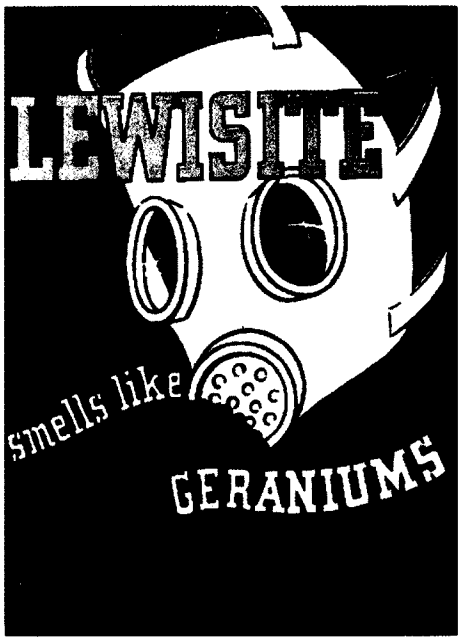

Figure 1. World War II identification poster of lewisite.

At the end of World War II, lewisite was rendered obsolete due to the development of the antidote, British Anti-Lewisite (BAL),[17-19] and several countries ordered the disposal of the deadly compound by either sea dumping or burial.[16] In 1945, United States' 925-ton stockpile stored in India was dumped in the Bay of Bengal, and an undetermined amount stored in Australia that same year was disposed of off Cape Moreton. From 1946-1948, an estimated 13,150 tons of lewisite was dumped in water a mile deep near Charleston, South Carolina. In 1958, 448 tons of lewisite was dumped west of the Gold Gate Bridge in California.[16] In 1957, the Chemical Corps Technical committee ordered that the remaining 3,000 tons of lewisite in stock in the United States be dumped in the sea. Other dumpsites in US waters were not only used to dispose lewisite, but other weapons of mass destruction (Figure 2).[20] However, many

countries have undocumented stockpiles and undetermined dump sites, where strict disposal regulations do not exist.[16] Proper disposal of CWAs is vital to environmental health and should be closely regulated due to potential disasters (i.e. leaching into water supply sources, accumulation in marine life, etc.). Chemical agents have to the ability to rapidly affect major population masses and are relatively inexpensive when compared to production of firearms and conventional artillery.[21]

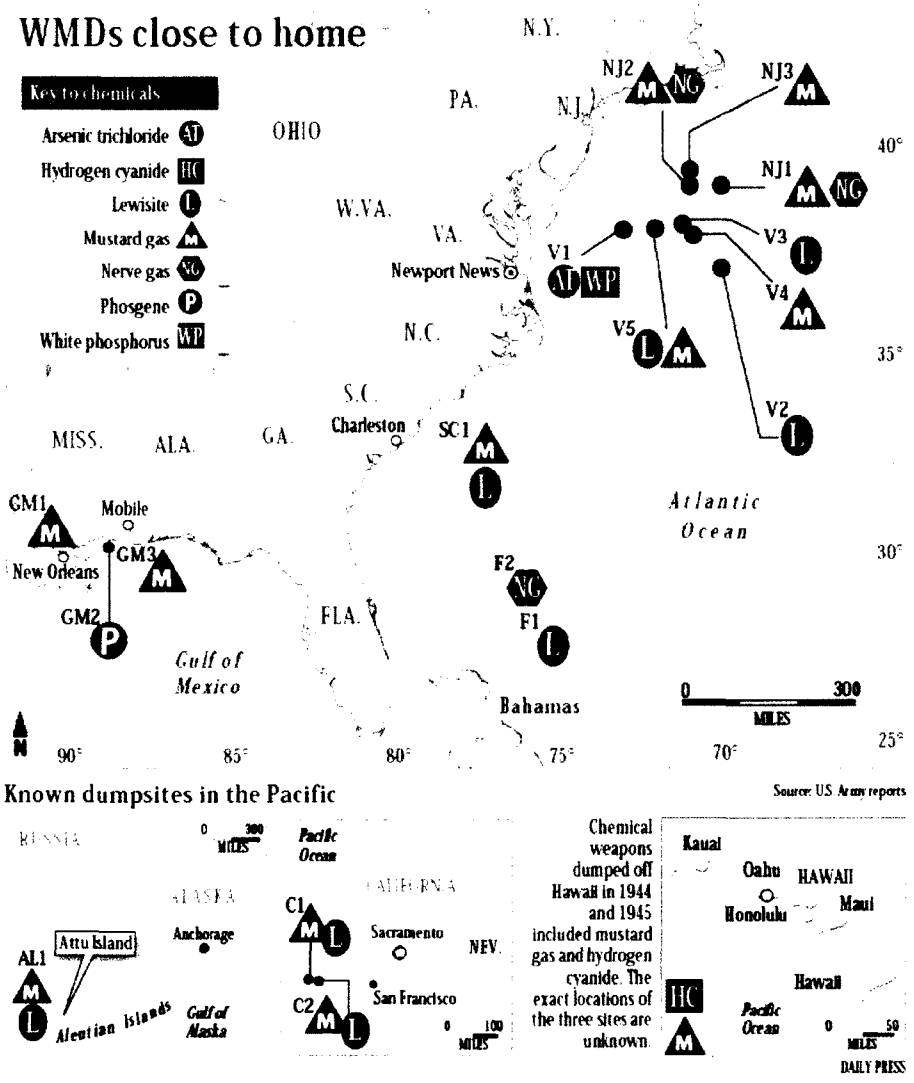

Figure 2. Known United States dumpsites for weapons of mass destruction.

In biological systems, arsenic is generally introduced to the body in the As(V) oxidation state as arsenate, where it is reduced to the As(III) oxidation state, arsenite.[22] From there, As(III) can react with sulfur-containing biomolecules and enzymes.[23, 24] For example, reactions between As(III) and glutathione reduces the concentration of the redox buffer that is responsible for cellular defense. Arsenite is also known to bind to Cys in proteins with potential inhibiting effects and dithiol-containing pyruvate dehydrogenase[25, 26] as well as zinc finger proteins.[27, 28] In the 1930s, an antagonistic effect was observed when arsenic and selenium were co-administered, but the otherwise toxic compounds are safely excreted.[29] Reduction of arsenite by-products can react with reduction of selenium by-products to form an experimentally determined non-toxic complex, seleno-bis-glutathionyl(sulfyl) arsinium ($[(GS_2)AsSe]^-$) ion, which was found in urine.[30] Lewisite binds to pyruvate dehydrogenase, an enzyme which participates in cellular respiration, and other dithiol-containing proteins near their active site.[7] BAL, the antidote discovered particularly for lewisite, is a simple dithiol compound that forms a nontoxic 5-membered ring with lewisite.[7, 19] In this work, the mechanism of the reduction of arsenous acid by methyl thiol, the formation of the As-Se complex, as well as the detoxification of lewisite using BAL is modeled using density functional theory.

Chemistry of Explosives

HEDMs are defined as compounds that contain high potential energy which exert excessive pressure and volumes of gases upon detonation.[31] These compounds

can be classified by their functional groups (i.e., nitro compounds, nitric esters, nitramines, azides) which contain oxygen and nitrogen components that will rearrange upon decomposition to form gaseous products. HEDMs can be grouped into three categories: (1) propellants, (2) primary explosives, and (3) secondary explosives.[31] A propellant burns to produce the gas required to propel an object (known as deflagration), whereas an explosive detonates and produces a shockwave of pressure that propagates through a material.[31] Primary and secondary explosives differ in sensitivities, where primary explosives (i.e., PETN) are much more sensitive to stimuli than secondary explosives (i.e., RDX and TNT). Primary explosive are also used to detonate secondary explosives which require a greater amount of energy to initiate decomposition.[31]

HEDMs are commonly used in ammunitions, fuel, and bombs in military applications. Around 2,000 years ago, the first explosive was discovered when the Chinese produced fireworks, which later would be modified to black powder, when developing signaling devices for military purposes.[32] In 1863, Alfred Nobel invented the blasting cap, which is still used in the US military today. The cap was a copper capsule which consisted of the primary explosive mercury fulminate and a fuse inserted into the end.[32] The invention paved the way for explosive technology. Currently, new compounds are being synthesized to enhance power, efficiency, and safety of these types of ammunitions. Commonly used HEDMs like 1,3,5-trinitro-1,3,5-triazacyclohexane (RDX), 1,3,5,7-tetranitro-1,3,5,7-tetrazacyclooctane (HMX), 2,4,6-

trinitrotoluene (TNT), and pentaerythritol tetranitrate (PETN) are components in several munitions used by the US military and are the basis for comparison for new explosives.

Explosives can be defined by properties such as oxygen balance (OB), heats of formation (HOF), heats of explosion (HOE), explosive power and power index (PI), detonation pressure and velocities, as well as impact and friction sensitivities.[31] The oxygen balance is the amount of oxygen gas that results from complete oxidation to form carbon dioxide, water, sulfur dioxide, etc. To calculate OB (Ω), a formula consisting of the number of carbon (a), hydrogen (b), nitrogen (c), and oxygen (d) atoms in the molecular formula and the explosive's molecular mass (*M*) is used (eq 1):

$$\Omega = \frac{\left[d-(2a)-\left(\frac{b}{2}\right)\right]x1600}{M} \quad (1)$$

A positive oxygen balance means that there is more oxygen than is required for complete oxidation, whereas a negative value means complete oxidation cannot take place due to a shortage of oxygen. If it is large and negative then the amount of oxygen for conversion to carbon dioxide is insufficient. As a result, toxic compounds such as carbon monoxide is released, a caveat in the development of commercial explosives. For example, RDX ($C_3H_6N_6O_6$; *M*=222; where a=3, b=6, c=6, and d=6) has an oxygen balance of -21.6%. If the oxygen balance is greater than -40.0%, then the decomposition products of the explosive reaction can be predicted based on the four steps of the Kistiakowsky-Wilson rules:[31]

1. Carbon atoms are converted to CO.
2. If any O remains, hydrogen is oxidized to form water.

3. If any O still remains, then CO is oxidized to CO_2.

4. N is converted to N_2.

For example, the overall decomposition reaction of RDX ($C_3H_6N_6O_6$) is (eq 2):

$$C_3H_6N_6O_6 \rightarrow 3\ CO + 3\ H_2O + 3\ N_2 \quad (2)$$

If energetic materials possess an OB lower than -40.0%, like TNT ($C_7H_5N_3O_6$, OB = -74.0%), the modified Kistiakowsky-Wilson rules are used to determine decomposition products:[31]

1. Hydrogen is converted to H_2O.

2. If any O remains, then C is oxidized to CO.

3. If any O still remains, then C is oxidized to CO_2.

4. N is converted to N_2.

Therefore, the overall reaction for TNT is (eq 3):

$$C_7H_5N_3O_6 \rightarrow 3½\ CO + 3\ H_2O + 3\ N_2 \quad (3)$$

Determination of decomposition products is required in order to calculate heats of formation, the total heat evolved when a substance completely oxidizes in excess oxygen. When oxidation is incomplete, as seen in TNT, the energy given off after detonation is termed the "heat of explosion." The heat of formation for all energetic materials should be negative, meaning the reaction is exothermic and will give off large amounts of heat.

The explosive power of energetic matter is a product of the volume of gas liberated upon detonation, *V*, and the heat of the explosion, *Q* (eq 4):

$$\text{Explosive power} = Q \times V \quad (4)$$

The power in relation to a standard explosive (std) is known as the power index (eq 5):

$$\text{Power Index} = \frac{Q_{HEDM} \times V_{HEDM}}{Q_{std} \times V_{std}} x\ 100 \quad (5)$$

TNT, RDX, HMX, and PETN have power indices of 116, 169, 169, and 167%, respectively, relative to picric acid. Another measure of explosive power is the detonation velocities (V_{det}) and pressure ($p_{C\text{-}J}$), where its power comes from the speed at which the shockwave propagates through an explosive and the pressure at the front of the shockwave, respectively. The impact and friction sensitivities are measurements of sensitivity of a compound subjected to external stimuli.

Although decomposition products of HEDMs can be predicted based on their molecular formula, the mechanism at which these compounds decompose remains unclear. Due to the nature of an explosion, the production of a shockwave front at supersonic speeds, experimental evidence of this bond breaking mechanism is lacking. Trigger bonds,[33] which initiate decomposition upon breaking, have been proposed[34] and studied thoroughly using computational methods which include calculating bond dissociation energies,[35] electron densities between two given atoms,[36, 37] as well as molecular dynamic simulations[38, 39] of a shockwave propagating through explosive materials. Computational measurements of bond strength are an important potential tool for characterizing trigger bonds. Understanding these mechanisms can lead to the development of more efficient and stable HEDMs. In this study, WBIs are calculated for the heavily investigated RDX, HMX, TNT, and PETN explosives to describe potential trigger bonds and to apply them to novel HEDMs to describe potential detonation pathways.

Computational Methods[40]

This dissertation uses density functional theory (DFT) as its basis for all theoretical calculations. DFT is a computational method used to describe the electronic structure and molecular properties (i.e. bond distances, atomic charges, etc.) of molecular systems. The energy of a system is calculated based on the Schrödinger equation (eq 6.1),

$$\hat{H}_{elec}\psi = E_{elec}\psi \tag{6.1}$$

where $\hat{H}$ represents the electronic Hamiltonian operator which consists of three terms: the electronic kinetic energy, the external potential energy acting on the system, and the electron-electron attraction (eq 6.2).

$$\hat{H}_{elec} = -\frac{\hbar^2}{2m}\sum_{i=1}^{N}\nabla_i^2 + \sum_{i=1}^{N}V(\mathbf{r}_i) + \sum_{i=1}^{N}\sum U(\mathbf{r}_i, \mathbf{r}_j) \tag{6.2}$$

The external potential energy ($\sum_{i=1}^{N}V(\mathbf{r}_i)$)is the interactions between the electrons and atomic nuclei (eq 6.3), where $\mathbf{r}_i$ is the position of electron i, and $\mathbf{R}_\alpha$ and Z_α are the position and charge of nucleus α, respectively :

$$V(\boldsymbol{r}_i) = -\frac{Z_\alpha}{|\mathbf{r}_i - \mathbf{R}_\alpha|} \tag{6.3}$$

The electronic Hamiltonian operator acts on a wavefunction ψ to return the original function, known as an eigenfunction, multiplied by a constant, the electronic energy of the system (E_{elec}). The Born-Oppenheimer approximation reduces the number of terms in the Hamiltonian based on the assumption that the nuclei are too heavy and slow to contribute significantly to the kinetic energy of the system; therefore, the kinetic energy of the nuclei and the nuclei-nuclei repulsion of the system can be

ignored. Solving the Schrödinger equation for many-electron systems is impossible; therefore, the Hartree-Fock method is used to approximate the energy of the system.

The Hartree-Fock (HF) method uses the variation method to obtain an approximate solution to a multi-electron Hamiltonian using a single Slater determinant as the wavefunction. The electron wavefunction describing the set of electrons is generalized as (eq 7),

$$\Psi(\vec{r}_1, S_{z1}, \vec{r}_2, S_{z2}, \ldots, \vec{r}_i, S_{zi}, \ldots, \vec{r}_I, S_{zI}) \tag{7}$$

where $\vec{r}_i$ is the position of the electron number i, S_{zi} is spin in z direction, and I is the total number of electrons. HF approximates Ψ in terms of a set of single-electron functions, known as "orbitals" or "spin orbitals". The wave function ψ can be written as a Slater determinant, which is the sum of the $I!$ Hartree products with their single-electron functions in a different order. In order to obtain energies with small error, electron correlation must be included through multireference methods or post-Hartree-Fock methods such as configuration interaction (CI), coupled cluster (CC), Møller-Plesset perturbation theory (i.e. MP2). These methods are able to recover much of the electron correlation, but are computationally expensive.

DFT has the accuracy of post-HF methods and is less expensive. DFT is based on the electron probability density (ρ) function, whereas HF is dependent on the molecular wavefunction. Based on the Kohn-Sham (KS) theory, DFT approximates the electron density in terms of molecular orbitals (MOs) and treats the exchange-correlation energy functional ($E_{xc}[\rho]$), a term previously ignored in the HF method. Therefore, the ground-state electronic energy (E_0) of a system is described in eq 8.1.

$$E_0 = \int \rho(\mathbf{r})v(\mathbf{r})d\mathbf{r} + \bar{T}_s[\rho] + \frac{1}{2}\iint \frac{\rho(\mathbf{r}_1)(\mathbf{r}_2)}{r_{12}} d\mathbf{r}_1 d\mathbf{r}_2 + E_{xc}[\rho] \quad (8.1)$$

The first three terms describe the potential energies of the electron-nuclei attraction, kinetic energy of noninteracting electrons, and electrostatic repulsion between electrons, respectively, which collectively contribute largely to the total energy of the system. The last term, $E_{xc}[\rho]$ (eq 8.2), is comprised of the kinetic ($\Delta\bar{T}$) and coulombic correlation energies ($\Delta\bar{V}_{ee}$), exchange energy, and the self-interaction energy.

$$E_{xc}[\rho] = \Delta\bar{T}[\rho] + \Delta\bar{V}_{ee}[\rho] \quad (8.2)$$

Good approximation of the otherwise unknown exchange-correlation energies are required to get an accurate total energy of the system. The $E_{xc}[\rho]$ can be calculated with two different types of functionals, Local Density Approximations (LDA) or Generalized Gradient Approximations (GGA).

LDA is based on the notion that the electron density probability does not is uniformly distributed, so it can be solved using eq 9.1,

$$E_{xc}^{LDA}[\rho] = \int \rho(\mathbf{r})\varepsilon_{xc.}(\rho)\, d\mathbf{r}, \quad (9.1)$$

where $\varepsilon_{xc.}$ is the exchange ($\varepsilon_{x.}$) and correlation ($\varepsilon_{c.}$) energy for each electron, which is written (eq 9.2):

$$\varepsilon_{xc}[\rho] = \varepsilon_x(\rho) + \varepsilon_c(\rho) = -\frac{3}{4}\left(\frac{3}{\pi}\right)^{\frac{1}{3}}(\rho(\mathbf{r}))^{1/3} + \varepsilon_c^{VWN}(\rho) \quad (9.2)$$

The ε_c^{VWN} is a known, complicated function developed by Vosko, Wilk, and Nusair (VWN).[41] An improvement to LDA is the local-spin-density approximation (LSDA), which allows separate spatial HF orbitals for electrons with opposite spins (LDA treats the

paired electrons with the same KS orbitals). LSDA is a good functional for open-shell systems and molecules near dissociation (following reaction coordinates).

The GGA functionals are used to describe position of electron density, the term neglected both in LDA and LSDA. The GGA exchange-correlation energy, E_{xc}^{GGA}, can be solved using eq 10.1.

$$E_{xc}^{GGA}[\rho^{\alpha},\ \rho^{\beta}] = \int f\left(\rho^{\alpha}(\mathbf{r}),\ \rho^{\beta}(\mathbf{r}),\ \nabla\rho^{\alpha}(\mathbf{r}),\ \nabla\rho^{\beta}(\mathbf{r})\right) d\mathbf{r} \qquad (10.1)$$

The exchange-correlation energy obtained using GGA is a correction to LSDA, where the electron density of α and β-spin electrons are treated separately, similar to the exchange and correlation functionals (eq 10.2).

$$E_{xc}^{GGA} = \mathrm{E_x^{GGA}} + \mathrm{E_c^{GGA}} \qquad (10.2)$$

For example, the commonly used BLYP functional is comprised of Becke's 1988 (B) exchange functional[42] with Lee-Yang-Parr's (LYP) correlation functional[43]. Meta-GGA functionals, dependent on the second derivatives of electron density versus the first derivative in GGA functionals, can also be used to calculate $E_{xc}$and give more accurate results, but require more computational time. Hybrid functionals, like B3LYP,[44] is defined the HF exchange functional, E_x^{HF}, and the GGA LYP correlation functional. These types of functional give good geometries, vibrational frequencies, and dipole moments.

In either HF or DFT, the molecular orbitals that contribute to the wavefunction or density are built up as linear combination of atomic orbitals. Atomic orbitals are represented by basis functions, χ_s, that can be grouped to form the basis set. Two types of basis functions discussed here are Slater-Type Orbitals (STOs) and Gaussian-Type Orbitals. STOs are exponential functions similar to the solutions of the hydrogenic atom,

but multicenter two-electron integrals are computationally expensive. To speed up calculation time, Boys[45] proposed using Gaussian-Type Orbitals (GTOs) in place of STO because multicenter two-electron integrals can be simplified to two-center integrals, requiring less computational time. Several GTOs are required to represent one STO because GTOs do not represent the sharp cusp at the nucleus like STOs. GTOs also approach zero more quickly as the distance from the nucleus increases. Additional GTOs are used to correct these problems, with less computational expense that a single STO.

Minimal basis sets are described using only one Gaussian function to represent both the core electrons and valence electrons. These types of basis sets are used as rough estimates, but are not publication-quality. Basis sets that have more than one Gaussian functions on valence orbitals are called double-, triple-, quadruple-zeta basis sets. Pople[46] developed a split-valence basis set which takes the form of X-YZG. X is the number of primitive Gaussian functions on core electrons, and Y and Z tell us two basis functions for each valence orbital is used. For example, 3-21G is a double-zeta split valence basis set that has three GTOs for core orbitals and the valence orbitals are split into two functions with two and one primitive Gaussian orbitals. Diffuse functions, which allow AOs to change upon molecular formation, can be added to basis set and are denoted with a (+). To add diffuse functions to hydrogen atoms, a (++) is used.[47] Polarization functions, added GTO functions to the maximum *l* quantum number, allow AOs to become distorted with shifts in charge during the formation of molecules.[48] For example, C has an *l*=1; therefore, a functional is added to the *l*=2 orbital, known as the d orbital. Polarization functions added to heavy atoms is marked with an (*) and to add to

hydrogen as well, a (**) is written. So, 3-21++G** is a double zeta split valence basis set with diffuse and polarization functions added to all atoms on the system.

Dunning developed the correlation-consistent (cc) basis set, designed for calculations involving electron correlation.[49] These basis sets are written using the cc-pVNZ, which stands for the correlation-consistent, polarized valence double-, triple-, quadrupole-, etc. zeta. To add additional diffuse and polarization functions, the prefix *aug-* should be used (i.e., aug-cc-pVDZ). Alhrich's TZVP basis set is a triple zeta basis set and diffuse functions can be added using (+) (TZVP+).[50]

CHAPTER 2

THIOL REDUCTION OF ARSENITE: DFT MODELING OF THE PATHWAYS TO AN AS-SE BOND

Introduction

Arsenic and selenium compounds are important naturally occurring environmental toxicants.[4,5,51, 52,53] The United States Environmental Protection Agency has set maximum contaminant levels for arsenic and selenium at 10 and 50 ppb for drinking water, respectively.[54] Consumption and inhalation of arsenic through contaminated drinking water and industrial by-products have been shown to increase the risk of neuropathy; skin lesions; and cancers of the skin, lung, and bladder.[15,14] Ingestion of significant amounts of selenium, an essential trace element, results in gastrointestinal complications, hair and nail loss, as well as central nervous system damage.[55] Arsenic and selenium can assume inorganic and organic forms which exist mainly in two oxidation states: As(III) and As(V), and Se(IV) and Se(VI). Arsenate (As(V)) and selenate (Se(VI)) species are found in well-oxygenated surface waters, whereas arsenite (As(III)) and selenite (Se(IV)) are observed in ground water.[56,57] As(III), the most toxic arsenic species[58] (LD_{50} of AsO_3^{3-} – 34.5 mg/kg),[4] is 10 times more toxic than arsenate and 70 times more toxic than organic methylated arsenic.[56] Se(IV) (LD_{50} of Na_2SeO_3 – 5 mg/kg), has been determined to be several times more toxic than selenoethers[55] such as

---

Adapted with permission from (Harper, L. K.; Antony, S.; Bayse, C. A. Thiol reduction of arsenite and selenite: DFT modeling of the pathways to an As–Se bond. *Chem. Res. Toxicol.* **2014**, *27* (12), 2119-2127). Copyright 2015 American Chemical Society.

selenomethionine.[59] Interactions of arsenite and selenite with sulfhydryl-containing biomolecules are key factors in their toxicity.[6,60,61] Formation of reactive oxygen species (ROS) from reactions between selenite/arsenite and gluthathione (GSH) cause DNA damage, which can trigger carcinogenesis.[62] Other modes of toxicity for both selenium and arsenic compounds include reactions involving proteins: selenite inhibits the activity of zinc finger transcription factors TFIIIA, Sp1 and AP1[63] and arsenite inhibits the DNA damage-repairing protein poly(ADP-ribose) polymerase-1 (PARP-1).[64-66,67] Arsenite and selenite also release Zn^{2+} from metallothionein (MT),[68] xeroderma pigmentosum group A (XPA)[27, 28, 69] and formamidopyrimidine-DNA glycolyase (Fpg),[27, 28, 69] and disrupt the function of pyruvate dehydrogenase,[25, 26] glutathione reductase,[70] and thioredoxin reductase.[71] As(III) and Se(IV) can deplete GSH, an essential redox buffer that plays a critical role in cellular defense and is found in high concentrations in cells.[72] The reaction of selenite with GSH forms selenopersulfide ($HSSe^-$) which promotes cell death in various cancer cell lines.[25,71] Arsenic is most likely introduced to the body as As(V) where it is reduced by arsenate reductase (ArsC),[22] human glutathione-S-transferase ω (hGST-01),[23] or available thiols (RSH)[24] to produce arsenite. Arsenite can then disrupt cellular defense mechanisms by reacting with up to three equivalents of RSH to form $As(SR)_3$ **4** (eq 11). According to Delnomdedieu et al., $As(SG)_3$ is stable from pH 1.5 to 7.5 and readily forms under physiological conditions.[73] Similarly, selenite **5** reacts with four equivalents of thiol (eq 12) to produce selenotrisulfide **9** (RSSeSR) which is further reduced to selenide **11** (Se^{2-}) by thiols (eq 13) including thioredoxin[74, 75] or glutathione reductase.[76]

$$As(OH)_3 + 3RSH \rightarrow As(SR)_3 + 3H_2O \quad (11)$$

$$Se{=}O(OH)_2 + 4RSH \rightarrow Se(SR)_2 + 4H_2O + 2RSSR \quad (12)$$

$$Se(SR)_2 + 2\ RSH \rightarrow H_2Se + 2RSSR \quad (13)$$

In the 1930s, Moxon and DuBois first observed an antagonistic relationship between selenium and arsenic when selenium toxicity decreased in rats exposed to As(III)-laced drinking water.[29] Further studies by DuBois et al. determined that As(III), in the form of $NaAsO_2$, protected against liver damage caused by seleniferous wheat and Se(IV).[77] Later, Levander and Argrett found that arsenite inhibited the excretion of dimethylselenide[78] which was replaced by an arsenic-selenium-glutathione species in rat bile.[79] Conversely, selenite increased gastrointestinal excretion of arsenic.[80] When excess arsenite was present in vitro, selenite formation by glutathione reductase was indirectly inhibited by the formation of an As-Se by-product of arsenite and selenite reduction.[81] Based on this finding, Gailer et al. synthesized the As-Se complex ion **17**$^-$ (selenobis(S-glutathionyl)arsinium $[(GS)_2AsSe]^-$) from Se^{2-} and $(GS)_2AsOH$ **3** under physiological conditions, and characterized the compound using X-ray absorption spectroscopy.[1, 30]

In order to understand the mechanisms of arsenic and selenium toxicity and their antagonistic relationship, density functional theory (DFT) and solvent-assisted proton exchange (SAPE) were used to model the mechanisms for (1) the reaction of arsenous acid $As(OH)_3$ and selenious acid $SeO(OH)_2$ with thiols and (2) formation of the arsenic-selenium species $(RS)_2AsSe^-$. SAPE is a method of microsolvation that models proton exchange by connecting the protonation and deprotonation sites with a network of

water molecules. The indirect proton transfer in these models is an approximation of the role of bulk solvation and avoids the strained transition states and high activation barriers found in gas phase models. Previous studies have utilized SAPE modeling to determine redox mechanisms of biologically-relevant selenium compounds,[82] the oxidation and disulfide formation of cysteine,[83] the decomposition of thiosulfuric acid,[84] the tautomeric proton transfer of biologically relevant heterocyclic compounds[85] as well as other mechanisms requiring proton exchange with excellent agreement with experimental data.

Computational Methods

Geometry optimizations of the reaction of $As(OH)_3$ and $SeO(OH)_2$ by methyl thiol were performed in Gaussian03[86] and Gaussian09[87] using the mPW1PW91[88] functional. Arsenic, oxygen, and all hydrogens connected to non-carbon heavy atoms or involved in the SAPE network were represented by the Dunning split-valence triple-ζ basis set with polarization functions (TZVP).[89] The Ermler-Christiansen relativistic effective core potential (RECP) basis set was used for the Se atom.[90] Sulfur was represented by the Wadt-Hay RECP basis set.[91] These basis sets were augmented with diffuse *s*-, *p*-, and d-type (Se and As only) functions. A double-ζ basis set was employed with polarization functions on hydrocarbon fragments.[92] Two SAPE networks were used in this study. In network 1 (Scheme 1), water molecules are positioned in a square cluster and form a hydrogen bonding network to connect the thiol proton and the leaving –OH group to provide a pathway for proton transfer (network 1, Scheme 1). The square SAPE network

reduces strain introduced in smaller network sizes and is small enough to manually search for the most favorable conformation.[82] For steps in which the leaving group is sulfur or arsenic, longer distances are required between the sites involved in proton transfer, and an open three-water SAPE network is utilized (network 2, Scheme 1).

Scheme 1. SAPE models used in DFT calculations.

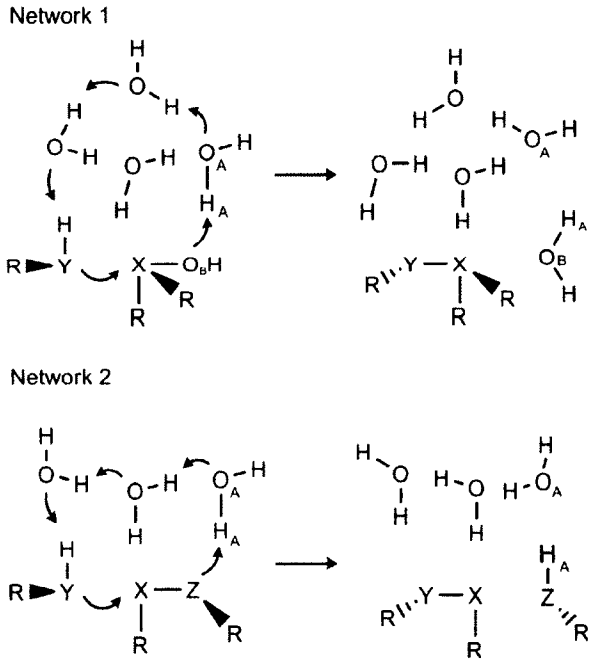

Transition states were found either by a manual scan of the selected reaction coordinate followed by a full optimization of the initial guess or by using a quadratic[93] Synchronous Transit-Guided Quasi-Newton (STQN) Method (QST3 in Gaussian09).[94] Each transition state was found to have one imaginary frequency along the appropriate reaction coordinate. Reported energies include zero-point energy (ZPE), thermal, and

entropic corrections. Polarizable continuum models (PCM)[95] using Bondi atomic radii[96] were employed for bulk solvation corrections for water.

Results and Discussion

DFT-SAPE models of the mechanism of the reactions of $As(OH)_3$ and $SeO(OH)_2$ with MeSH (Scheme 2) are discussed first, followed by possible pathways for As-Se bond formation. The stationary points (reactant complex (R), transition state (TS), or product complex (P)) for each pathway are labeled by mechanistic step (for example, **1→2$_{TS}$** is the transition state for the conversion of **1** to **2**). In the following discussion, activation barriers and reaction energies are reported as the solvation-corrected Gibbs free energy ($\Delta G+\Delta G_{sol}$) unless otherwise noted.

Scheme 2. Mechanisms for the reduction of (a) arsenate and (b) selenite. RSH represents glutathione or other available thiol.

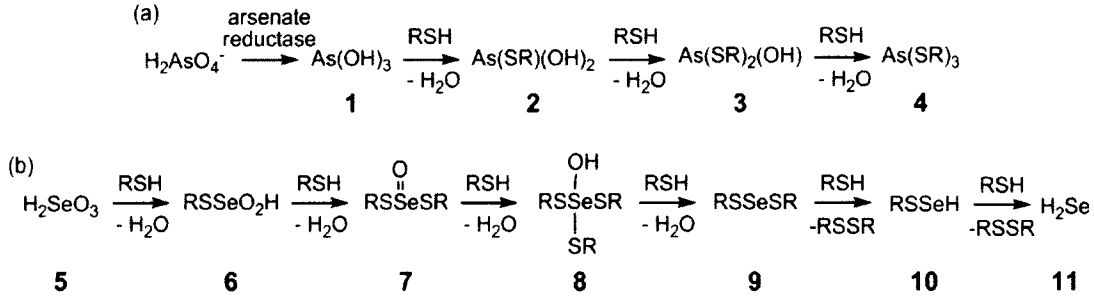

Reduction of $As(OH)_3$ to $As(SR)_3$ (**1→2→3→4**). The conversion of **1** to **4** was modeled as the sequential S_N2-like nucleophilic attack of three equivalents of MeSH on

the As center eliminating a water molecule at each step. Proton transfer from the thiol to the leaving water is facilitated by four-water SAPE network 1 (scheme 1) and occurs in tandem with As—S bond formation. Each additional sulfur bonded to the arsenic center of **1-3** decreases the partial positive charge on As (q_{As}(**1**)=1.49e, q_{As}(**2**)=1.25e, q_{As}(**3**)=1.02e). As a result, the As···S interaction with the thiol in the reactant complexes increases by 0.1 Å from **1**→$\mathbf{2}_R$ to **2**→$\mathbf{3}_R$ due to the lower As partial charge, but decreases by 0.1 Å in **3**→$\mathbf{4}_R$ due to softening of the arsenic center in **3** (Figure 3). From these reactant complexes, transition states were found by stretching O_A-H_A bond in the water molecule present at the site of protonation of the reactant (scheme 1). The increase in activation barriers (Table 1) from **1**→**2** (+20.0 kcal/mol) to **2**→**3**(+21.7 kcal/mol), correlates to the change in the As partial charge; however, the decrease in barrier height in step **3**→**4** by 5.0 kcal/mol is associated with the greater affinity of **3** for a soft nucleophile. The high barriers for steps **1**→**2** and **2**→**3** are consistent with the experimental studies in which the reaction temperature had to be increased to 37°C in order to speed the production of $As(SR)_3$.[97] DFT As-S bond distances for **3**→$\mathbf{4}_P$ ((2.26 and 2.27 Å) are comparable to XAS values obtained by Miot et al (2.25 Å).[98] The formation of **2** (-13.3 kcal/mol) and **4** (-16.7 kcal/mol) is more exergonic than the formation of **3** (-10.4 kcal/mol), suggesting that **3** will not be a stable intermediate. Similarly, Suzuki et al. performed *ab initio* calculations on the reaction between thioarsenates and thiols at 37°C and found the first attack of thiol on $As{=}S(CH_3)(OH)$ to be the driving force in the reaction based on ΔH (-4.85 kcal/mol).[99]

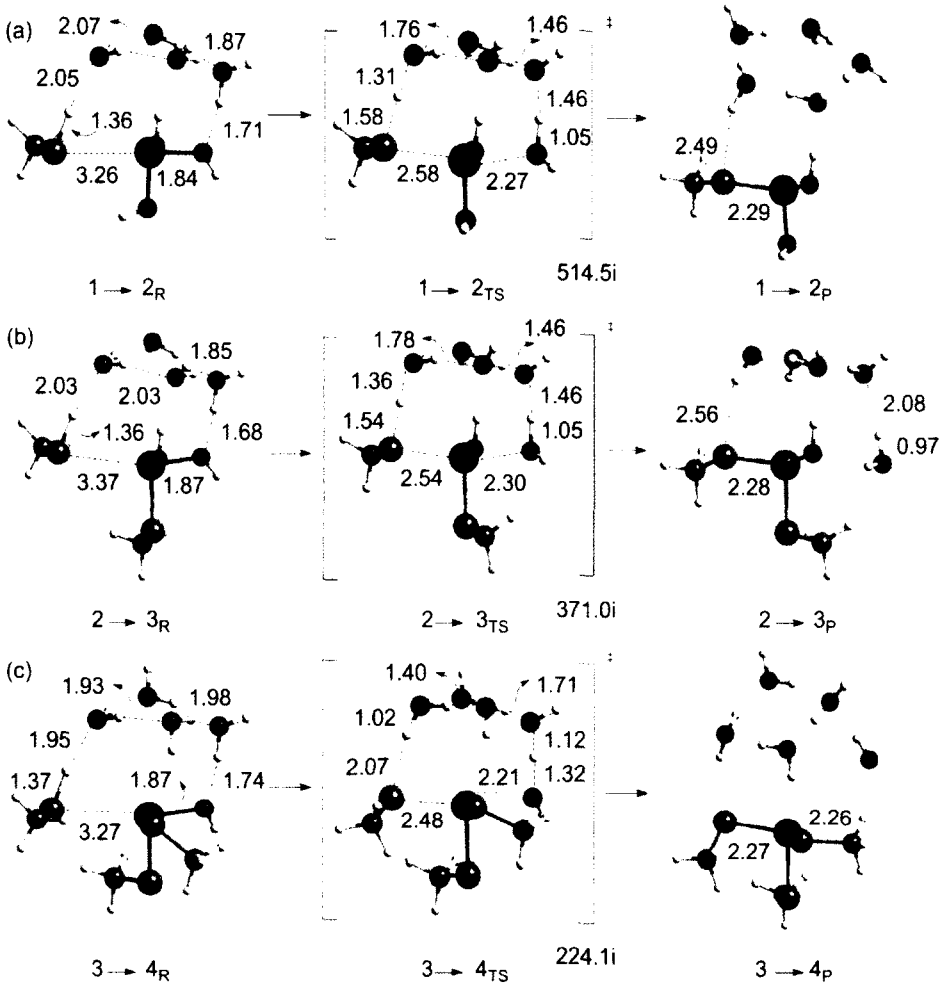

Figure 3. Selected bond distances (Å) for the three steps involved in the reduction of arsenous acid by methyl thiol ((a) 1→2, (b) 2→3, and (c) 3→4). Imaginary vibrational modes are listed for each transition state structure.

Table 1. Relative DFT(mPW1PW91) energies for the three-step reduction of arsenous acid by methyl thiol (**1**→**2**, **2**→**3**, **3**→**4**).

Reaction		TS	Product
1→**2**	ΔH	11.1	-13.3
	ΔG	16.9	-14.5
	$\Delta G + \Delta G_{solv}$	20.0	-14.9
2→**3**	ΔH	9.2	-10.4
	ΔG	17.5	-7.2
	$\Delta G + \Delta G_{solv}$	21.7	-1.8
3→**4**	ΔH	6.8	-16.7
	ΔG	14.4	-16.3
	$\Delta G + \Delta G_{solv}$	16.7	-16.8

Several studies have attempted to detect arsenic-GSH intermediates in biological media such as blood, bile and urine (pH 8.0).[100] $As(SG)_3$ was recovered with a half-life of 20 minutes in bile.[101] Similar results were found in a study by Spuches et al[97] where near-UV absorption spectroscopy and isothermal titration calorimetry were used to determine the thermodynamics of As-thiol interactions. Stability constants (K) were calculated for each step in the sequential attack of thiol on As to form a 1:3 As-GSH complex. The value of K increases with each addition of GSH (K_1=20, K_2=430, K_3=1.2×10^3), indicating that the stability of the intermediates are at least an order of magnitude less stable than the final product. Our calculated activation energies suggest steps **1**→**2** (+20.0 kcal/mol) and **2**→**3** (+21.7 kcal/mol) are slower than the formation of product **4** (+16.7 kcal/mol) and will produce intermediates (ΔH=-13.3 kcal/mol, **1**→**2**$_P$;

ΔH=-10.4 kcal/mol, **2→3$_P$**) which could react readily with sulfur-containing biomolecules.

Reduction of $Se(SMe)_2$ to H_2Se (**9→10→11**). The reduction of selenious acid (**5**) with thiols to produce selenotrisulfide **9** (**5→6→7→8**) was performed by Sonia Antony.[102] The first four steps in the reaction of selenious acid (**5**) with thiols have low activation barriers with the formation of selenurane **8** as the rate determining step (Table 2). Selenurane is unstable and is further reduced to stable product, selenotrisulfide **9** (**8→9**). Selenotrisulfide **9** can react with two more equivalents of thiol to be fully reduced to **11**. The first step of this stepwise reaction is the nucleophilic attack of thiol on **9** to form MeSSeH **10** (Figure 4a) which then reacts with a second equivalent of thiol to form **11** (Figure 4b). The three-water SAPE network 2 is used to facilitate proton transfer in reactant complexes **9→10$_R$** and **10→11$_R$** (Scheme 1). In these reactant complexes, MeSH is positioned properly for nucleophilic attack as evidenced by the nearly linear S···S–Se bond angles (173.3° and 173.7°, respectively), which are comparable to the S···S–Se bond angle (172.9°) in models of the reduction of PhSeSMe to PhSeH by MeSH.[82] The high activation barriers for **9→10** and **10→11** (+19.0 kcal/mol and + 19.9 kcal/mol, resp.), which are similar to those for the reduction of selenenyl sulfide by thiol (+21.7 kcal/mol[82]), suggests that formation of **10** and **11** will take place slowly. The endergonicity of these reactions (+7.2 kcal/mol and +1.4 kcal/mol, resp.), suggests that **9→10** and **10→11** are reversible processes that will be driven to completion by excess thiol.

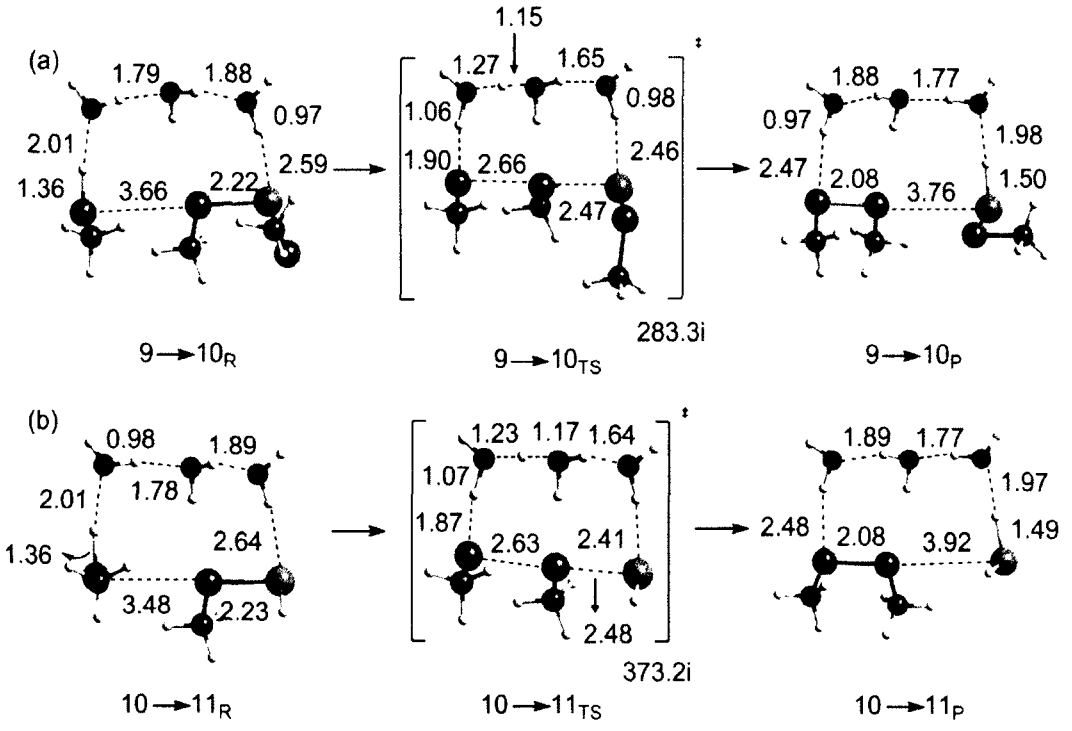

Figure 4. Selected bond distances (Å) for the formation of selenide ((a) 9→10 and (b) 10→11). Imaginary vibrational modes are listed for each transition state structure.

Table 2. Relative DFT(mPW1PW91) energies (kcal/mol) of the four mechanistic steps involved in the reaction of selenious acid with methyl thiol (**5→6**, **6→7**, **7→8**, **8→9**) and the formation of selenide (**9→10**, **10→11**).

Reaction		TS	Product
5→6	ΔH	2.8	-22.2
	ΔG	5.8	-23.9
	$\Delta G + \Delta G_{solv}$	6.2	-24.7
6→7	ΔH	1.1	-15.4
	ΔG	5.3	-15.7
	$\Delta G + \Delta G_{solv}$	6.6	-16.0
7→8	ΔH	11.4	0.0
	ΔG	19.4	4.7
	$\Delta G + \Delta G_{solv}$	19.2	3.8
8→9	ΔH	4.7	-39.8
	ΔG	8.6	-44.1
	$\Delta G + \Delta G_{solv}$	7.8	-43.9
9→10	ΔH	17.2	7.8
	ΔG	24.4	8.3
	$\Delta G + \Delta G_{solv}$	19.0	7.2
10→11	ΔH	13.9	1.8
	ΔG	20.6	1.6
	$\Delta G + \Delta G_{solv}$	19.9	1.4

Formation of the arsenic-selenium complex

The antagonistic biological relationship between arsenic and selenium has been traced to the formation of an arsenic-selenium species $[(GS)_2AsSe]^-$ which can be safely excreted.[30] Gailer et al.[1] investigated two possible mechanisms for the coupling of As(III) and Se(IV) originally proposed by Seko et al (Scheme 3).[103] In pathway A (Scheme 4), six equivalents of GSH convert **5** to **11**, which reacts with **3** to form **17**. The second proposed mechanism (pathway B, Scheme 4) combines **3** with selenopersulfide **10** to

form methylthioseleno-bis(S-methylthionyl) arsenite **16**, followed by thiol reduction to **17**. Seko et al.'s mechanisms involve intermediates in the arsenic reduction mechanism, but the DFT-SAPE activation energies for this pathway (**1**→**2**→**3**) are relatively high (*vide supra*), indicating that the formation of intermediates **2** and **3** will take place slowly allowing available arsenous acid to react with the stronger H_2Se nucleophile. Therefore, a third mechanism is considered in which **1** and **11** form **12**, followed by thiol reduction to **17** (pathway C, Scheme 4). To investigate other possible competing pathways to **17**, the nucleophilic attacks of **10** on **1** (**1+10**→**14**, pathway D) and **2** (**2+10**→**15**, pathway E), and **11** on **2** (**2+11**→**13**, pathway F) were also modeled (Scheme 4). SAPE models (Figures 4-9) for the As-Se bond formation steps were constructed using the water networks shown in scheme 1.

For pathway A (**3+11**→**17**), the nucleophilic attack of **11** on **3** to form the As-Se bond in **17** was modeled using SAPE network 1 to aid proton transfer (Figure 5). The one-step exergonic reaction **3+11**→**17** (-19.8 kcal/mol) has a lower activation barrier (+8.6 kcal/mol) than **3+10**→**16** below (+10.8 kcal/mol) due to the greater nucleophilicity of **11**. The Se-As (2.42 Å) and As-S (2.26 and 2.25 Å) bond distances calculated for **17** in **3+11**→**17**$_P$ are comparable to experimental bond lengths ($d_{As\text{-}Se}$=2.39 Å, $d_{As\text{-}S}$=2.25 Å) obtained for $[(GS)_2AsSe]^-$ from EXAFS. The As-Se stretching frequency is slightly higher (311 cm^{-1}) than that reported for $[(GS)_2AsSe]^-$ (290 cm^{-1}).[30]

Scheme 3. Proposed mechanisms by Gailer et al[1] for the biological formation of an As-Se bond.

(a) $(GS)_2AsOH + HSe^- \longrightarrow [(GS)_2AsSe]^- + H_2O$

(b) $(GS)_2AsOH + GSSe^- \longrightarrow (GS)_2AsSeSG + OH^-$

$(GS)_2AsSeSG + GSH \longrightarrow [(GS)_2AsSe]^- + GSSG + H^+$

Scheme 4. Proposed mechanisms for the biological formation of an As-Se bond.

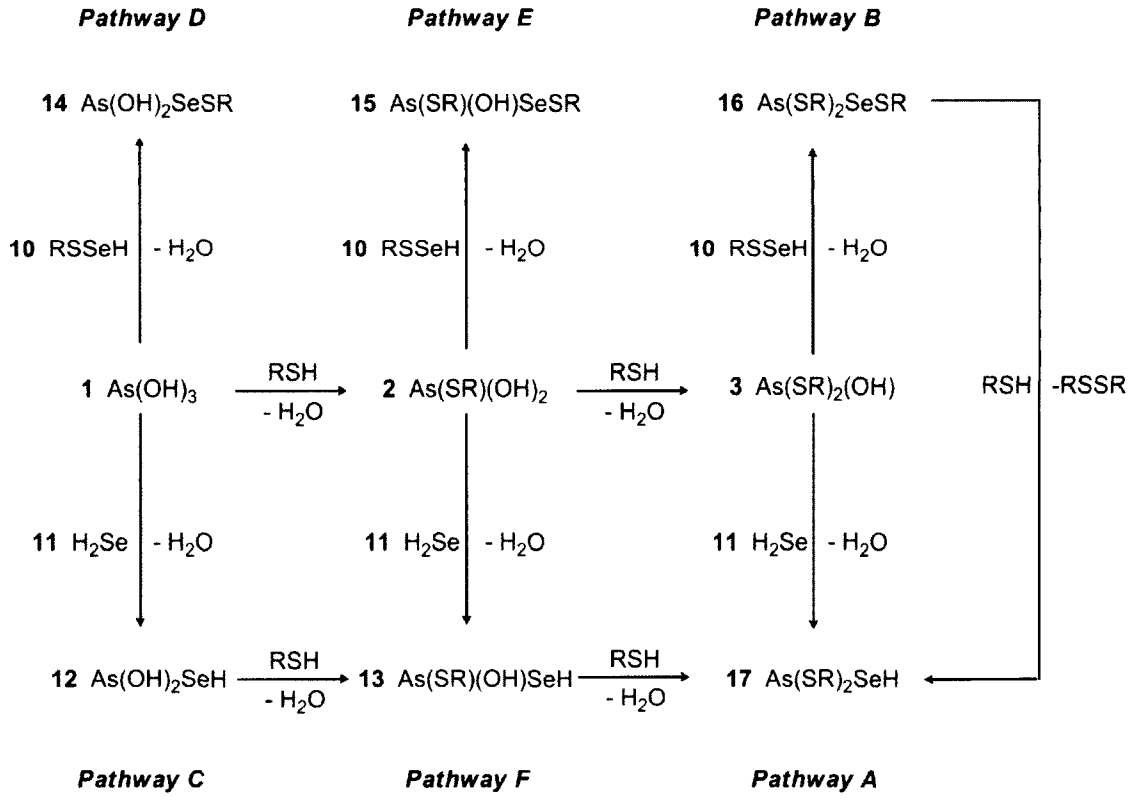

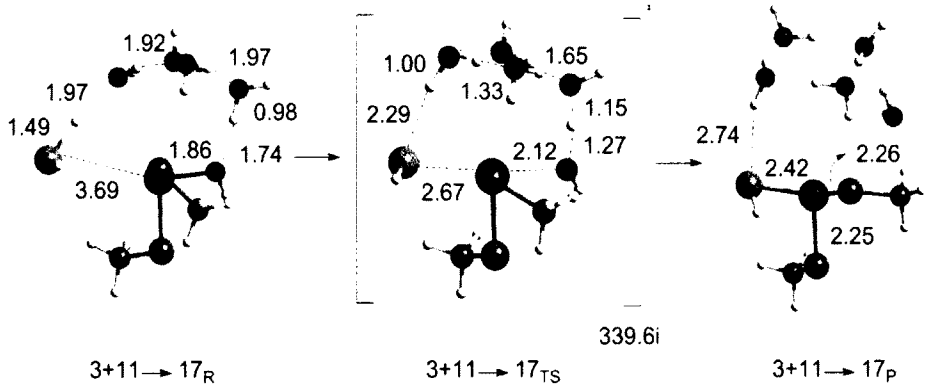

Figure 5. Selected bond distances (Å) for pathway A (3+11→17). The imaginary vibrational mode is listed for the transition state structure.

Pathway B (**3+10→16→17**) was modeled as the nucleophilic attack of **10** on **3** to form **16**, followed by thiol reduction to form **17** (Figure 6) using SAPE network 1 for **3+10→16** and network 2 for **16→17**. The activation energy for the exergonic reaction (-21.0 kcal/mol) between **3** and **10** is relatively low (+10.8 kcal/mol) compared to the barrier for **1+10→14** (+15.0 kcal/mol) due to the greater affinity of the soft arsenic center of **3** for the soft nucleophile **10.** The high barrier for step **16→17** (+21.9 kcal/mol) is consistent with those calculated for other disulfide bond formation reactions (e.g., **9→10** (+19.0 kcal/mol), **10→11** (+19.9 kcal/mol) and the reduction of a selenenyl sulfide to selenol in the glutathione peroxidase-like cycle of benzeneselenols (+21.7 kcal/mol)[82]). The formation of **17** (**16→17**$_P$, +2.4 kcal/mol) is likely stabilized under biological conditions by hydrogen bonding to the GSH backbone and deprotonation to **17**$^-$.

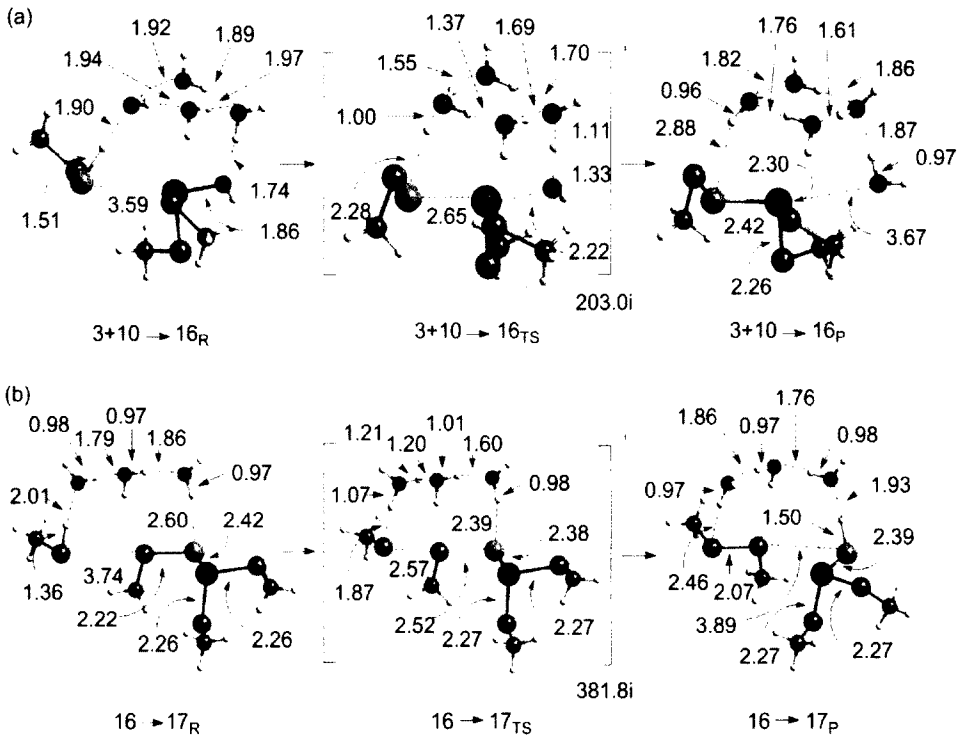

Figure 6. Selected bond distances (Å) for pathway B ((a) **3+10→16** and (b) **16→17**). Imaginary vibrational modes are listed for each transition state structure.

In pathway C, the steps leading to the As-Se species (**1+11→12→13→17)** are modeled as a sequence of nucleophilic attacks to form final product **17** (Figure 7) using SAPE network 1 (Scheme 1). In the first step of pathway C, **11** attacks **1** and forms intermediate **12**, while in subsequent steps, RSH acts as the nucleophile to form **17.** The activation energy barrier in **12→13** is significantly higher (+19.4 kcal/mol) than both the previous (+13.6 kcal/mol) and proceeding (+10.4 kcal/mol) step, making this the rate-determining step in the reaction and unlikely to occur.

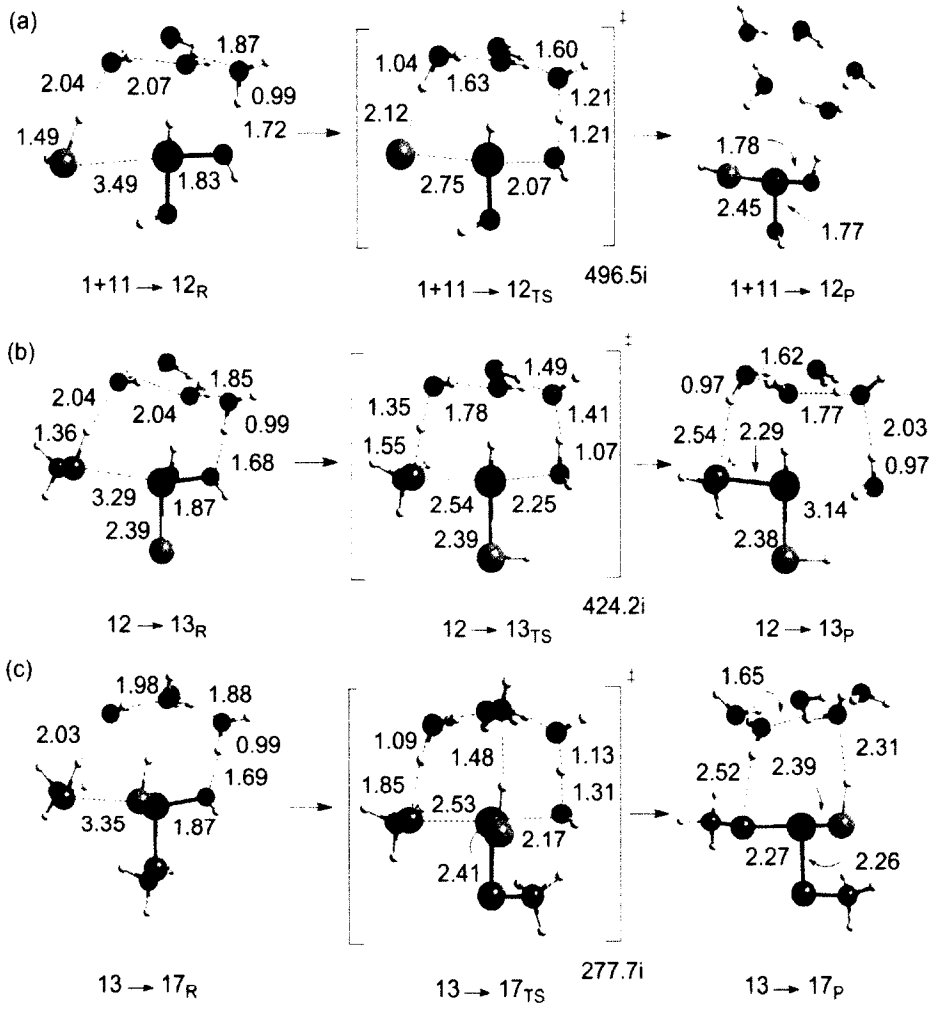

Figure 7. Selected bond distances (Å) for pathway C ((a) 1+11→12, (b) 12→13, and (c) 13→15). Imaginary vibrational modes are listed for each transition state structure.

Pathways D, E, and F are initial steps in the formation of the As-Se bond: (D) the reduction of **1** by **10** to form **14**, methylthioseleno-bis(hydroxyl)arsenite (**1+10→14**, Figure 8), (E) attack of **2** on **10**, yielding intermediate **15**, methylthioseleno-(hydroxomethylthionyl) arsenite (**2+10→15**, Figure 9), and (F) the formation of **13** through the attack of **2** on **11** (**2+11→13**, Figure 10). SAPE network 1 (Scheme 1) was

utilized to aid proton transfer for each mechanism. Exergonic steps **1+10→14** (-8.4 kcal/mol), **2+10→14** (-12.7 kcal/mol), and **2+11→13** (-24.6 kcal/mol) have similar barrier heights (+15.0 kcal/mol, +13.3 kcal/mol, and 14.3 kcal/mol, respectively) to **1+11→12**. It is unlikely pathway D will take place due to the harder As center in **1** and weaker nucleophilic strength of **10**. Pathways E (**2+10→15**) and F (**2+11→13**) and step **2→3** are competing pathways involving electrophiles with harder arsenic centers than intermediate **3**. Step **2→3** has an activation barrier ≈6 kcal/mol higher than **2+10→15** and **2+11→13**, allowing **2** to be available for reaction. Activation heights of **2** with **10** and **11** are relatively similar (+13.3 and +14.3 kcal/mol, respectively), but higher than reactions of **3** and **10** and **11**, due to the greater hardness of the As center in **2**. All steps require significantly more energy than reaction **3+11→17**, therefore these reactions are unlikely to take place.

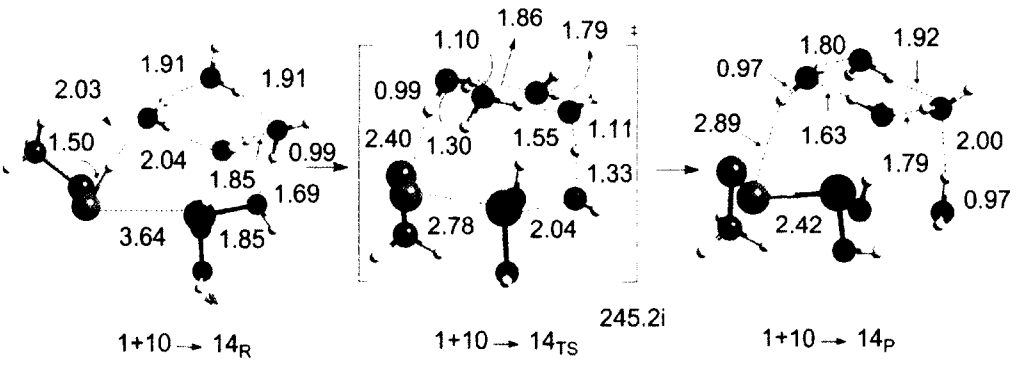

Figure 8. Selected bond distances (Å) for pathway D (1+10→14). The imaginary vibrational modes is listed for the transition state structure.

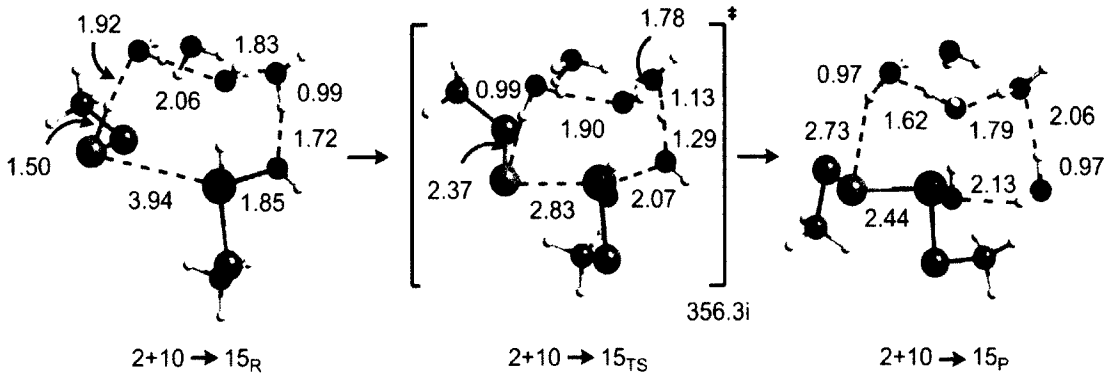

Figure 9. Selected bond distances (Å) for pathway E (2+10→15). The imaginary vibrational mode is listed for the transition state structure.

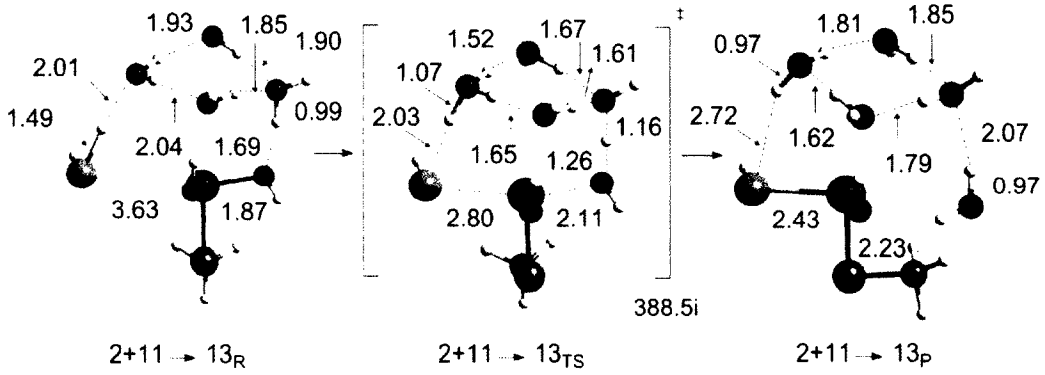

Figure 10. Selected bond distances (Å) for pathway F (2+11→13). The imaginary vibrational mode is listed for the transition state structure.

Table 3. Relative DFT(mPW1PW91) energies and activation barrier for the complexation of $(GS)_2AsSeH$ (**3+11→17**, **3+10→16**, **16→17**, **1+11→12**, **12→13**, **13→17**).

Reaction		TS	Product
Pathway A			
3+11→17	ΔH	1.2	-19.8
	ΔG	6.9	-19.9
	$\Delta G + \Delta G_{solv}$	8.6	-21.5
Pathway B			
3+10→16	ΔH	0.3	-21.0
	ΔG	6.9	-20.7
	$\Delta G + \Delta G_{solv}$	10.8	-15.9
16→17	ΔH	15.3	2.4
	ΔG	23.3	5.7
	$\Delta G + \Delta G_{solv}$	21.9	8.4
Pathway C			
1+11→12	ΔH	8.1	-16.7
	ΔG	14.7	-17.3
	$\Delta G + \Delta G_{solv}$	13.6	-18.6
12→13	ΔH	9.6	-10.3
	ΔG	15.5	-9.7
	$\Delta G + \Delta G_{solv}$	19.4	-8.9
13→17	ΔH	8.5	-18.4
	ΔG	16.3	-17.8
	$\Delta G + \Delta G_{solv}$	10.4	-17.2
Pathway D			
1+10→14	ΔH	5.4	-12.6
	ΔG	14.0	-10.4
	$\Delta G + \Delta G_{solv}$	15.0	-8.4
Pathway E			
2+10→15	ΔH	7.3	-21.1
	ΔG	13.9	-25.4
	$\Delta G + \Delta G_{solv}$	13.3	-12.7
Pathway F			
2+11→13	ΔH	7.6	-21.1
	ΔG	14.7	-25.4
	$\Delta G + \Delta G_{solv}$	14.3	-24.6

Based on our DFT-SAPE results, the reaction of selenide **11** with **3** (pathway A) should be the most favorable mechanism in the formation of the As-Se bond. Reaction **3+11→17** has a low activation barrier due a stronger interaction between the soft nucleophile **11** and the soft electrophile **3**. Concurrent with selenite reduction, arsenite will be converted to **3** by excess thiols, making **3** available for reaction. The first two steps of selenite reduction, **5→6** ($\Delta G^{\ddagger}$=+6.2 kcal/mol) and **6→7** ($\Delta G^{\ddagger}$=+6.6 kcal/mol), will yield no observable intermediates. Step **7→8** will take place slowly based on the higher barrier (+19.2 kcal/mol), creating a bottleneck at **7**. Intermediate **8** is rapidly reduced to **9** (+7.8 kcal/mol) and further reduction of **9** to **10** and **11** have high barriers (+19.0 and +19.9 kcal/mol) comparable to steps **1→2** and **2→3** of arsenite reduction ($\Delta G^{\ddagger}$=+20.0, +21.7 kcal/mol). Therefore, it is expected that formation of **3** would occur parallel to **10** and **11** and that it is unlikely that **1** would be available for reaction through pathway C. This conclusion is consistent with experimental results by Hsieh and Ganther who determined that **1** completely inhibits the formation of **11** and will react with selenite reduction by-products before selenide is formed.[81]

Conclusion

The thiol reduction of arsenite and selenite, as well as the formation of an arsenic-selenium complex were modeled using DFT-SAPE methods. In the three-step reduction of arsenous acid by thiol, the first two steps were determined to take place slowly such that the intermediates may be long-lived enough to interact with other species, such as intermediates in the reduction of selenite. The DFT-SAPE models in this

study may be used as a basis for examining the reactions of arsenite with other thiol-containing proteins. The formation of an arsenic-selenium product is predicted to proceed through the attack of selenide on arsenic-reduction intermediate **3** to form **17**. Alternate pathways to As-Se bond formation were less favorable due to large barrier heights and the lower likelihood that required intermediates would be bioavailable. However, experimental evidence is lacking and the isolation and characterization of reaction intermediates, as well as kinetic studies, could provide information on the possibility and stability of intermediates.

CHAPTER 3

THE DETOXIFICATION OF LEWISITE WITH BRITISH ANTI-LEWISITE USING DFT-SAPE MODELING.

Introduction

Lewisite (**1**, *trans*-2-chlorovinyldichloroarsine), developed at the end of World War I, is an arsenical vesicant chemical warfare agent coined as the 'Dew of Death' that causes severe blistering of the skin, eyes, and lungs.[10] **1** can be rapidly absorbed through the skin and is more lethal (LD_{50} = 0.5-50 mg/kg in rabbits and rats)[12] than mustard gas (LD_{50} = 100 mg/kg)[104], another blistering agent. The liquid agent can be dispersed by spray or through bombs or artillery shells.[11, 105] The United States was first to produce lewisite in bulk at the end of World War I, followed by Great Britain, France, Italy, the Soviet Union, Germany, and Japan. Although **1** has never officially been used militarily, Iraqi forces were speculated to have used it in combination with mustard gas in the Persian Gulf War (1991) and by the Soviets during the invasion of Afghanistan in 1982, allegedly killing about 3,000 people.[16] **1** remains a potential threat, because terrorists could steal it from the 35-40 countries estimated to still have it stockpiled.[16] Since 2002, safety drills across the United States have been conducted based on the potential use of **1** in a terrorist attacks, suggesting that the threat of use of **1** still remains.[16] Disposal of **1** began after World War II, when stockpiles were dumped into large bodies of water such as the Atlantic, Arctic and Indian oceans.[16, 106] Leaching from these discarded munitions, as well as the remaining buried stockpiles, potentially threatens ecosystems, commercial fishing and water supplies.[16, 107] Therefore, detoxification of **1** is important

for treatment of human exposure and for the decontamination of storage site and water supplies.

Toxicity of **1** is due to the affinity of its soft trivalent arsenic (As(III)) for sulfhydryl-containing biomolecules such as glutathione (GSH), cysteine (Cys), and other thiols.[108] Of particular importance is the inhibition of pyruvate dehydrogenase through binding to the dithiol of the lipoic acid substrate by low concentrations of arsenic.[7, 8] This inhibition hinders acetyl coenzyme formation, oxidation of fatty acids[109] and production of adenosine triphosphate by blocking the citric acid cycle.[110] Even low concentrations of **1** (1.5×10^{-6} M) can inhibit the enzyme activity by 50%.[18]

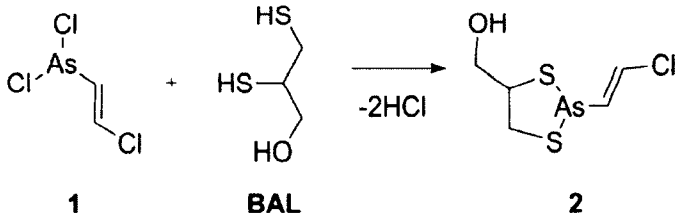

1 **BAL** **2** (13)

At the beginning of World War II, the British sought out an antidote for **1** due to the fear of its use by the Nazis.[16, 17, 30] In 1940, British anti-lewisite (BAL, 2,3-dimercaptopropanol) was shown to chelate As(III) to form a stable, nontoxic product (2-methyl-1,3,2-dithiarsolan-4-yl)methanol, **2**) (eq 13).[18] Monothiols were less effective in the prevention of pyruvate dehydrogenase inhibition and other effects of **1** due to the inability to chelate.[19] BAL exists as either a D or L enantiomer and is able to pass readily through the skin to neutralize **1** by the formation of **2**, which is excreted in urine. Peters

et al. showed that timely administration of to human subjects exposed to **1**, not only completely protected against inhibition of pyruvate dehydrogenase, but reversed toxic effects.[18]

The detoxification mechanism is expected to proceed through the sequential S_N2-type attack of the BAL thiolates on the As-Cl bonds of **1**. Computational studies have investigated this mechanism using explicit water and ammonia molecules in the model of the reaction pathway.[111] However, the chloride leaving group was positioned adjacent to the nucleophile ($\angle$S···As–Cl= 90°), inconsistent with bond overlap between the lone pair on the incoming sulfur nucleophile and As-Cl σ* antibonding orbital opposite. Although the model was claimed to be water-catalyzed, water does not actively participate in the reaction (i.e., the added water remains unchanged throughout the mechanism) and acts only to solvate the transition state to lower the calculated barrier.[111] Even if the water molecule truly acted as a catalyst, the incorrect positioning of the nucleophile with respect to the leaving group is not a realistic representation of an S_N2-type process, resulting in strained transition states with higher than expected activation barriers.

Our group has used solvent-assisted proton exchange in conjunction with density functional theory (DFT-SAPE) to provide realistic gas-phase models of aqueous reactions.[82, 83, 112, 113] SAPE uses a network of water molecules to connect the protonation sites in the nucleophile and leaving group to facilitate proton transfer in order to mimic the role of the protic solvent.[82, 114-116] Networks of water molecules are added to a complex of the reacting molecules in the correct orientation for the reaction.

The combination of explicit waters and the proper orientation of the reactants provides a more realistic transition and lower barrier heights than other gas-phase models. DFT-SAPE studies have previously been successful in modeling the reduction of arsenite by thiol and the formation of an As-Se adduct resulting from the antagonistic relationship between As and Se.[102] In this study, we use DFT-SAPE modeling of the molecular mechanism of detoxification of **1** by BAL as a step toward understanding the inhibition of biochemical processes by chemical warfare agents and the development of more effective antidotes for these deadly compounds.

Computational Methods

Geometry optimizations of the detoxification of lewisite by BAL were performed in Gaussian03[86] using the mPW1PW91[88] functional. Arsenic, chlorine, oxygen, carbon and all hydrogens connected to non-carbon heavy atoms or involved in the SAPE network were represented by Ahlrich and coworkers' split-valence triple-ζ basis set with polarization functions (TZVP).[50] These basis sets were augmented with diffuse *s*-, *p*-, (As, Cl, S and O) and d-type (As only) functions (TZVP+). A double-ζ basis set with polarization functions on carbon has used for hydrocarbon fragments.[117] A SAPE network where three water molecules connect the incoming thiol proton and the leaving –Cl group in the model systems to provide a pathway for proton transfer (Scheme 5) while accommodating the proper orientation of the attacking sulfur and the chloride leaving group for an S_N2-type process ($\angle S\cdots As–Cl \approx 180°$). The hydroxyl group of BAL was positioned to prevent hydrogen bonding with the water network to reduce strain in the

models. Transition states were found by a manual scan of the selected reaction coordinate followed by a full optimization. Each transition state was found to have one imaginary frequency along the appropriate reaction coordinate. Reported energies include zero-point energy (ZPE), thermal, and entropic corrections. Polarizable continuum models (PCM)[95] using Bondi atomic radii[96] were employed for bulk solvation corrections for water.

Scheme 5. Three-water SAPE model used in DFT calculations.

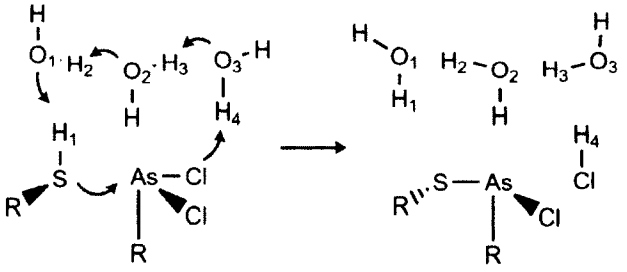

Results and Discussion

The reaction of **1** with BAL was modeled as two S_N2-type steps: (1) initial attack of a BAL thiol on **1** to intermediate followed by (2) an attack of the other thiol to close the ring (Scheme 6). In pathway I, the primary thiol (S_A) reacts with As(III) first and in pathway II, the secondary thiol (S_B) reacts first. Pathways are further distinguished by the chirality of the secondary carbon of BAL (D and L). The stationary points (reactant (R), transition state (TS), or product complex (P)) for each pathway are labeled by their attacking sulfur and BAL enantiomer (for example, **1**→**IA**$_{TSL}$ is the transition state for

step 1 with S_A of L-BAL). Activation barriers and reaction energies are reported as the solvation-corrected Gibbs free energy ($\Delta G+\Delta G_{sol}$, Table 4).

Scheme 6. Detoxification of **1** with BAL (a) initial reaction with the primary thiol (S_A) and (b) initial reaction with the secondary thiol (S_B). The chiral carbon is indicated by *.

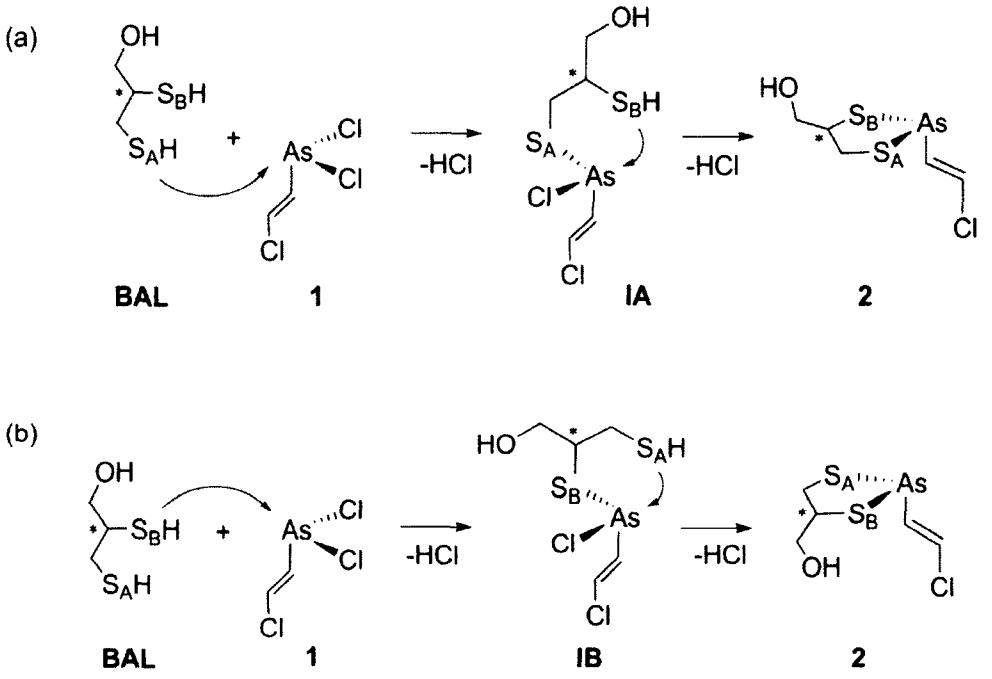

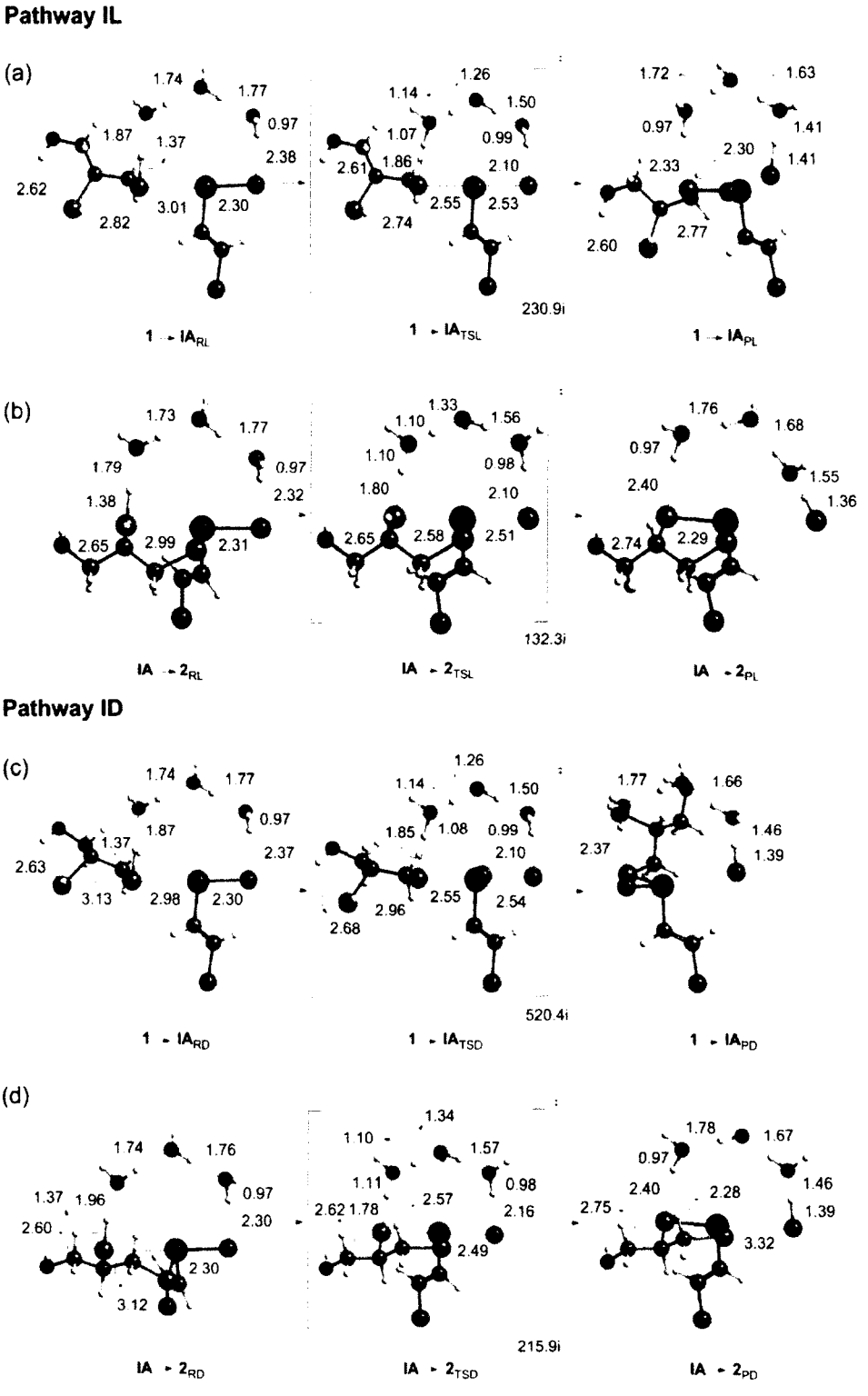

Figure 11. Selected bond distances (Å) for pathway IL ((a) **1**→**IA**$_L$ and (b) **IA**→**2**$_L$) and pathway ID ((c) **1**→**IA**$_D$ and (d) **IA**→**2**$_D$). The imaginary vibrational modes are listed for each transition state structure.

In pathway IL (Figure 11a-b, **1**→**IA**$_L$→**2**$_L$) and ID (Figure 11c-d, **1**→**IA**$_D$→**2**$_D$), the formation of **2** through the attack of BAL (S_A) on **1** and the subsequent attack of the second thiol (S_B) eliminates HCl at each step (Scheme 6a). In the reactant complex **1**→**IA**$_{RL}$, the incoming thiol, S_A, in L-BAL is well positioned by the SAPE network for backside attack upon the arsenic center of **1** (∠S···As–Cl = 177°). Similarly in the second step, S_B was arranged to approach **IA** from the backside of the second chloride leaving group to form **2**. The reactant complexes **1**→**IA**$_{RL}$ and **IA**→**2**$_{RL}$ have the incoming thiol positioned ~3 Å away from As, where the As-S bond distances decreases to ~2.6 Å in **1**→IA$_{TSL}$ and **IA**→**2**$_{TSL}$ with a see-saw type TS structure (Figures 11a-b). Proton transfer within the SAPE network can be seen in the decreases in distance in the hydrogen bonding interactions (i.e. in **1**→**IA**$_{RL}$ to **1**→**IA**$_{TSL}$, H_2-O_2 bond distance decreases from 1.74 to 1.26 Å as the H_3-O_3 bond length decreases from 1.77 to 1.50 Å). The activation barriers for these pathways with each stereoisomer are very low (+0.7 – +4.9 kcal/mol, Table 4) with the ring formation in L-BAL predicted to be nearly instantaneous (+0.7 kcal/mol). These results are consistent with rapid formation of **2** due to the chelate effect as found in experimental studies.[18] In contrast, D-BAL requires a higher activation energy ($\Delta G^{\ddagger}$=+4.9 kcal/mol) for the second step, possibly due to ring strain in the As···S_B interaction of **IA**→**2**$_{RD}$ introduced by the constraints of the chirality of the molecule. The similarities in the activation barriers for D-BAL and L-BAL suggest that neither stereoisomer is significantly more reactive and separation of the racemic mixture would not enhance the effectiveness against **1**. In comparison, models without explicit water molecules or those that only solvate the transition state lead to significantly higher

barriers (for comparison to **1**→**IA**$_L$, $\Delta G^{\ddagger}$=+24.2 (no water), +16.1 (one solvent water), +9.7 (two solvent waters) kcal), due to the incorrect orientation of the nucleophile and leaving group in the transition state ($\angle$S···As–Cl = 98°).

Pathway II (Scheme 6b, **1**→**IB**→**2**) reverses the order of attacking sulfur, where S_B is the nucleophile in the first step, and S_A attacks to close the ring to form **2** (Figure 12). The initial step in both pathways are predicted by DFT to take place rapidly ($\Delta G^{\ddagger}$=+3.8 kcal/mol for **1**→**IB**$_L$; $\Delta G^{\ddagger}$=+5.3 kcal/mol for **1**→**IB**$_D$; Table 4). The barrier heights for the formation of **2** in **IA**→**2**$_L$ and **IA**→**2**$_D$ are low (+1.3 and +1.5 kcal/mol, respectively), meaning ring formation will take place quickly as for pathway I. The activation barrier in the first step of mechanism IIL (Figure 12a, **1**→**IB**$_L$) is only slightly higher (~+0.7 kcal/mol) than that calculated for **1**→**IA**$_L$, suggesting that there is no preference for the initial attack of either S_A or S_B. As in pathway I, the barrier height for step **1**→**IB**$_D$ (Figure 12c) is 1.5 kcal/mol higher than **1**→**IB**$_L$, suggesting a slight preference for L-BAL in the attack of S_B, but unlikely to be observable due to the low activation barriers. This result is in agreement with experimental studies of 2,3-dimercapto-1-propane-sulfonic acid (DMPS) and *meso*-2,3-dimercaptosuccinic acid (DMSA), where there is no preference for the D- or L- isomer in the prevention of the toxicity of sodium arsenite.[118]

The activation barriers for **1** with BAL are significantly lower than those calculated for the reduction of arsenite with methyl thiol, (e.g., $As(OH)_3$ + MeSH → $(MeS)As(OH)_2$, $\Delta G^{\ddagger}$=+20.0 kcal/mol)[102] due to the greater stability of the chloride leaving group. The reaction of arsenite with GSH is slow, where a window of 9 hours under

biological conditions is used to ensure $As(SG)_3$ formation, consistent with high barriers found in the reduction of arsenite with thiol.[97] However, the formation of nontoxic ring product **2** is rapid based on the fast disappearance of **1**'s toxic effects and increased As urinary excretion.[119] In the DFT-SAPE models, an HCl molecule is the leaving group for each step because the three-water network is insufficient to fully solvate a chloride ion. In previous SAPE-type modeling of the water-catalyzed decomposition of chloromethanol, 4 or more waters are needed for HCl to be deprotonated in the product.[114] As a result, the overall reaction energies for the two pathways are smaller than expected and the activation barriers may be overestimated in the present study.

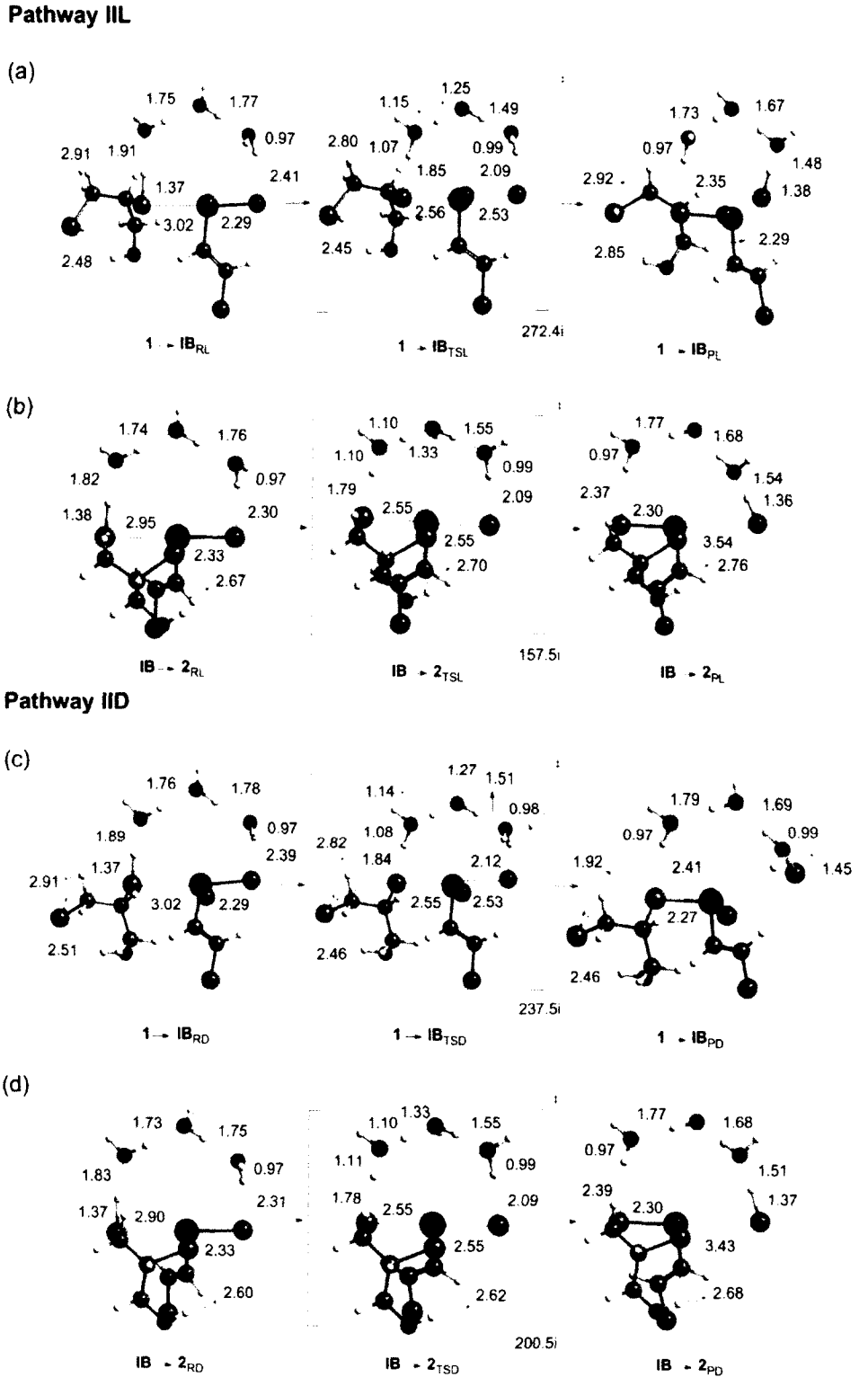

Figure 12. Selected bond distances (Å) for pathway IIL ((a) **1**→**IB**$_L$ and (b) **IB**→**2**$_L$) and pathway IID ((c) **1**→**IB**$_D$ and (d) **IB**→**2**$_D$). The imaginary vibrational modes are listed for each transition state structure.

In addition to inhibiting pyruvate dehydrogenase through the reaction with lipoic acid, arsenite and **1** can react with proteins that contain as least two Cys at the active site (e.g., alcohol dehydrogenase,[120] hexokinase,[108] and succinic oxidase[108]). Experimentally, As(III) has a greater affinity for dithiols versus monothiols as observed in the displacement by dithiols of GSH from $As(SG)_3$ and Cys residues from arsenated proteins (i.e. metallothionein, dihydrolipoamide dehydrogenase, etc...).[121] DFT calculations show that ring formation is favored when dithiol reacts with a monothiol-As complex to produce two molar equivalents of monothiol and a dithiol-As complex ($SHCH_2CH_2SH + (CH_3S)_2As(CHCHCl) \rightarrow 2CH_3SH + (SCH_2CH_2S)As(CHCHCl)$, ΔG=-8.07 kcal/mol). In an near-UV absorption spectroscopy study, stability constants calculated for the formation of $As(SG)_3$ ($1.0\ (\pm 2) \times 10^7$) versus *bis*-(DMSA)As-OH ($5(\pm 2) \times 10^9$) show that As has a greater affinity for the dithiol and will displace GSH from the complex.[97] The inhibition of these proteins can be reversed through the addition of BAL, because the 5-membered ring of **2** is more stable than the larger (>6-membered) rings in the arsenated protein.[122] The same can be said for **1** in the presence of dithiols where reaction is rapid,[18] presumably less than 10 minutes under ambient conditions based on the reaction rate of an aqueous solution of lewisite and 1-butanethiol.[123]

Table 4. Relative DFT(mPW1PW91) energies for the formation of 2-methyl-1,3,2-dithiarsolan-4-yl)methanol (**1**→**IA**$_L$, **IA**→**2**$_L$, **1**→**IA**$_D$, **IA**→**2**$_D$, **1**→**IB**$_L$, **IB**→**2**$_L$, **IB**→**2**$_L$, **IB**→**2**$_D$).

Reaction		TS	Product
Mechanism IL			
1→**IA**$_L$	ΔH	6.9	-2.6
	ΔG	12.1	-3.5
	ΔG + ΔG$_{solv}$	3.1	-4.9
IA→**2**$_L$	ΔH	4.5	-2.2
	ΔG	8.7	-2.5
	ΔG + ΔG$_{solv}$	0.7	-3.1
Mechanism ID			
1→**IA**$_D$	ΔH	7.2	-3.3
	ΔG	12.6	-0.8
	ΔG + ΔG$_{solv}$	2.9	2.0
IA→**2**$_D$	ΔH	7.8	1.7
	ΔG	13.1	2.4
	ΔG + ΔG$_{solv}$	4.9	-1.2
Mechanism IIL			
1→**IB**$_L$	ΔH	8.8	-0.3
	ΔG	14.4	-1.3
	ΔG + ΔG$_{solv}$	3.8	-3.6
IB→**2**$_L$	ΔH	4.7	-2.5
	ΔG	9.6	-3.0
	ΔG + ΔG$_{solv}$	1.3	-4.0
Mechanism IID			
1→**IB**$_D$	ΔH	7.4	0.7
	ΔG	13.5	2.2
	ΔG + ΔG$_{solv}$	5.3	-1.5
IB→**2**$_D$	ΔH	4.8	-2.1
	ΔG	10.7	-1.4
	ΔG + ΔG$_{solv}$	1.5	-3.4

Conclusions

Computational modeling of the interaction of As(III)-containing chemical warfare agents with biological systems is important for understanding toxicity at a molecular level. British anti-lewisite, the antidote to **1**, contains two thiol substituents that are available for attack on the arsenic center of lewisite and possesses a chiral carbon center. DFT-SAPE modeling suggests minute differences in attack between sulfurs as well as chirality with very low activation barriers consistent with rapid inhibition of the toxic effects of **1**. In comparison to our previous study on the reduction of arsenite by thiol using DFT-SAPE, lower activation barriers for the reaction of **1** relative to arsenite with thiol is in agreement with the weaker basicity of the –Cl leaving group (compared to –OH leaving group). In contrast to previous explicit solvation modeling, DFT-SAPE models preserve the nature of the attack (presumed S_N2) and utilize water as a true catalyst. Alternate antidotes for **1** poisoning are of interest due to painful intramuscular administration[119, 124] and side effects such as nausea, vomiting, and headaches[125] as well as the increase in As concentration in rabbit brain after treatment with toxic BAL.[118, 126] Two BAL-analogues, DMPS and DMSA, have been determined to be as effective as BAL and easier to administer; however, BAL still remains the preferred antidote in the United States.[118, 126, 127] Further DFT-SAPE studies could be used to describe reactions of **1** and other chemical agents to understand the mechanisms of both the attack on the protein and the action of the dithiol to aid in the development of new antidotes of potentially harmful arsenicals.

CHAPTER 4

WIBERG INDICES TO DISCOVER POTENTIAL PATHWAYS IN THE COMPOSITION OF HIGH ENERGY DENSITY MATERIALS

Introduction

The development of stable and efficient high energy density materials (HEDMs) for military, aeronautical, and engineering applications has been a focal point of many research groups. The development of more effective and environmentally safer explosives is an important goal of this research.[3] However, the decomposition mechanisms of these compounds, in particular, the initialization step of these reactions, are not well understood. Experimental analysis is limited due to the rapid rate at which these reactions take place, so computational tools such as molecular dynamics (MD) and density functional theory (DFT) have been used in order to determine the dominant initial reaction.[9] Decomposition mechanisms have been proposed based on weak bonds in explosive materials. The bond strength is a good indicator of potential pathways for bond cleavage leading to detonation and several methods have been used to identify weak bonds (i.e. bond dissociation energies (BDE), natural bond order analysis (NBO), and electron densities) within explosive materials. Characterization of weak bonds through computational methods is important for determining initiation mechanisms in known HEDMs and can be used to establish possible bond breaking mechanisms in novel HEDMs.

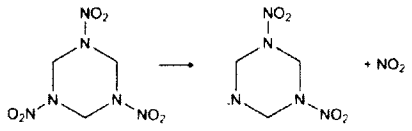

(14a)

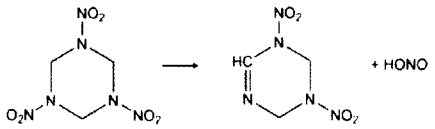

(14b)

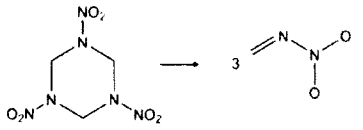

(14c)

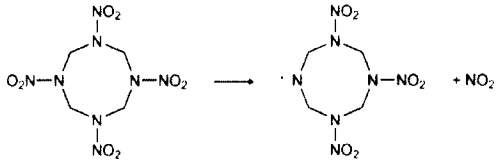

(15a)

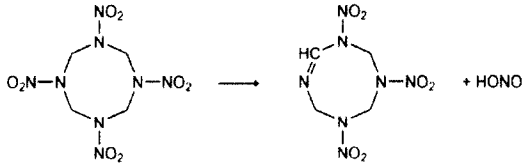

(15b)

The mechanisms of common secondary explosives, 1,3,5-trinitro-1,3,5-triazacyclohexane (RDX), 1,3,5,7-tetranitro-1,3,5,7-tetrazacyclooctane (HMX), 2,4,6-trinitrotoluene (TNT), and pentaerythritol tetranitrate (PETN) have been studied experimentally through decomposition product analysis with mass spectrometry from laser- and pyrolysis-induced decomposition[128-131] and theoretically using density functional theory.[35, 132, 133] Several decomposition pathways (eqs 14-15) have been proposed to include (a) homolytic cleavage, (b) molecular eliminations/rearrangements, and (c) ring opening. Zhao et al.[134] suggested that concerted ring fission (eq 14c) is the initialization step in the unimolecular thermal decomposition of RDX based upon infrared multiphoton dissociation. However, other photochemical decomposition studies argue N-N homolysis is dominant in the condensed phase.[135] Gas-phase DFT calculations found that N-N homolytic cleavage and HONO elimination for RDX (eqs 14a-

b) have similar barriers (~40 kcal/mol), while concerted ring fission (eq 14c) is 20 kcal/mol higher.[132] The conclusion that the gas-phase decomposition of RDX is predominantly the breaking of N-NO_2 is supported by several theoretical studies.[136, 137]. Similarly, an N-N homolytic cleavage (eq 15a) and HONO elimination (eq 15b) have been proposed as the initial pathway in the gas-phase decomposition of HMX. Theoretical calculations predict N-N homolytic bond breaking in HMX is more favorable (~6 kcal/mol) than concerted HONO elimination (eq 15b) but subsequent steps in the degradation of their products are less exothermic.[35] Product distributions from mass spectrometry (CH_2O, N_2O, HONO, and HCN) have been used to propose oxygen transfer from the nitro group to the adjacent carbon for HMX[129, 131] as well as a concerted ring fission to form four methylenenitramine molecules.[138]

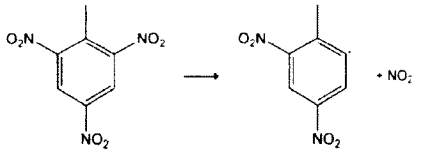

(16a)

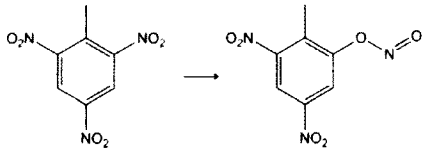

(16b)

Homolytic cleavage[139-141] (eq 16a) and a –ONO rearrangement[142] (eq 16b) have been suggested as the initial step using several experimental studies with varying experimental conditions for TNT. Based on similarity in structure, the most dominant pathway for initiation at high temperatures is a C-NO_2 break evidenced by laser pyrolysis of nitroaromatic compounds like 2,4-dinitrotoluene.[141] A –ONO rearrangement was suggested as an initial step based on the gaseous product NO formation through a

phenoxy radical[142]. Cohen et al.[143] used DFT studies to conclude that the the initialization step for unimolecular thermal decomposition of TNT is C-NO_2 cleavage on experimental time scales.

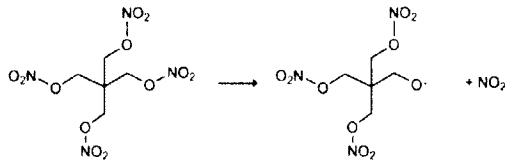

(17a)

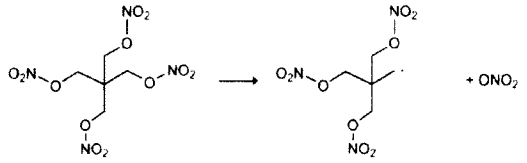

(17b)

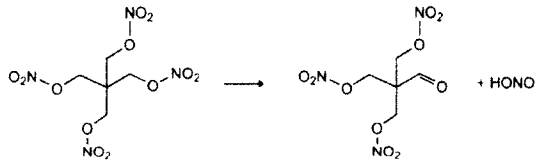

(17c)

Proposed decomposition mechanisms for PETN are similar to other HEDMs: 1) homolytic O-NO_2 and 2) C-ONO_2 cleavage, and a 3) HONO elimination (eqs 17a-c). Ng et al.[144, 145] determined that the primary thermal decomposition mechanism is the O-NO_2 bond cleavage based on similar activation barriers found in mononitrate and nitrite esters. Liu et al.[146] performed DFT calculations and found that an O-N bond break has a bond dissociation energy of 39.0 kcal/mol compared to energies of 82.2 and 39.2 kcal/mol for C-O and HONO elimination, respectively. Therefore, it is concluded that the O-NO_2 homolytic cleavage is the primary pathway in the decomposition of PETN.

In 1979, Kamlet[33] introduced the term 'trigger linkage' as the bond that initiates explosive decomposition and may be an important identifier when proposing compounds with explosive properties. Due to the weak nature of C-N and N-N bonds in

nitramines, it is likely that the X-NO_2 (X = C, N, O) bond is the first to rupture, evidenced by the gaseous products (i.e. N_2O, H_2O, NO_2, NO, CO_2, and CO) determined by mass spectrometry.[34] Theoretical calculations to determine bond strength have been used to identify weak bonds in explosive molecules. These methods include the determination of the electron density (ρ) between atoms using the Atoms-In-Molecules (AIM) method,[36, 37] unimolecular decomposition activation barriers,[35, 132] calculated bond dissociation energies (BDE),[147], and molecular dynamics simulations of shock-initiated decomposition[38]. Trigger bonds are expected to have longer bond lengths and lower electron density relative to those found in chemically similar, yet unconstrained, reference compounds. Wiberg Bond Indices (WBIs), a measurement of electron density between two atoms in a compound (eq 18), have been used to determine trigger bonds in dinitroamino-substituted benzene derivatives[148]. However, they did not compare to a reference to determine an absolute scale for the weakening of the bond.

$$B_{AB}^{Wiberg} = \sum_{\lambda \epsilon A} \sum_{\omega \epsilon B} P_{\lambda\omega}^2 \quad (18)$$

The Wiberg bond order *B* represents the density between atoms A and B and is determined as the sum of the off-diagonal square of the density matrix, *P* (Wiberg).[149] WBIs values can be similar in magnitude to the bond order expected from valence bond theory. WBIs are a better measure of the bond strength relative to the overlap population, which is basis set dependent and often does not correlate well to bond strength. The possibility that bond orders for trigger linkages correlate well with experimental impact sensitivities across a set of analogous structures has been proposed by Xiao et al.[150, 151]

Nitrogen-rich novel energetic materials with nitro ($-NO_2$)[152], nitramine ($-NNO_2$)[153-155], and nitrate ester ($-ONO_2$)[156] functional groups with good stability and explosive properties comparable to RDX have recently been synthesized. In 2010, Fischer et al.[2] characterized a series of energetic materials (Figure 2) featuring tetrazoles and nitramines: 1-(2-nitro-2-azapropyl)-5-aminotetrazole (**1**), 1-(2-nitro-2-azapropyl)-5H-tetrazole (**2**), 1,5-bis(2-nitro-2-azapropyl)-5-nitraminotetrazole (**3**), 1-methyl-5-(2-nitro-2-azapropyl)-5-nitraminotetrazole (**4**), 1-methyl-4-(2-nitro-2-azapropyl)-5-nitraminotetrazole (**5**), 1-methyl-5-(2-nitro-2-azapropyl)-5-aminotetrazole (**6**), and 2-methyl-5-(2-nitro-2-azapropyl)-5-nitraminotetrazole (**7**). Many of these compounds have explosive properties (i.e., high detonation velocity and pressure, temperature, impact sensitivity, etc.) and structural aspects (cyclic compounds containing nitro groups) similar to common HEDMs and, like RDX, HMX, TNT, and PETN, decomposition mechanisms are not known.

The use of WBO values to determine bond strength could be applied to novel energetic materials in order to identify trigger bonds and their potential as an HEDM. Because decomposition mechanisms of RDX, HMX, TNT, and PETN have been thoroughly investigated, an analysis of the WBIs of these standard compounds can serve as a reference point for the application of WBIs to novel compounds. In this study, our goal is to (1) use WBI of RDX, HMX, TNT, and PETN to describe potential trigger bonds in their decomposition mechanisms, and (2) to apply WBIs to propose potential detonation pathways of novel HEDMs.

Computational Methods

Density functional theory geometry optimizations have been calculated for RDX, HMX, TNT, PETN, and compounds **1-7** using the Gaussian09 software package. Various functional/basis set combinations were used to determine the lowest unsigned errors in the potential trigger bonds (X-NO_2 and C-N backbone bonds, Table 1). The post Hartree-Fock (HF) method, MP2,[157] and B3LYP[44] functional were tested based on their common use in calculations of HEDMs. Hybrid functionals M06-2X[158], a method known to accurately describe dispersion forces for main group atoms, and mPW1PW91[88], were included based on their performance in predicting properties of a range of organic molecules.[159] A triple-zeta basis set (TZVP), with diffuse functions on all heavy atoms (TZVP+)[50] was paired with M06-2X, mPW1PW91, and MP2. The B3LYP functional was paired with both split-valence double- and triple-ζ Pople basis sets[46] with polarization functions on heavy atoms (6-31G*) and diffuse and polarization functions on all atoms (6-311++g**).[160] Calculations were also performed at the MP2/6-31G* level.

The commonly used B3LYP, MP2, and to a lesser extent, mPW1PW91 functional overestimate N-NO_2, C-NO_2, O-NO_2 bonds ranging from 1.4 $x10^{-2}$ (mPW1PW91) to $2.5x10^{-2}$ (B3LYP/6-311+G*) Å (Table 5). Similarly, C-N bonds are overestimated using B3LYP, MP2, and M06-2X ranging from $9.1x10^{-3}$ (B3LYP) to $5.6x10^{-3}$ (M06-2X) Å. The mPW1PW91 functional underestimates the C-N bond with a MUE of $1.7x10^{-3}$ Å. The M06-2X/TZVP+ functional/basis set combination yields, on average, small MUEs for X-NO_2 and C-N bonds, where calculated bond distances are slightly higher than those found in the crystal structure (i.e. the calculated O-NO_2 bond length in PETN-I is 0.003 Å

higher than the experimental value). Calculated C-N bond lengths found in the backbone of each HEDM yield comparable experimental distances, particularly for lengths found in AAE-RDX and each phase of PETN. In compounds **1-7**, principal bond lengths from DFT(M06-2X/TZVP+) calculations are in good agreement with experimental N-N (MUE: $9.2x10^{-3}$ Å) and C-N (MUE: $4.2x10^{-3}$ Å) distances in agreement with the low error when compared to other combinations of basis set and method. Therefore, geometry calculations performed on RDX, HMX, PETN, TNT, and **1-7** were executed using M06-2X/TZVP+. From the optimized structures of each compound, WBIs indices were calculated for each potential trigger bond using the NBO version 3.1.[161, 162]

Table 5. Mean unsigned errors for N-N, C-N, and N-O bonds for RDX, HMX, TNT, PETN, and **1-7** with the B3LYP, MP2, mPW1PW91, and M06-2X functionals and 6-31g*, 6-311+g**, and TZVP+ basis set.

Bond	Functional/Basis Set					
	*B3LYP/ 6-31G**	*B3LYP/ 6-311+G***	*MP2/ 6-31G**	*MP2/ TZVP+*	*mPW1PW91/ TZVP+*	*M06-2X/ TZVP+*
			RDX, HMX, TNT, PETN			
X-NO_2	$2.3x10^{-2}$	$2.5x10^{-2}$	$2.4x10^{-2}$	$1.7x10^{-2}$	$1.4x10^{-2}$	$1.4x10^{-2}$
C-N	$9.1x10^{-3}$	$8.4x10^{-3}$	$5.6x10^{-3}$	$7.0x10^{-3}$	$1.7x10^{-3}$	$1.2x10^{-3}$
N-O	$7.5x10^{-3}$	$9.6x10^{-4}$	$1.0x10^{-2}$	$1.5x10^{-2}$	$8.7x10^{-3}$	$1.2x10^{-3}$
			1-7			
N-NO_2	$7.2x10^{-3}$	$1.9x10^{-2}$	$2.7x10^{-2}$	$3.0x10^{-2}$	$7.4x10^{-3}$	$9.2x10^{-3}$
C-N	$4.8x10^{-4}$	$1.1x10^{-3}$	$1.0x10^{-4}$	$2.1x10^{-3}$	$3.0x10^{-2}$	$4.2x10^{-3}$
N-O	$2.0x10^{-1}$	$1.9x10^{-1}$	$2.1x10^{-1}$	$3.0x10^{-2}$	$1.8x10^{-1}$	$1.8x10^{-1}$

*WBI were calculated from optimized geometries using M06-2X/TZVP+

Results and Discussion

Solid-phase structures and DFT gas-phase conformations of RDX, HMX, TNT, and PETN are discussed along with their relative energies (Figure 13). WBI values (Tables 2 and 3) are compared to previous theoretical results and reference compounds (Figure 14, Table 4) in order to identify potential trigger bonds in the decomposition of these HEDMs. Reference compounds were chosen because they are simple, unconstrained molecules with the same bond type and hybridization as the HEDM compounds. WBI analysis (Table 5) is further used to identify trigger bonds in the optimized geometries of **1**-**7** (Figure 15) and compare the weakening of these bonds to explosive properties.

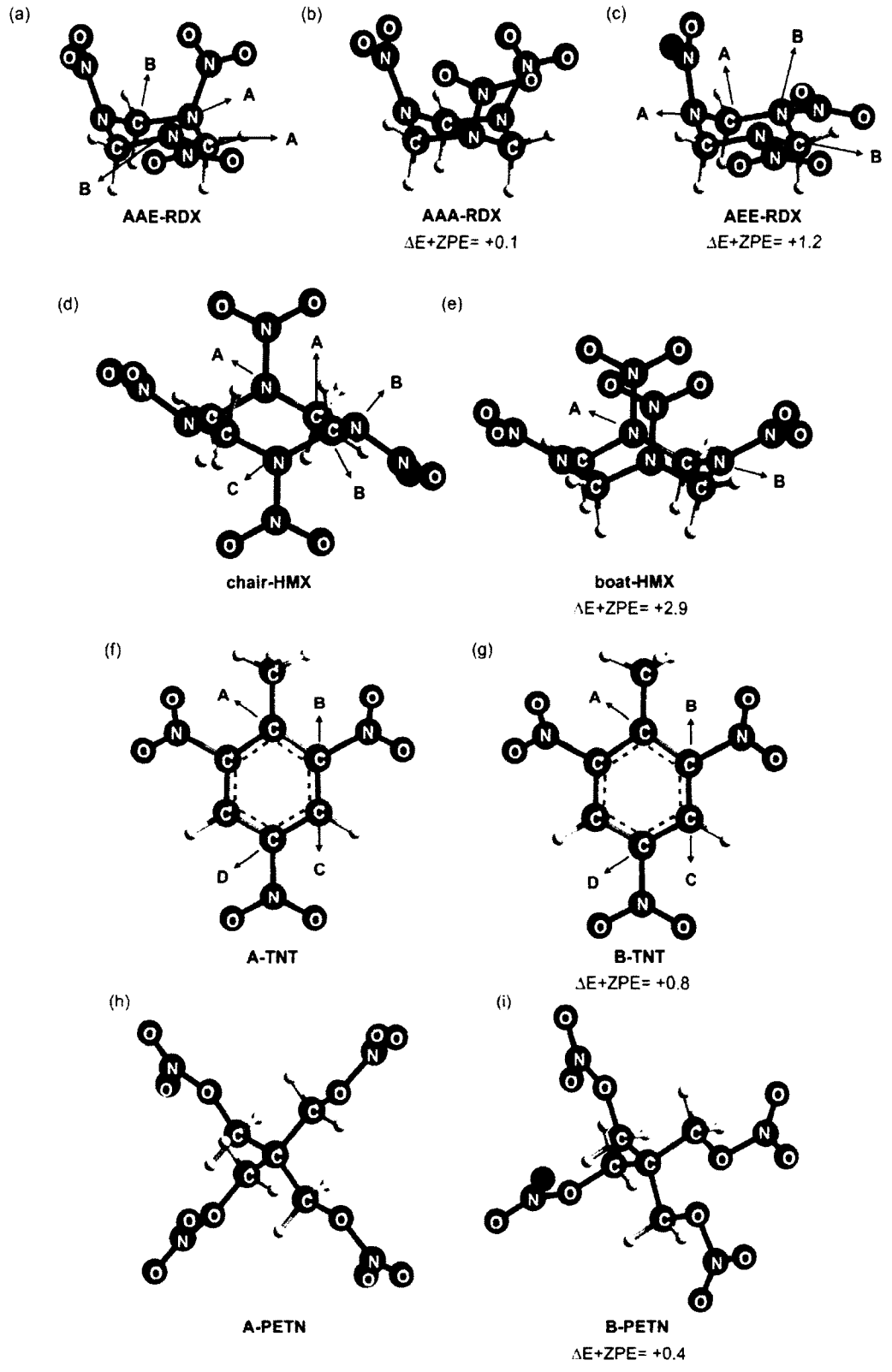

Figure 13. Optimized structures of the: (a) AAE, (b) AAA, and (c) AEE conformations of RDX; (d) chair and (e) boat conformations of HMX; (f) TNT-I and (g) TNT-II; and (h) PETN-I and (i) PETN-II with their relative DFT energies (M06-2X/TZVP+).

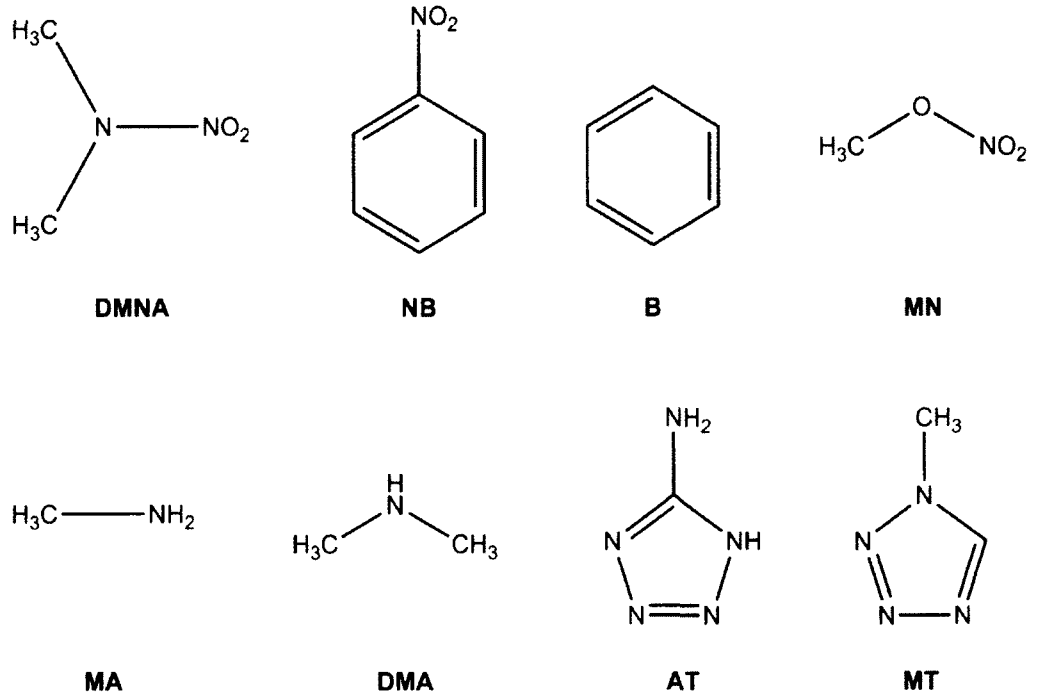

Figure 14. Reference compounds: dimethylnitramine (DMNA), nitrobenzene (NB), benzene (B), methyl nitrate (MN), methyl amine (MA), dimethylamine (DMA), 5-aminotetrazole (AT), and N-methyltetrazole (MT).

Optimized Structures of RDX, HMX, TNT, and PETN

DFT(M06-2X)/TZVP+ structures were optimized for various conformations of RDX, HMX, TNT, and PETN found in crystallographically distinct polymorphs. RDX exists in four phases: α, β, γ, and δ.[163, 164] Different phases of these structures possess conformations which are described by the position of the nitro- groups attached to the six-membered ring (Axial=A, equatorial=E). The α-phase, AAE (C_s), is present at ambient conditions up to ~4.0 GPa, where it converts to the pseudo-AAE orientation (γ-RDX).[163] The δ-phase (18-26.6 GPa) has contains the AAE structure with a slight change in the orientation of the E nitro group. The AAA (C_{3v}) conformation found in the β-phase

(prepared through recrystallization) converts back to α-phase (AAE) within seconds at room temperature.[163, 164] The AEE (C_{2v}) polymorph is not observed in crystalline forms, but is included for comparison of WBIs. The relative energy difference (DFT(M06-2X)/TZVP+) between AAE-RDX and AAA-RDX is small (+0.1 kcal/mol), suggesting that in gas-phase, the interconversion of the least stable β-RDX to stable α-RDX is rapid, whereas the AEE conformation is 1.2 kcal/mol higher in energy. The EEE polymorph is higher in energy (~5.0 kcal/mol relative to AAE).(Rice and Chabalowski) and not considered in this study.

HMX is known to exist in four different phases: α, β, γ, and δ.[165-169] The boat-like conformation of solid α-HMX (boat-HMX, C_{2V}) is orthorhombic with all nitro groups on the same side of the ring.[167] The unstable δ-HMX and γ-HMX polymorphs closely resemble boat-HMX.[170] Monoclinic β-HMX (chair-HMX, C_i) is the most dense, least impact-sensitive phase of HMX at room temperature[166] with two alternating axial nitro groups and the remaining alternating two in the pseudo-equatorial position. DFT(M06-2X)/TZVP+ gas phase calculations show that boat-HMX is 2.9 kcal/mol higher than the chair-like structure in agreement with theoretical observations.[35]

TNT and PETN are found in two crystalline phases.[171-175] TNT-I is stable at room temperature, whereas TNT-II is metastable. The $-NO_2$ groups in the crystal structures of TNT are non-planar due to crystal packing with different twist conformations in the two phases.[172, 176, 177] In TNT-I (A-TNT), both *ortho*-NO_2 groups extend forward (nonplanar) from the ring to maximize van der Waals interactions with $-CH_3$. In TNT-II (B-TNT), the planarity of *o*-NO_2 in position 2 is identical to the A conformation, but the 6-NO_2 group is

rotated to extend backward, reducing the number of intermolecular attractions by one. The *para* $-NO_2$ group is co-planar with the ring in both conformations to maximize conjugation of $-NO_2$ with the aromatic ring. The DFT bond distances of A- and B-TNT are comparable to experimental structures.[172, 176, 178] The conformations of PETN-I (A-PETN, D_{2d}) and the less stable PETN-II (B-PETN, S_4) differ in $-CH_2$-O-NO_2 dihedrals, where A has a four-fold symmetry and B has two $-CH_2$-O-NO_2 groups rotated about the C-C bond with respect to A. DFT(M06-2X/TZVP+) calculations show structure B of TNT is 0.4 kcal/mol less stable than A due to the lack of symmetry, and B-PETN is 0.8 kcal/mol less stable than A-PETN, which is in agreement with previous theoretical results.[178, 179]

Analysis of Wiberg Bond Indices of RDX, HMX, TNT, and PETN (Trigger Bonds)

WBIs were calculated from the DFT(M06-2X)/TZVP+ optimized geometries for potential trigger bonds, X-NO_2 (X=C/N/O) and C-N in the backbone of the ring structures, in RDX, HMX, TNT, and PETN as well as the reference compounds dimethylnitramine (DMNA), nitrobenzene (NB), benzene (B) and methyl nitrate (MN) (Figures 13 and 14). The comparison of these references to the HEDMs will determine if a weakening/strengthening of the bond in each bond type exists and to what degree. An index value is calculated as the difference between the HEDM WBI and the reference compound (ΔWBI) for a specific bond type. WBIs in HEDMs that are smaller than those in the reference compounds indicate a weaker bond that may be likely to initiate decomposition. Calculated WBI values will be compared with previous calculations of the bond strength using AIM, BDEs and other methods in order to determine if good

agreement exists between methods. Also, WBIs are compared to experimental impact sensitivities to determine if there is a correlation theoretical measures of the trigger bond and experimental properties.

The WBIs for proposed trigger N-NO_2 and backbone C-N bonds in RDX (AAE, AAA, and AEE conformations) and HMX (chair and boat) (listed in Tables 2 and 3) were compared to the N-NO_2 and C-N bonds in DMNA. Differences found in the axial and equatorial N-NO_2 bonds indicate that the bond strength is position dependent. In the AAE, AEE, and AAA conformations, axial bonds are longer (AAE: 1.422 Å, AEE: 1.430 Å, and AAA: 1.412 Å) than equatorial N-NO_2 bonds (AAE: 1.396 Å and AEE: 1.395 Å), and in comparison to DMNA reference (1.375 Å and WBI = 1.049), WBI values decreased more for bonds in the axial position (-9.34% for AAE, -10.58% for AEE, and -8.01% for AAA) versus the equatorial position (4.58% for AAE and 4.39% for AEE). Increases in N-NO_2 bond lengths in RDX could be attributed to destabilization by the ring structure and the greater weakening of the axial position could be attributed to the repulsion of the adjacent axial nitro group. It is notable that N-NO_2 bond lengths increase and strengths decrease with each additional equatorial –NO_2 group. This result is consistent with the observation by Moraes and Borges[36] that more E –NO_2 groups results in less electron density on the –NO_2 group and more delocalized to the C-N ring backbone, meaning the C-N are strengthened while N-N is weakened.[36] The C-N bonds in the ring structure of RDX range from 1.444-1.496 Å, values smaller and greater than the same bond in DMNA (1.455 Å). Shorter, stronger C-N bonds in RDX could be due to stabilizing interaction between the lone pair electrons on N in the ring and the antibonding orbital in C-N.

Concerted ring fission will not be as likely to happen based on a strengthening of the C-N (+1.76% relative to DMNA) in comparison to N-NO_2. Longer bond lengths and greater weakening of the axial N-N bonds in RDX when compared to reference compound DMNA suggests that an N-NO_2 bond break in the axial position is the most favorable pathway.

In HMX, longer and weaker bonds for the equatorial N-NO_2 bonds were found for both the chair ($d_{N\text{-}NO2}$ = 1.387 Å, WBI= 1.019) and boat ($d_{N\text{-}NO2}$ = 1.399 Å, WBI= 0.990) conformations in comparison to axial bonds (chair: $d_{N\text{-}NO2}$ = 1.376 Å, WBI= 1.025; boat: $d_{N\text{-}NO2}$- 1.386 Å, WBI= 1.005), similarly suggesting a positional preference in N-NO_2 cleavage. Our result is consistent with the barrier height difference calculated in chair-HMX between the axial and equatorial NO_2 groups in an N-NO_2 bond cleavage where the axial N-N bond required more energy to break (+2.9 kcal/mol)(Chakraborty et al.) For both boat- and chair-HMX, the percent of increase of the N-NO_2 bond in relation to DMNA is greater than for C-N, meaning there is a greater weakening of the N-NO_2 bond. The axial and equatorial N-NO_2 bond in boat- and chair-HMX lengthens by 0.07-0.80% (ΔWBI -2.29-4.19%) and 0.87-1.75% (ΔWBI -2.86-5.62%), respectively, consistent with DFT studies by Chakraborty[35] that determined an N-N homolytic cleavage for HMX has a bond dissociation energy of +39.8 kcal/mol, weaker than the same bond in DMNA (BDE = +46 kcal/mol[147]). Smaller WBI values in HMX for N-NO_2 versus DMNA could be attributed to the stabilization by a hydrogen bonding interaction between the nitro and the methylene group in the ring. A C-N bond distance increase (+1.14%) is only found in the chair-HMX C-N bond adjacent to the equatorial NO_2 group. The strength of C-N

varies from 3.73% weaker to 1.14% stronger in chair-HMX and boat-HMX compared to DMNA. It should also be noted that the boat-phase of HMX is more impact sensitive than chair-phase,[180] which correlates well with longer and weaker N-NO_2 bond distances in boat-HMX. Our WBI results suggest the equatorial N-NO_2 bonds will likely cleave first rather than the C-N bonds found in the backbone of both chair- and boat-HMX.

Bond lengths and strengths for proposed trigger bonds in TNT (C-NO_2) and PETN (O-NO_2) as well as other weak bonds that could break (C-ONO_2 in PETN) upon detonation have been calculated (Tables 2 and 3) and compared to nitrobenzene (NB) and methyl nitrate (MN). The *ortho* -NO_2 has a smaller C-NO_2 WBI (0.893 in A-TNT) than that calculated for *p*-NO_2 (0.900) as expected in aromatic compounds due to steric hindrance present in the *ortho*-position. The reference WBI for the C-NO_2 bond in NB is slightly larger (0.903) with a shorter distance (1.480 Å in NB versus 1.483 Å in TNT). The smaller WBI for *o*-NO_2 can be attributed the additional electron withdrawing –NO_2 groups, while the longer bond length could be due to the steric effect the methyl group. In PETN, both C-ONO_2 and O-NO_2 bonds are compared to MN (O-NO_2: 1.389 Å, WBI = 0.928; C-ONO_2: 1.430 Å; WBI = 0.904), where O-NO_2 is weaker than C-ONO_2. In A- and B-PETN, there is a 0.79% increase in the O-N bond distance (ΔWBI: -2.92%) from the same bond in MN, while the C-ONO_2 bond in both PETN-I and –II increases in length by 0.21-0.28% (ΔWBI: -1.33-1.11%), consistent with an O-N bond cleavage as the possible decomposition pathway. The notion that the C-ONO_2 bond is the weakest is discussed in an AIM study by Zhurova et al.[37] However, AIM analysis pointed to the C-ONO_2 bonds as the trigger bond,[37] inconsistent with experimental observations that the O-NO_2 bond

breaks when subjected to a low energy laser or slow thermal decomposition.[144] This discrepancy may be attributed to a focus on the absolute bond strength versus the strength relative to a reference bond.

Table 6. Comparison of the DFT(M06-2X/TZVP+) and experimental bond distances (Å) and WBIs for X-NO_2 (X = N, C , or O) bond distances (Å) of various polymorphs of RDX, HMX, TNT, and PETN with their experimental impact sensitivities (J).

HEDM	Bond	Functional/Basis Set									
		*B3LYP/ 6-31G**	*B3LYP/ 6-311+G**	*MP2/ 6-31G**	*mPW1PW91/TZVP+*	*M06-2X/ TZVP+*	*Exp*	*WBI*[a]	*Reference Compound*	*ΔWBI(%)*	*I.S.*[b]
AAE-RDX	Ax. N-NO_2	1.432	1.434	1.437	1.418	1.422	1.395	0.961	DMNA	-9.34	
	Eq. N-NO_2	1.402	1.405	1.411	1.392	1.396	1.351	1.000		-4.58	
AAA-RDX	N-NO_2	1.423	1.423	1.428	1.409	1.412	1.413	0.964	DMNA	-8.01 0.00	7.5
AEE-RDX	Ax. N-NO_2	1.441	1.444	1.443	1.428	1.430		0.938	DMNA	-10.58	
	Eq. N-NO_2	1.401	1.404	1.409	1.390	1.395		1.003		-4.39	
chair-HMX	Ax. N-NO_2	1.398	1.401	1.386	1.379	1.376	1.373	1.025	DMNA	-2.29	7.4
	Eq. N-NO_2	1.392	1.393	1.400	1.387	1.387	1.354	1.019		-2.86	
boat-HMX	Ax. N-NO_2	1.403	1.403	1.393	1.391	1.386	1.354	1.005	DMNA	-4.19	<7.4
	Eq. N-NO_2	1.414	1.414	1.415	1.402	1.399	1.367	0.990		-5.62	
A-TNT	C-CH_3	1.509	1.506	1.505	1.496	1.503	1.510	1.041			
	o C-NO_2	1.481	1.485	1.469	1.477	1.482	1.478	0.893	NB	-1.11	
	p C-NO_2	1.475	1.482	1.474	1.475	1.481	1.471	0.900		-0.33	
B-TNT	C-CH_3	1.509	1.506	1.506	1.497	1.503	1.498	1.040			15
	o C-NO_2	1.482	1.485	1.469	1.477	1.483	1.472	0.893	NB	-1.11	
	p C-NO_2	1.475	1.482	1.474	1.474	1.480	1.464	0.900		-0.33	
	o C-NO_2	1.483	1.488	1.469	1.479	1.483	1.475	0.886		-1.88	
A-PETN	O-NO_2	1.432	1.437	1.437	1.414	1.400	1.397	0.901	MN	-2.92	3
B-PETN	O-NO_2			1.437	1.414	1.400	1.386	0.901	MN	-2.92	
	O-NO_2			1.437	1.414	1.400	1.392				

[a]WBI were calculated from optimized geometries using M06-2X/TZVP+
[b]Reference[31]

Table 7. Comparison of the DFT(M06-2X/TZVP+) and experimental bond distances (Å) and WBIs for backbone C-X (X = N, O, C) bond distances (Å) of polymorphs of RDX, HMX, TNT, and PETN with their experimental impact sensitivities (J).

HEDM	Bond	Functional/Basis Set									
		*B3LYP/ 6-31G**	*B3LYP/ 6-311+G**	*MP2/ 6-31G**	*mPW1PW91/ TZVP+*	*M06-2X/ TZVP+*	*Exp*	*WBI*[a]	*Reference Compound*	*ΔWBI(%)*	*I.S.*[b]
AAE-RDX	N_A-C_A	1.449	1.449	1.448	1.438	1.444	1.443	0.983		+1.76	
	N_B-C_A	1.473	1.475	1.470	1.462	1.469	1.464	0.942	DMNA	-2.48	
	N_A-C_B	1.462	1.463	1.462	1.451	1.458	1.458	0.965		-0.10	
AAA-RDX	N-C	1.460	1.461	1.459	1.449	1.455	1.464	0.966	DMNA	0.00	7.5
AEE-RDX	N_A-C_A	1.450	1.450	1.449	1.439	1.445		0.980		+1.45	
	N_B-C_A	1.471	1.472	1.469	1.459	1.466		0.942	DMNA	-2.48	
	N_B-C_B	1.463	1.464	1.463	1.451	1.459		0.958		-0.83	
chair-HMX	N_A-C_A	1.441	1.443	1.438	1.432	1.436	1.455	0.977		+1.14	
	N_B-C_A	1.478	1.479	1.473	1.465	1.471	1.448	0.930	DMNA	-3.73	7.4
	N_B-C_B	1.451	1.453	1.450	1.441	1.444	1.471	0.973		+0.72	
	N_C-C_B	1.460	1.461	1.455	1.449	1.457	1.437	0.943		-2.38	
boat-HMX	N_A-C	1.450	1.450	1.451	1.439	1.450	1.450	0.960	DMNA	-0.62	<7.4
	N_B-C	1.455	1.460	1.445	1.445	1.443	1.471	0.966		0.00	
A-TNT	C_A-C_B	1.411	1.406	1.403	1.399	1.398	1.400	1.363			
	C_B-C_C	1.391	1.387	1.390	1.381	1.381	1.386	1.411			
	C_C-C_D	1.386	1.385	1.387	1.378	1.378	1.373	1.396			15
B-TNT	C_A-C_B	1.413	1.407	1.404	1.400	1.398	1.403	1.363			
	C_B-C_C	1.391	1.387	1.390	1.380	1.381	1.320	1.411			
	C_C-C_D	1.386	1.385	1.387	1.378	1.379	1.388	1.396			
A-PETN	C-O	1.441	1.442	1.441		1.433	1.434	0.892	MN	-1.11	3
B-PETN	C-O	1.442	1.444	1.442		1.434	1.433	0.894	MN	-1.33	

[a]WBI were calculated from optimized geometries using M06-2X/TZVP+
[b]Reference[31]

Table 8. Calculated bond distances (Å) and Wiberg indices (WBI) of standard molecules.

Compound	Bond	$d_{M06\text{-}2X/TZVP+}$ (Å)	WBI*
NB	C-N	1.480	0.903
DMNA	C-N	1.455	0.966
DMNA	N-N	1.375	1.049
AT	C-N	1.362	1.131
MT	N-C	1.449	0.951
MN	O-N	1.389	0.928
MN	C-O	1.430	0.904
MA	C-N	1.460	1.033
DMA	C-N	1.452	1.018
B	C-C	1.389	1.442

*WBI were calculated from optimized geometries using M06-2X/TZVP+

Optimized Structures of Novel HEDMs

The DFT(M06-2X)/TZVP+-optimized geometries of HEDMs **1-7** (Figure 15) are in good agreement with the X-ray structures. C-N bonds to the tetrazole ring were generally more accurately described than the N-NO_2 bonds. For example, in **1** the C-N bond was estimated to be 1.443 Å, only 0.001 Å longer than the same bond in the crystal structure, whereas the calculated N-NO_2 bond (1.378 Å) was slightly longer (+0.009 Å). These differences between the DFT and experimental structures could be attributed to crystal packing forces.

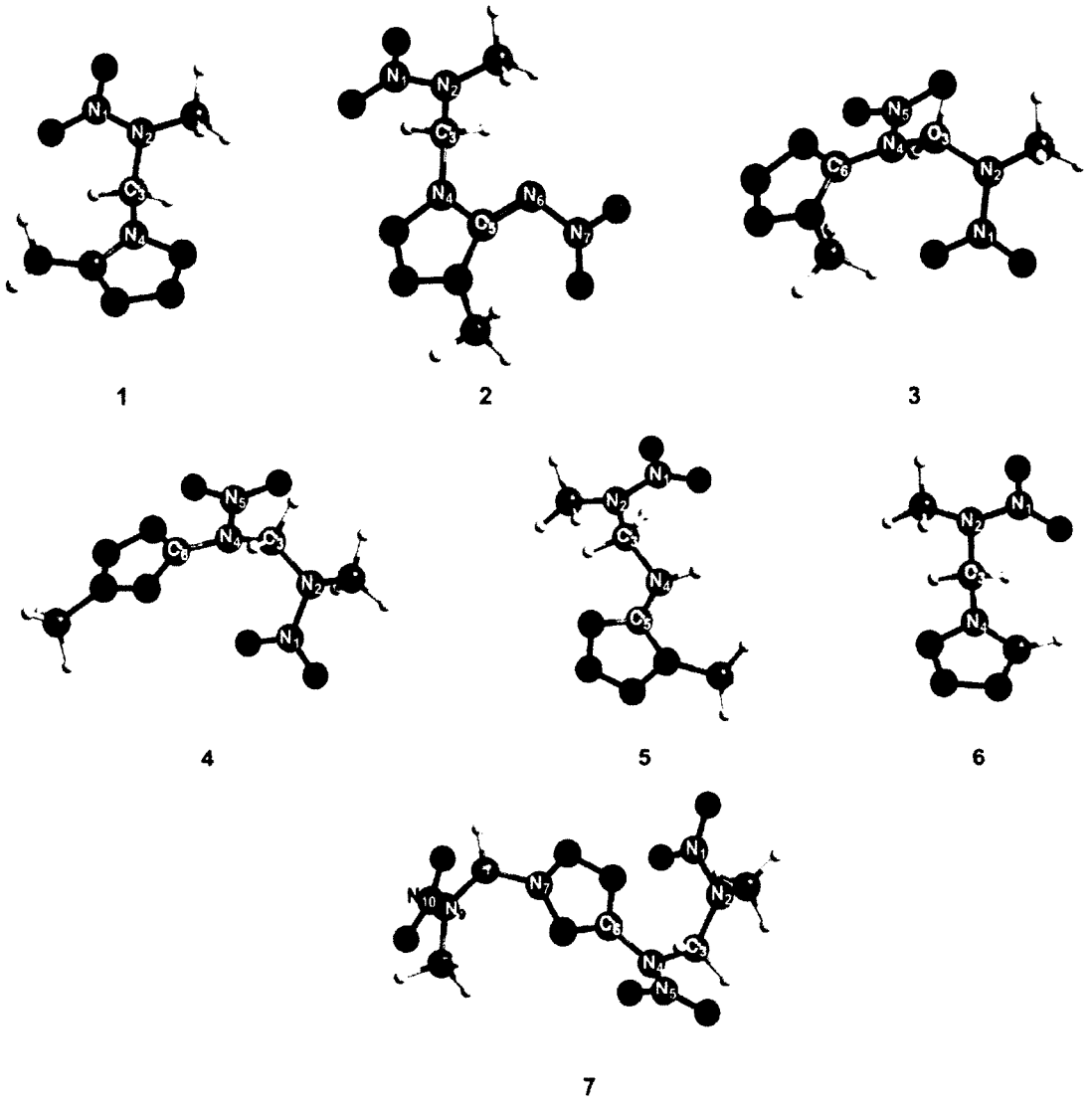

Figure 15. Optimized structures of HEDMS **1**-**7** (M06-2X/TZVP+).

Analysis of Wiberg Bond Indices of Novel HEDMs (Identify Trigger Bonds)

WBIs for **1**-**7** were calculated at the DFT(M06-2X)/TZVP+ level from the optimized structures and compared to standard compounds (Table 9). In the case of RDX, HMX, TNT, and PETN, possible trigger bonds (C-N and X-NO_2 (X = N, C or O)) were identified based on decomposition products and theoretical reaction energies in

explosive materials. Possible fragmentation pathways of **1-7** have been proposed based on decomposition products obtained through mass spectrometry (MS). For example, Fischer et al.[2] proposed several possible fragmentation pathways for structure **7** (scheme 7). From these decomposition products and the assignments of trigger bonds on well-established HEDMs, trigger bonds can be proposed for **1-7**.

Scheme 7. Proposed fragmentation patterns of **7** adapted from Fischer et al.[2] and mass spectrometric results.

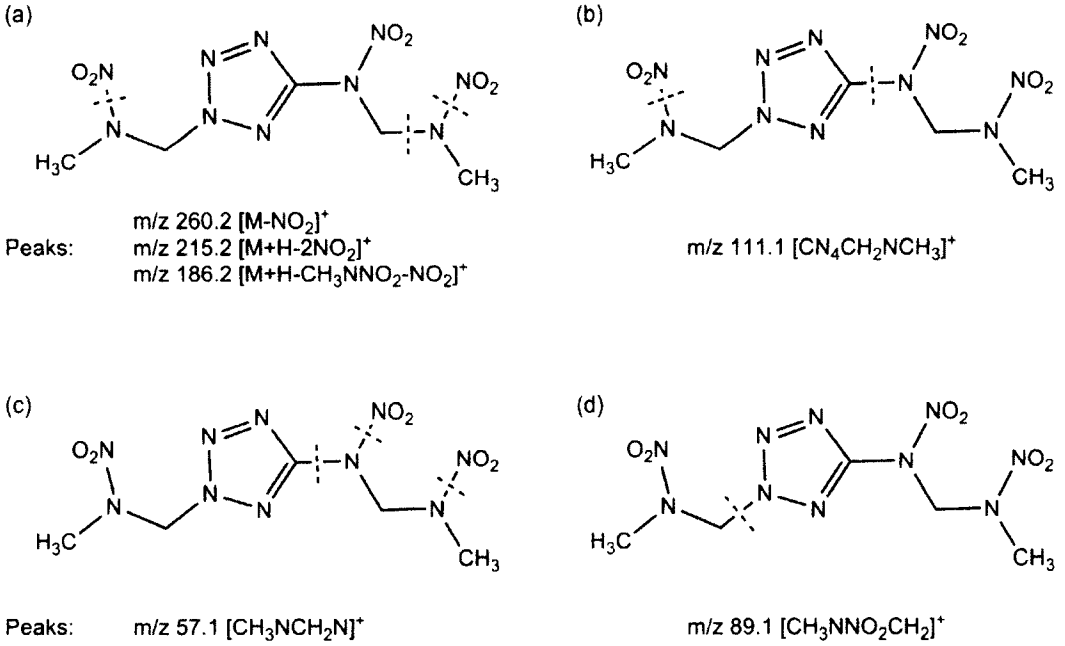

In the mass spectra analysis of **1-7**, the loss of one or more nitro groups (i.e., *m/z* 260 and 215 for **7**) as well as a molecular peak at *m/z* of 89 ($[CH_3NNO_2CH_2]^+$) is observed in each compound. Based on these molecular fragments, it can be assumed that an N-NO_2 bond is likely to break first to initiate detonation. The C-N in the long chain

substituent attached to the tetrazole ring may also be a trigger bond that ruptures in bimolecular collisions as a shockwave propagates through the material. Therefore, WBIs were calculated for N-NO_2 and C-N bonds and compared to standard compounds DMNA, methyl amine (MA), and dimethylamine (DMA), methyltetrazole (MT), and 5-aminotetrazole (AT). Compounds **1** and **6** have only one NO_2 group tethered to the tetrazole by a short side chain. The increase in N-NO_2 bond length (**1**: +0.22% and **6**: +1.02%) and decrease in bond strength (**1**: -0.86% and **6**: -3.15%) is greater relative to DMNA than for cleavage of C-N bonds in the side chain. However, in structures **2-4** and **7** containing 2 or more –NO_2 groups, C-N bonds to tetrazole are weaker relative to the standards AT and MT compared to N-NO_2. Structure **7** has two weak C-N bonds, both attached to the ring (N(4)-C(5) and N(6)-C(7)). The N(6)-C(7) bond is weaker than N(4)-C(5) by ~0.5%, but the length of the bond only increases by 0.27% compared to 2.62%. As shown in Scheme 7d, a single bond break for **7** could possibly occur at N(6)-C(7) to give intermediate $[CH_3NNO_2CH_2]^+$ (*m/z* 89.1), whereas bond cleavage between N(4) and C(5) take place simultaneously with a N-NO_2 break to give a peak of *m/z* 57.1 $(CH_3NCH_2]^+$). Compound **5** has a 4-membered chain attached to the tetrazole with only one –NO_2 group. Although the C(3)-N(4) bond in the chain is weakened the most (-3.05%), the bond distance shortens (-0.41%). Both the N(2)-C(3) and C-N bond attached to the tetrazole are weakened (-1.97% and -1.50%, respectively) from their standards (DMNA and AT, respectively) while a greater bond lengthening is predicted in C(5)-N(4) (+0.66%). Based on small differences in values of bond length and strength, **5** C-N bond cleavage at either site is possible. The difference in the identity of trigger bonds in

structures **1**-**7** could be attributed to the size of the side chains and the number of electron withdrawing $-NO_2$ groups. Shorter side chains with only one $-NO_2$ groups could be more destabilized by the tetrazole ring. Conversely, compounds with two or more $-NO_2$ groups show a shift in electron density away from the C-N bonds that make up the side chain, evidenced by longer and weaker bonds. In addition, destabilization by the ring occurs at the C-N attached to the tetrazole. Based on this evidence, WBIs can be used to determine possible trigger bonds in the breakdown of newly synthesized energetic compounds, which, in the case of these tetrazole-based compounds, are N-NO_2 and C-N bonds. Specifically, trigger bonds for **1** and **6**, smaller molecules with minimal $-NO_2$ groups present, is the N-NO_2 bond. For compounds with more than one $-NO_2$ group (**2**-**4** and **7**), the C-N attached to the tetrazole will likely cleave initially. Larger molecules with only one $-NO_2$ group could cleave at any position in the C-N side chain backbone (**5**). When comparing the trigger bond ΔWBI values of **1**-**7**, the difference in the decrease of bond strength of the trigger bonds and the sensitivity of the explosive shows a positive weak correlation, where smaller impact sensitivities (more sensitive) are observed for compounds with larger ΔWBIs and vice versa. The most insensitive compound, **1** (>100 J), has little change in bond strength (-0.86%), whereas the greater difference in strength is seen in **7** (-12.39%) and is the most sensitive (3 J).[31] Further calculations on other tetrazole-based structures could provide more insight into the correlation between ΔWBI and impact sensitivities.

Table 9. Comparison of the experimental and DFT(M06-2X/TZVP+) bond distances (Å) and WBIs for potential trigger bond of HEDMs **1-7** with experimental impact sensitivities.

HEDM	Bond	d_{exp} (Å)	d_{calc} (Å)	WBI[a]	Reference Compound	ΔWBI (%)	I.S. (J)[b]
1	N(2)-NO_2	1.357	1.378	1.040	DMNA	-0.86	>100
	N(2)-C(3)	1.446	1.448	0.970	DMNA	+0.41	
	N(4)-C(3)	1.459	1.443	0.944	MT	-0.74	
2	N(2)-NO_2	1.365	1.373	1.040	DMNA	-0.86	N/A
	N(2)-C(3)	1.434	1.433	0.991	DMNA	+2.59	
	N(4)-C(3)	1.480	1.458	0.916	MT	-3.68	
	N(6)-NO_2	1.371	1.375	1.055	DMNA	+0.57	
3	N(2)-NO_2	1.346	1.369	1.053	DMNA	+0.38	5
	N(2)-C(3)	1.448	1.442	0.976	DMNA	+1.04	
	N(4)-C(3)	1.458	1.463	0.930	DMNA	-3.73	
	N(4)-NO_2	1.395	1.395	0.967	DMNA	-7.82	
	N(4)-C(6)	1.399	1.396	0.998	AT	-11.76	
4	N(2)-NO_2	1.349	1.384	1.026	DMNA	-2.19	8
	N(2)-C(3)	1.440	1.442	0.978	DMNA	+1.24	
	N(4)-C(3)	1.459	1.464	0.934	DMNA	-3.31	
	N(4)-NO_2	1.403	1.400	0.981	DMNA	-6.48	
	N(4)-C(6)	1.459	1.464	0.994	AT	-12.11	
5	N(2)-NO_2	1.344	1.355	1.091	DMNA	+4.00	40
	N(2)-C(3)	1.463	1.457	0.947	DMNA	-1.97	
	N(4)-C(3)	1.436	1.446	0.987	DMA	-3.05	
	N(4)-C(5)	1.354	1.371	1.114	AT	-1.50	
6	N(2)-NO_2	1.340	1.389	1.016	DMNA	-3.15	15
	N(2)-C(3)	1.442	1.443	0.981	DMNA	+1.55	
	N(4)-C(3)	1.456	1.456	0.932	MT	-2.00	
7	N(2)-NO_2	1.399	1.387	1.024	DMNA	-2.38	2
	N(2)-C(3)	1.458	1.442	0.983	DMA	-3.82	
	N(4)-C(3)	1.478	1.468	0.931	DMA	-8.90	
	N(4)-NO_2	1.424	1.411	0.964	DMNA	-8.10	
	N(4)-C(6)	1.404	1.401	0.996	AT	-11.94	
	N(7)-C(8)	1.478	1.464	0.905	MA	-12.39	
	N(9)-C(8)	1.448	1.432	1.000	DMNA	+3.52	
	N(9)-NO_2	1.407	1.394	1.000	DMNA	-4.67	

[a]WBI were calculated from optimized geometries using M06-2X/TZVP+
[b]Reference[2]

Conclusions

Decomposition mechanisms have been thoroughly investigated and proposed for RDX, HMX, TNT, and PETN based on potential trigger bonds, bonds which are the most likely to break to initiate decomposition of the energetic material. Two bonds have been identified as possible trigger bonds in nitro-containing explosives: X-NO_2

(X=N/C/O) and C-N. The use of Wiberg bond indices to characterize strengths of potential trigger bonds opens new means of identifying possible trigger bonds in HEDMs. Based on this study, the differences in WBIs between RDX, HMX, TNT, and PETN and reference compounds support the most weakened bond is most likely to break. The use of these values to determine bond strength can be applied to novel energetic materials where decomposition mechanisms are unknown and limited experimental evidence exists. Newly synthesized explosives **1** and **6** have weak N-NO_2 bonds, whereas more complex compounds **2-5** and **7** have weak C-N bonds that are attached to the ring. Differences can be attributed to the chain length of the substituent and the number of $-NO_2$ groups. Weak correlations have been observed between ΔWBI and impact sensitivities, where the larger decreases in WBIs from reference compounds are more shock sensitive. However, further investigations on a larger database of HEDMs are required to draw conclusions.

CHAPTER 5

CONCLUSION

The growth and development of military science and technology is dependent on understanding the fundamental chemistry of pernicious species like chemical warfare agents (CWAs) and high energy density materials (HEDMs). The toxicity of many CWAs, such how arsenicals like lewisite inhibit sulfur-containing proteins as well as the initial step in the explosive decomposition of HEDMs are important mechanisms with military applications that are poorly understood. Computational methods such as density functional theory (DFT) can be used to understand the mechanisms of these complicated systems for which experimental evidence cannot be easily obtained. In biologically relevant mechanisms of As(III), density functional theory-solvent assisted proton exchange (DFT-SAPE) was used to model reactions that take place in aqueous phase, mimicking solvent interactions that take place under biological conditions. When determining weak bonds in explosive materials where the reaction is too rapid for experimental monitoring, Wiberg bond indices (WBIs) were used to characterize bonds that could potentially initiate decomposition.

Arsenic is a naturally occurring environmental toxicant that can cause disruption of enzyme activity through binding to sulfhydryl-containing biomolecules. An antagonistic relationship between arsenic and selenium, an essential trace element, exists based on the formation of selenobis(S-glutathionyl)arsinium $[(GS)2AsSe]^-$ which is safely excreted in urine. DFT-SAPE calculations predict that the first two steps in the

reduction of arsenite with thiol are slow, with formation of the final product, $As(SR)_3$, faster, consistent with experimental observation. The formation of $[(GS)2AsSe]^-$ is predicted through the attack of selenide on reduced arsenite intermediate $(RS)_2As(OH)$ due to a lower barrier height relative to competing reactions. This DFT-SAPE model is a good basis for future modeling of the release of Zn^{2+} in zinc finger proteins by arsenite and other arsenic compounds as well as the reaction with other sulfhydryl-containing proteins. However, SAPE calculations must be extended to hybrid quantum mechanics/molecular mechanics (QM/MM) methods to include the effect of the protein on the interaction between As(III) and Cys residues and more accurately represent the biological mechanism.

Lewisite, an arsenic-based vesicant, binds to the dithiol of the lipoic acid substrate of pyruvate dehydrogenase, inhibiting its function. The most common antidote, British anti-lewisite (BAL), is predicted by DFT-SAPE to form a stable ring product rapidly, consistent with the almost immediate protection and reversal of the harmful effects of lewiste under experimental conditions. Understanding the mechanism of the rapid chelation of As(III) by BAL can lead to the development of new, safer antidotes which compete with dithiol-containing proteins in order to repair and reverse damage caused through the inhibition of the enzyme. Smaller scale models of reactions are used to lower computational costs caused by higher degrees of freedom and increased number of atoms that are present in larger systems. Future studies can use these small models as the basis for larger-scale reactions using QM/MM methods to include the entire protein and larger hydration shells to help illustrate the role of

solvent interaction and obtain a more complete picture of the interaction of chemical warfare agents with biological systems.

For HEDMs, trigger bonds, or bonds that break in order to initiate decomposition, have been characterized using WBI, which describes bond strength. Potential trigger bonds are typically X-NO_2 (X = C, N and O) or C-N bonds found in substituents that are weak compared to similar bonds with the same hybridization in structurally similar reference compounds. Relative WBI values indicate that the N-NO_2 bond in RDX (axial position), HMX (axial position) and TNT (*ortho* position) and the O-NO_2 bond in PETN are likely trigger bonds, consistent with previous theoretical and experimental studies. The degree of weakening of potential trigger bonds could be used to determine correlations between the magnitude of ΔWBI and impact sensitivities. Insufficient data on the use of WBI to predict impact sensitivities opens an avenue to be explored. Large databases of chemically similar explosives, like those which contain the same functional groups, will be required to determine if any relationship exists between a decrease in WBI values from reference compounds and potential trigger bonds in explosives and their impact sensitivities. Better experimental methods for determining impact sensitivities should also be explored. The drop hammer test performed to determine if an explosive is more sensitive to stimuli than a reference explosive is not very accurate and new tests to quantify impact sensitivities of explosives should be developed.[181] Nevertheless, DFT has been shown to be a valuable tool in the characterization of proposed trigger bonds in established HEDMs and can be used further to provide insight for novel HEDMs.

REFERENCES

(1) Gailer, J., George, G. N., Pickering, I. J., Buttigieg, G. A., Denton, M. B., and Glass, R. S. (2002) Synthesis, X-ray absorption spectroscopy and purification of the seleno-bis (S-glutathionyl) arsinium anion from selenide, arsenite and glutathione. *J. Organomet. Chem.*, *650*, 108-113.

(2) Fischer, N., Karaghiosoff, K., Klapötke, T. M., and Stierstorfer, J. (2010) New energetic materials featuring tetrazoles and nitramines–synthesis, characterization and properties. *Z. Anorg. Allg. Chem.*, *636*, 735-749.

(3) Klapötke, T. M., Ed. (2007) *High Energy Density Materials*, Vol. 125, Springer, Berlin

(4) Bissen, M., and Frimmel, F. H. (2003) Arsenic - a review. - Part 1: Occurrence, toxicity, speciation, mobility. *Acta Hydrochim. Hydrobiol.*, *31*, 9-18.

(5) Mandal, B. K., and Suzuki, K. T. (2002) Arsenic round the world: a review. *Talanta*, *58*, 201-235.

(6) Squibb, K. S., and Fowler, B. A. (1983) The toxicity of arsenic and its compounds, In *Biological and Environmental Effects of Arsenic* (Fowler, B. A., Ed.) pp 233-269, Elsevier, New York.

(7) Peters, R., Sinclair, H., and Thompson, R. (1946) An analysis of the inhibition of pyruvate oxidation by arsenicals in relation to the enzyme theory of vesication. *Biochem. J.*, *40*, 516.

(8) Peters, R. A., and Wakelin, R. W. (1946) Observations on the relation between sulphydryl groups and pyruvate oxidation in brain tissue. *Biochem. J.*, *40*, 513-516.

(9) Adams, G. F., and Shaw Jr, R. W. (1992) Chemical reactions in energetic materials. *Ann. Rev. Phys. Chem.*, *43*, 311-340.

(10) Romano, J. A., Lukey, B. J., and Salem, H. (2007) *Chemical warfare agents: chemistry, pharmacology, toxicology, and therapeutics*. CRC Press, Boca Raton, FL.

(11) Marrs, T. T., Maynard, R. L., and Sidell, F. (2007) *Chemical warfare agents: toxicology and treatment*. John Wiley & Sons, Chichester, West Sussex, England.

(12) Marrs, T. C., and Maynard, R. L. (2007) Organic Arsenicals, In *Chemical Warfare Agents: Toxicology and Treatment* pp 467-475, John Wiley & Sons, Chichester, West Sussex, England.

(13) Salem, H., Ternay Jr, A. L., and Smart, J. K. (2008) Brief history and use of chemical warfare agents in warfare and terrorism, In *Chemical Warfare Agents: Chemistry, Pharmacology, Toxicology, and Therapeutics* (Romano Jr, J., Luckey, B., and Salem, H., Eds.) pp 1-17, CRC Press, Boca Raton, FL.

(14) Khan, M., and Ho, Y. (2011) Arsenic in drinking water: a review on toxicological effects, mechanism of accumulation and remediation. *Asian J. Chem.*, *23*, 1889-1901.

(15) Smith, A. H., Hopenhaynrich, C., Bates, M. N., Goeden, H. M., Hertzpicciotto, I., Duggan, H. M., Wood, R., Kosnett, M. J., and Smith, M. T. (1992) Cancer risks from arsenic in drinking-water. *Environ. Health Perspect., 97*, 259-267.

(16) Vilensky, J. A. (2005) *Dew of death: the story of lewisite, America's World War I weapon of mass destruction*. Indiana University Press, Bloomington, IN.

(17) Vilensky, J. A., and Redman, K. (2003) British anti-Lewisite (dimercaprol): an amazing history. *Ann. Emerg. Med., 41*, 378-383.

(18) Peters, R. A., Stocken, L. A., and Thompson, R. (1945) British anti-lewisite (BAL). *Nature, 156*, 616.

(19) Stocken, L., and Thompson, R. (1946) British anti-lewisite: 2. Dithiol compounds as antidotes for arsenic. *Biochem. J., 40*, 535.

(20) Bull, J. M. (2005) Special Report, Part 1: The Deadliness Below, In *Daily Press*, Newport News, VA.

(21) Lesho, M. E., Dorsey, M. D., and Bunner, D. (1998) Feces, dead horses, and fleas. Evolution of the hostile use of biological agents. *West. J. Med., 168*, 512-516.

(22) Radabaugh, T. R., Sampayo-Reyes, A., Zakharyan, R. A., and Aposhian, H. V. (2002) Arsenate reductase II. Purine nucleoside phosphorylase in the presence of dihydrolipoic acid is a route for reduction of arsenate to arsenite in mammalian systems. *Chem. Res. Toxicol., 15*, 692-698.

(23) Aposhian, H. V., and Aposhian, M. M. (2005) Arsenic Toxicology: Five Questions†. *Chem. Res. Toxicol., 19*, 1-15.

(24) Scott, N., Hatlelid, K. M., MacKenzie, N. E., and Carter, D. E. (1993) Reactions of arsenic(III) and arsenic(V) species with glutathione. *Chem. Res. Toxicol.*, *6*, 102-106.

(25) Hu, Y., Su, L., and Snow, E. T. (1998) Arsenic toxicity is enzyme specific and its affects on ligation are not caused by the direct inhibition of DNA repair enzymes. *Mutat. Res.-DNA Repair*, *408*, 203-218.

(26) Szinicz, L., and Forth, W. (1988) Effect of As2O3 on gluconeogenesis. *Arch. Toxicol.*, *61*, 444-449.

(27) Witkiewicz-Kucharczyk, A., and Bal, W. (2006) Damage of zinc fingers in DNA repair proteins, a novel molecular mechanism in carcinogenesis. *Toxicol. Lett.*, *162*, 29-42.

(28) Schwerdtle, T., Walter, I., and Hartwig, A. (2003) Arsenite and its biomethylated metabolites interfere with the formation and repair of stable BPDE-induced DNA adducts in human cells and impair XPAzf and Fpg. *DNA Repair*, *2*, 1449-1463.

(29) Moxon, A. L., and DuBois, K. P. (1939) The Influence of Arsenic and Certain Other Elements on the Toxicity of Seleniferous Grains: Three Figures. *J. Nutr.*, *18*, 447-457.

(30) Gailer, J., George, G. N., Pickering, I. J., Prince, R. C., Ringwald, S. C., Pemberton, J. E., Glass, R. S., Younis, H. S., DeYoung, D. W., and Aposhian, H. V. (2000) A metabolic link between arsenite and selenite: The seleno-bis(S-glutathionyl) arsinium ion. *J. Am. Chem. Soc.*, *122*, 4637-4639.

(31) Akhavan, J. (2011) *The chemistry of explosives*. 3rd ed., The Royal Society of Chemistry, Cambridge, UK.

(32) Meyers, S., and Shanley, E. S. (1990) Industrial explosives - a brief history of their development and use. *J. Haz. Mat.*, *23*, 183-201.

(33) Kamlet, M. J., and Adolph, H. G. (1979) The relationship of impact sensitivity with structure of organic high explosives. II. Polynitroaromatic explosives. *Prop. Explos. Pyrotech.*, *4*, 30-34.

(34) Melius, C. F., and Binkley, J. S. (1988) Thermochemistry of the decomposition of nitramines in the gas phase. *Symp. Int. Combust.*, *21*, 1953-1963.

(35) Chakraborty, D., Muller, R. P., Dasgupta, S., and Goddard, W. A. (2001) Mechanism for unimolecular decomposition of HMX (1,3,5,7-tetranitro-1,3,5,7-tetrazocine), an ab initio study. *J. Phys. Chem. A*, *105*, 1302-1314.

(36) Moraes, T. F., and Borges, I. (2011) Nuclear fukui functions and the deformed atoms in molecules representation of the electron density: application to gas-phase RDX (hexahydro-1, 3, 5-trinitro-1, 3, 5-triazine) electronic structure and decomposition. *Int. J. Quantum Chem.*, *111*, 1444-1452.

(37) Zhurova, E. A., Stash, A. I., Tsirelson, V. G., Zhurov, V. V., Bartashevich, E. V., Potemkin, V. A., and Pinkerton, A. A. (2006) Atoms-in-molecules study of intra- and intermolecular bonding in the pentaerythritol tetranitrate crystal. *J. Am. Chem. Soc.*, *128*, 14728-14734.

(38) Byrd, E. F. C., and Rice, B. M. (2007) Ab initio study of compressed 1,3,5,7-tetranitro-1,3,5,7-tetraazacyclooctane (HMX), cyclotrimethylenetrinitramine

(RDX), 2,4,6,8,10,12-hexanitrohexaazaisowurzitane (CL-20), 2,4,6-trinitro-1,3,5-benzenetriamine (TATB), and pentaerythritol tetranitrate (PETN). *J. Phys. Chem. C*, *111*, 2787-2796.

(39) Strachan, A., van Duin, A. C. T., Chakraborty, D., Dasgupta, S., and Goddard, W. A. (2003) Shock waves in high-energy materials: the initial chemical events in nitramine RDX. *Phys. Rev. Lett.*, *91*, 098301.

(40) Levine, I. N. (2009) *Quantum chemistry*. 6th ed., Pearson Prentice Hall, Upper Saddle River, NJ.

(41) Vosko, S. H., Wilk, L., and Nusair, M. (1980) Accurate spin-dependent electron liquid correlation energies for local spin density calculations: a critical analysis. *Can. J. Phys.*, *58*, 1200-1211.

(42) Becke, A. D. (1988) Density-functional exchange-energy approximation with correct asymptotic behavior. *Phys. Rev. A*, *38*, 3098-3100.

(43) Lee, C., Yang, W., and Parr, R. G. (1988) Development of the Colle-Salvetti correlation-energy formula into a functional of the electron density. *Phys. Rev. B*, *37*, 785-789.

(44) Becke, A. D. (1993) Density-functional thermochemistry. III. The role of exact exchange. *J. Chem. Phys.*, *98*, 5648-5652.

(45) Boys, S. F. (1950) Electronic wave functions. I. A general method of calculation for the stationary states of any molecular system. *Proc. R. Soc. A*, *200*, 542-554.

(46) Ditchfield, R., Hehre, W. J., and Pople, J. A. (1971) Self-consistent molecular-orbital methods. IX. An extended gaussian-type basis for molecular-orbital studies of organic molecules. *J. Chem. Phys.*, *54*, 724-728.

(47) Clark, T., Chandrasekhar, J., Spitznagel, G. W., and Schleyer, P. V. R. (1983) Efficient diffuse function-augmented basis sets for anion calculations. III. The 3-21+G basis set for first-row elements, Li–F. *J. Comput. Chem.*, *4*, 294-301.

(48) Frisch, M. J., Pople, J. A., and Binkley, J. S. (1984) Self-consistent molecular orbital methods 25. Supplementary functions for Gaussian basis sets. *J. Chem. Phys.*, *80*, 3265-3269.

(49) Woon, D. E., and Dunning, T. H. (1993) Gaussian basis sets for use in correlated molecular calculations. III. The atoms aluminum through argon. *J. Chem. Phys.*, *98*, 1358-1371.

(50) Schäfer, A., Huber, C., and Ahlrichs, R. (1994) Fully optimized contracted Gaussian basis sets of triple zeta valence quality for atoms Li to Kr. *J. Chem. Phys.*, *100*, 5829-5835.

(51) Barceloux, D. G. (1999) Selenium. *Clin. Toxicol.*, *37*, 145-172.

(52) Valko, M., Morris, H., and Cronin, M. (2005) Metals, toxicity and oxidative stress. *Curr. Med. Chem.*, *12*, 1161-1208.

(53) Hamilton, S. J. (2004) Review of selenium toxicity in the aquatic food chain. *Sci. Total Environ.*, *326*, 1-31.

(54) (2009) National Primary Drinking Water Regulations, (Agency, U. S. E. P., Ed.).

(55) Spallholz, J. E. (1994) On the nature of selenium toxicity and carcinostatic activity. *Free Rad. Biol. Med.*, *17*, 45-64.

(56) Ammar, E. M., and Couri, D. (1981) Acute toxicity of sodium selenite and selenomethionine in mice after ICV or IV administration. *Neurotoxicology*, *2*, 383-386.

(57) Ralston, N. V., Unrine, J., and Wallschläger, D. (2008) Biogeochemistry and Analysis of Selenium and its Species, North American Metals Council, Washington, DC.

(58) Neff, J. M. (1997) Ecotoxicology of arsenic in the marine environment. *Environ. Toxicol. Chem.*, *16*, 917-927.

(59) Schrauzer, G. N. (2000) Selenomethionine: A Review of Its Nutritional Significance, Metabolism and Toxicity. *J. Nutr.*, *130*, 1653-1656.

(60) Dumont, E., Vanhaecke, F., and Cornelis, R. (2006) Selenium speciation from food source to metabolites: a critical review. *Anal. Bioanal. Chem.*, *385*, 1304-1323.

(61) Tarze, A., Dauplais, M., Grigoras, I., Lazard, M., Ha-Duong, N. T., Barbier, F., Blanquet, S., and Plateau, P. (2007) Extracellular production of hydrogen selenide accounts for thiol-assisted toxicity of selenite against Saccharomyces cerevisiae. *J. Biol. Chem.*, *282*, 8759-8767.

(62) Qin, X.-J., Hudson, L. G., Liu, W., Ding, W., Cooper, K. L., and Liu, K. J. (2008) Dual Actions Involved in Arsenite-Induced Oxidative DNA Damage. *Chem. Res. Toxicol.*, *21*, 1806-1813.

(63) Larabee, J. L., Hocker, J. R., Hanas, R. J., Kahn, F. M., and Hanas, J. S. (2002) Inhibition of zinc finger protein–DNA interactions by sodium selenite. *Biochem. Pharmacol.*, *64*, 1757-1765.

(64) Hartwig, A., Groblinghoff, U. D., Beyersmann, D., Natarajan, A. T., Filon, R., and Mullenders, L. H. F. (1997) Interaction of arsenic(III) with nucleotide excision repair in UV-irradiated human fibroblasts. *Carcinogenesis*, *18*, 399-405.

(65) Hartwig, A., Pelzer, A., Asmuss, M., and Burkle, A. (2003) Very low concentrations of arsenite suppress poly(adp-ribosyl)ation in mammalian cells. *Int. J. Cancer*, *104*, 1-6.

(66) Hartwig, A., Blessing, H., Schwerdtle, T., and Walter, I. (2003) Modulation of DNA repair processes by arsenic and selenium compounds. *Toxicology*, *193*, 161-169.

(67) Ding, W., Liu, W. L., Cooper, K. L., Qin, X. J., Bergo, P. L. D., Hudson, L. G., and Liu, K. J. (2009) Inhibition of Poly(ADP-ribose) Polymerase-1 by Arsenite Interferes with Repair of Oxidative DNA Damage. *J. Biol. Chem.*, *284*, 6809-6817.

(68) Quintal, S. M., Antonia dePaula, Q., and Farrell, N. P. (2011) Zinc finger proteins as templates for metal ion exchange and ligand reactivity. Chemical and biological consequences. *Metallomics*, *3*, 121-139.

(69) Blessing, H., Kraus, S., Heindl, P., Bal, W., and Hartwig, A. (2004) Interaction of selenium compounds with zinc finger proteins involved in DNA repair. *Eur. J. Biochem.*, *271*, 3190-3199.

(70) Styblo, M., Del Razo, L. M., Vega, L., Germolec, D. R., LeCluyse, E. L., Hamilton, G. A., Reed, W., Wang, C., Cullen, W. R., and Thomas, D. J. (2000) Comparative

toxicity of trivalent and pentavalent inorganic and methylated arsenicals in rat and human cells. *Arch. Toxicol.*, *74*, 289-299.

(71) Lin, S., Cullen, W. R., and Thomas, D. J. (1999) Methylarsenicals and Arsinothiols Are Potent Inhibitors of Mouse Liver Thioredoxin Reductase. *Chem. Res. Toxicol.*, *12*, 924-930.

(72) Meister, A. (1988) Glutathione metabolism and its selective modification. *J. Biol. Chem.*, *263*, 17205-17208.

(73) Delnomdedieu, M., Basti, M. M., Otvos, J. D., and Thomas, D. J. (1994) Reduction and binding of arsenate and dimethylarsinate by glutathione - A magnetic-resonance study. *Chem.-Biol. Interact.*, *90*, 139-155.

(74) Björnstedt, M., Kumar, S., and Holmgren, A. (1992) Selenodiglutathione is a highly efficient oxidant of reduced thioredoxin and a substrate for mammalian thioredoxin reductase. *J. Biol. Chem.*, *267*, 8030-8034.

(75) Jornstedt, M. B., Kumar, S., and Holmgren, A. (1995) [22] Selenite and selenodiglutathione: Reactions with thioredoxin systems. *Methods Enzymol.*, *252*, 209-219.

(76) Ganther, H. E. (1971) Reduction of the selenotrisulfide derivative of glutathione to a persulfide analog by gluthathione reductase. *Biochemistry*, *10*, 4089-4098.

(77) Dubois, K. P., Moxon, A. L., and Olson, O. E. (1940) Further studies on the effective ness of arsenic in preventing selenium poisoning. *J. Nutr.*, *19*, 477-482.

(78) Levander, O., and Argrett, L. (1969) Effects of arsenic, mercury, thallium, and lead on selenium metabolism in rats. *Toxicol. Appl. Pharmacol.* , *14*, 308-314.

(79) Levander, O., and Baumann, C. (1966) Selenium metabolism: VI. Effect of arsenic on the excretion of selenium in the bile. *Toxicol. Appl. Pharmacol.*, *9*, 106-115.

(80) Levander, O. A., and Baumann, C. A. (1966) Selenium metabolism: V. Studies on the distribution of selenium in rats given arsenic. *Toxicol. Appl. Pharmacol.*, *9*, 98-105.

(81) Hsieh, H. S., and Ganther, H. E. (1975) Acid-volatile selenium formation catalyzed by glutathione reductase. *Biochemistry*, *14*, 1632-1636.

(82) Bayse, C. A. (2007) DFT Study of the Glutathione Peroxidase-Like Activity of Phenylselenol Incorporating Solvent-Assisted Proton Exchange. *J. Phys. Chem. A*, *111*, 9070-9075.

(83) Bayse, C. A. (2011) Transition states for cysteine redox processes modeled by DFT and solvent-assisted proton exchange. *Org. Biomol. Chem.*, *9*, 4748-4751.

(84) Steudel, R., and Steudel, Y. (2009) Microsolvation of Thiosulfuric Acid and Its Tautomeric Anions [HSSO3]− and [SSO2 (OH)]− Studied by B3LYP-PCM and G3X (MP2) Calculations. *J. Phys. Chem. A*, *113*, 9920-9933.

(85) Xue, Y., Kim, C. K., Guo, Y., Xie, D. Q., and Yan, G. S. (2005) DFT study and Monte Carlo simulation on proton transfers of 2-amino-2-oxazoline, 2-amino-2-thiazoline, and 2-amino-2-imidazoline in the gas phase and in water. *J. Comput. Chem.*, *26*, 994-1005.

(86) Frisch, M. J. T., G. W.; Schlegel, H. B.; Scuseria, G. E.; Robb, M. A.; Cheeseman, J. R.; Montgomery, Jr., J. A.; Vreven, T.; Kudin, K. N.; Burant, J. C.; Millam, J. M.; Iyengar, S. S.; Tomasi, J.; Barone, V.; Mennucci, B.; Cossi, M.; Scalmani, G.; Rega,

N.; Petersson, G. A.; Nakatsuji, H.; Hada, M.; Ehara, M.; Toyota, K.; Fukuda, R.; Hasegawa, J.; Ishida, M.; Nakajima, T.; Honda, Y.; Kitao, O.; Nakai, H.; Klene, M.; Li, X.; Knox, J. E.; Hratchian, H. P.; Cross, J. B.; Bakken, V.; Adamo, C.; Jaramillo, J.; Gomperts, R.; Stratmann, R. E.; Yazyev, O.; Austin, A. J.; Cammi, R.; Pomelli, C.; Ochterski, J. W.; Ayala, P. Y.; Morokuma, K.; Voth, G. A.; Salvador, P.; Dannenberg, J. J.; Zakrzewski, V. G.; Dapprich, S.; Daniels, A. D.; Strain, M. C.; Farkas, O.; Malick, D. K.; Rabuck, A. D.; Raghavachari, K.; Foresman, J. B.; Ortiz, J. V.; Cui, Q.; Baboul, A. G.; Clifford, S.; Cioslowski, J.; Stefanov, B. B.; Liu, G.; Liashenko, A.; Piskorz, P.; Komaromi, I.; Martin, R. L.; Fox, D. J.; Keith, T.; Al-Laham, M. A.; Peng, C. Y.; Nanayakkara, A.; Challacombe, M.; Gill, P. M. W.; Johnson, B.; Chen, W.; Wong, M. W.; Gonzalez, C.; and Pople, J. A. (2003) Gaussian 03, Gaussian, Inc., Wallingford, CT.

(87) Frisch, M. J. T., G. W.; Schlegel, H. B.; Scuseria, G. E.; Robb, M. A.; Cheeseman, J. R.; Scalmani, G.; Barone, V.; Mennucci, B.; Petersson, G. A.; Nakatsuji, H.; Caricato, M.; Li, X.; Hratchian, H. P.; Izmaylov, A. F.; Bloino, J.; Zheng, G.; Sonnenberg, J. L.; Hada, M.; Ehara, M.; Toyota, K.; Fukuda, R.; Hasegawa, J.; Ishida, M.; Nakajima, T.; Honda, Y.; Kitao, O.; Nakai, H.; Vreven, T.; Montgomery, J. A., Jr.; Peralta, J. E.; Ogliaro, F.; Bearpark, M.; Heyd, J. J.; Brothers, E.; Kudin, K. N.; Staroverov, V. N.; Kobayashi, R.; Normand, J.; Raghavachari, K.; Rendell, A.; Burant, J. C.; Iyengar, S. S.; Tomasi, J.; Cossi, M.; Rega, N.; Millam, M. J.; Klene, M.; Knox, J. E.; Cross, J. B.; Bakken, V.; Adamo, C.; Jaramillo, J.; Gomperts, R.; Stratmann, R. E.; Yazyev, O.; Austin, A. J.; Cammi, R.; Pomelli, C.; Ochterski, J. W.;

Martin, R. L.; Morokuma, K.; Zakrzewski, V. G.; Voth, G. A.; Salvador, P.; Dannenberg, J. J.; Dapprich, S.; Daniels, A. D.; Farkas, Ö.; Foresman, J. B.; Ortiz, J. V.; Cioslowski, J.; Fox. (2009) Gaussian 09, Gaussian, Inc., Wallingford, CT.

(88) Adamo, C., and Barone, V. (1998) Exchange functionals with improved long-range behavior and adiabatic connection methods without adjustable parameters: the mPW and mPW1PW models. *J. Chem. Phys.*, *108*, 664-675.

(89) Thom. H. Dunning, J. (1971) Gaussian Basis Functions for Use in Molecular Calculations. III. Contraction of (10s6p) Atomic Basis Sets for the First-Row Atoms. *J. Chem. Phys.*, *55*, 716-723.

(90) Hurley, M., Pacios, L. F., Christiansen, P., Ross, R., and Ermler, W. (1986) Ab initio relativistic effective potentials with spin-orbit operators. II. K through Kr. *J. Chem. Phys.*, *84*, 6840.

(91) Hay, P. J., and Wadt, W. R. (1985) Ab initio effective core potentials for molecular calculations. Potentials for K to Au including the outermost core orbitals. *J. Chem. Phys.*, *82*, 299.

(92) Thom H. Dunning, J. (1970) Gaussian Basis Functions for Use in Molecular Calculations. I. Contraction of (9s5p) Atomic Basis Sets for the First-Row Atoms. *J. Chem. Phys.*, *53*, 2823-2833.

(93) Peng, C., Ayala, P. Y., Schlegel, H. B., and Frisch, M. J. (1996) Using redundant internal coordinates to optimize equilibrium geometries and transition states. *J. Comput. Chem.*, *17*, 49-56.

(94) Peng, C., and Schlegel, H. B. (1993) Combining synchronous transit and quasi-Newton methods to find transition states. *Israel J. Chem.*, *33*, 449-454.

(95) Tomasi, J., Mennucci, B., and Cammi, R. (2005) Quantum Mechanical Continuum Solvation Models. *Chem. Rev.*, *105*, 2999-3094.

(96) Bondi, A. (1964) van der Waals volumes and radii. *J. Phys. Chem.*, *68*, 441-451.

(97) Spuches, A. M., Kruszyna, H. G., Rich, A. M., and Wilcox, D. E. (2005) Thermodynamics of the As(III)−Thiol Interaction: Arsenite and Monomethylarsenite Complexes with Glutathione, Dihydrolipoic Acid, and Other Thiol Ligands. *Inorg. Chem.*, *44*, 2964-2972.

(98) Miot, J., Morin, G., Skouri-Panet, F., Ferard, C., Aubry, E., Briand, J., Wang, Y., Ona-Nguema, G., Guyot, F., and Brown, G. E. (2008) XAS study of arsenic coordination in Euglena gracilis exposed to arsenite. *Environ. Sci. Technol.*, *42*, 5342-5347.

(99) Suzuki, N., Naranmandura, H., Hirano, S., and Suzuki, K. T. (2008) Theoretical Calculations and Reaction Analysis on the Interaction of Pentavalent Thioarsenicals with Biorelevant Thiol Compounds. *Chem. Res. Toxicol.*, *21*, 550-553.

(100) Kala, S. V., Neely, M. W., Kala, G., Prater, C. I., Atwood, D. W., Rice, J. S., and Lieberman, M. W. (2000) The MRP2/cMOAT Transporter and Arsenic-Glutathione Complex Formation Are Required for Biliary Excretion of Arsenic. *J. Biol. Chem.*, *275*, 33404-33408.

(101) Raab, A., Meharg, A. A., Jaspars, M., Genney, D. R., and Feldmann, J. (2004) Arsenic-glutathione complexes-their stability in solution and during separation by different HPLC modes. *J. Anal. At. Spectrom.*, *19*, 183-190.

(102) Harper, L. K., Antony, S., and Bayse, C. A. (2014) Thiol Reduction of Arsenite and Selenite: DFT Modeling of the Pathways to an As–Se Bond. *Chem. Res. Toxicol.*, *27*, 2119-2127.

(103) Seko, Y., Saito, Y., Kitahara, J., and Imura, N. (1989) Active Oxygen Generation by the Reaction of Selenite with Reduced Glutathione in Vitro, In *Selenium in Biology and Medicine* (Wendel, A., Ed.) pp 70-73, Springer Berlin.

(104) Maynard, R. L. (2007) Mustard Gas, In *Chemical Warfare Agents: Toxicology and Treatment,* pp 375-407, John Wiley & Sons, Chichester, West Sussex, England.

(105) Brogdon, B. G., Vogel, H., and McDowell, J. D. (2004) *A radiologic atlas of abuse, torture, terrorism, and inflicted trauma*. CRC Press, Boca Raton, FL.

(106) MEDEA. (1997) Ocean dumping of chemical munitions: environmental effects in Arctic Seas, Measurements of Earth Data for Enivronmental Analysis, McLean, VA.

(107) Munro, N. B., Talmage, S. S., Griffin, G. D., Waters, L. C., Watson, A. P., King, J. F., and Hauschild, V. (1999) The sources, fate, and toxicity of chemical warfare agent degradation products. *Environ. Health Perspect.*, *107*, 933-974.

(108) Webb, E. C., and Van Heyningen, R. (1947) The action of British anti-lewisite (BAL) on enzyme systems. *Biochem. J.*, *41*, 74-78.

(109) Wieland, O. (1983) The mammalian pyruvate dehydrogenase complex: Structure and regulation, In *Rev. Physiol. Biochem. Pharmacol.* pp 123-170, Springer, Berlin.

(110) Petrick, J. S., Jagadish, B., Mash, E. A., and Aposhian, H. V. (2001) Monomethylarsonous Acid (MMAIII) and Arsenite: LD50 in Hamsters and In Vitro Inhibition of Pyruvate Dehydrogenase. *Chem. Res. Toxicol.*, *14*, 651-656.

(111) Sahu, C., Pakhira, S., Sen, K., and Das, A. K. (2013) A Computational Study of Detoxification of Lewisite Warfare Agents by British Anti-lewisite: Catalytic Effects of Water and Ammonia on Reaction Mechanism and Kinetics. *J. Phys. Chem. A*, *117*, 3496-3506.

(112) Bayse, C. A., and Antony, S. (2009) Modeling the Oxidation of Ebselen and Other Organoselenium Compounds Using Explicit Solvent Networks. *J. Phys. Chem. A*, *113*, 5780-5785.

(113) Bayse, C. A., and Ortwine, K. N. (2013) Modeling the Glutathione Peroxidase-Like Activity of a Cyclic Seleninate by DFT and Solvent-Assisted Proton Exchange. *Eur. J. Inorg. Chem.*, *2013*, 3680-3688.

(114) Phillips, D. L., Zhao, C., and Wang, D. (2005) A Theoretical Study of the Mechanism of the Water-Catalyzed HCl Elimination Reactions of CHXCl(OH) (X = H, Cl) and HClCO in the Gas Phase and in Aqueous Solution. *J. Phys. Chem. A*, *109*, 9653-9673.

(115) Wu, Z., Ban, F., and Boyd, R. J. (2003) Modeling the Reaction Mechanisms of the Amide Hydrolysis in an N-(o-Carboxybenzoyl)-l-amino Acid. *J. Am. Chem. Soc.*, *125*, 6994-7000.

(116) Kallies, B., and Mitzner, R. (1998) Models of Water-Assisted Hydrolyses of Methyl Formate, Formamide, and Urea from Combined DFT-SCRF Calculations. *J Mol Model*, *4*, 183-196.

(117) Dunning, T. H., and Hay, P. J., Eds. (1977) *Methods of Electronic Structure Theory*, Vol. 3, Plenum Press, New York.

(118) Aposhian, H. V. (1983) DMSA and DMPS-water soluble antidotes for heavy metal poisoning. *Ann. Rev. Pharmacol. Toxicol.*, *23*, 193-215.

(119) Eagle, H., Magnuson, H. J., and Fleischman, R. (1946) Clinical uses of 2,3—dimercaptopropanol (BAL). I. The systemic treatment of experimental arsenic poisoning (mapharsen, lewisite, phenyl arsenoxide) with BAL. *J. Clin. Invest.*, *25*, 451-466.

(120) Barron, E. S. G., Miller, Z. B., Bartlett, G. R., Meyer, J., and Singer, T. P. (1947) Reactivation by dithiols of enzymes inhibited by lewisite. *Biochem. J.*, *41*, 69-74.

(121) Delnomdedieu, M., Basti, M. M., Otvos, J. D., and Thomas, D. J. (1993) Transfer of arsenite from glutathione to dithiols: A model of interaction. *Chem. Res. Toxicol.*, *6*, 598-602.

(122) Goldman, M., and Dacre, J. (1989) Lewisite: Its Chemistry, Toxicology, and Biological Effects, In *Reviews of Environmental Contamination and Toxicology* (Ware, G., Ed.) pp 75-115, Springer New York.

(123) Sokołowski, M. S., and Konopski, L. (2007) Reaction of Lewisite-1 with Alcohols, Diols, and Thiols in Water—A Simple Method of Derivatization of Thiodiglycol. *Phosphorus Sulfur Silicon Relat. Elem.*, *182*, 2311-2327.

(124) Munro, N. B., Watson, A. P., Ambrose, K. R., and Griffin, G. D. (1990) Treating exposure to chemical warfare agents: implications for health care providers and community emergency planning. *Environ. Health Perspect.*, *89*, 205-215.

(125) Modell, W., Gold, H., and Cattell, M. (1946) Clinical uses of 2,3-dimercaptopropanol (BAL). IV. Pharmacologic observations on BAL by intramuscular injection in man. *J. Clin. Invest.*, *25*, 480-487.

(126) Aposhian, H. V., Carter, D. E., Hoover, T. D., Hsu, C.-A., Maiorino, R. M., and Stine, E. (1984) DMSA, DMPS, and DMPA—as arsenic antidotes. *Toxicol. Sci.*, *4*, 58-70.

(127) Inns, R. H., Rice, P., Bright, J. E., and Marrs, T. C. (1990) Evaluation of the Efficacy of Dimercapto Chelating Agents for the Treatment of Systemic Organic Arsenic Poisoning in Rabbits. *Human Exp. Toxicol.*, *9*, 215-220.

(128) Behrens, R., and Bulusu, S. (1992) Recent advances in the thermal decomposition of cyclic nitramines, In *MRS Proc.* p 13, Cambridge Univ Press.

(129) Behrens, R., and Bulusu, S. (1991) Thermal decomposition of energetic materials. 2. Deuterium isotope effects and isotopic scrambling in condensed-phase decomposition of octahydro-1,3,5,7-tetranitro-1,3,5,7-tetrazocine. *J. Phys. Chem.*, *95*, 5838-5845.

(130) Behrens, R. (1990) Thermal decomposition of HMX and RDX: decomposition processes and mechanisms based on STMBMS and TOF of velocity-spectra measurements, In *Chemistry and Physics of Energetic Materials* pp 347-368, Springer.

(131) Behrens, R. (1990) Thermal decomposition of energetic materials: temporal behaviors of the rates of formation of the gaseous pyrolysis products from condensed-phase decomposition of octahydro-1,3,5,7-tetranitro-1,3,5,7-tetrazocine. *J. Phys. Chem., 94,* 6706-6718.

(132) Chakraborty, D., Muller, R. P., Dasgupta, S., and Goddard, W. A. (2000) The mechanism for unimolecular decomposition of RDX (1,3,5-trinitro-1,3,5-triazine), an ab initio study. *J. Phys. Chem. A, 104,* 2261-2272.

(133) Chambers, C. C., and Thompson, D. L. (1995) Further studies of the classical dynamics of the unimolecular dissociation of RDX. *J. Phys. Chem., 99,* 15881-15889.

(134) Zhao, X., Hintsa, E. J., and Lee, Y. T. (1988) Infrared multiphoton dissociation of RDX in a molecular beam. *J. Chem. Phys., 88,* 801-810.

(135) Botcher, T. R., and Wight, C. A. (1993) Transient thin film laser pyrolysis of RDX. *J. Phys. Chem., 97,* 9149-9153.

(136) Wu, C. J., and Fried, L. E. (1997) Ab initio study of RDX decomposition mechanisms. *J. Phys. Chem. A, 101,* 8675-8679.

(137) Liu, M. H., and Zheng, G. F. (2007) Computational study of unimolecular decomposition mechanism of RDX explosive. *J. Theor. Comput. Chem.*, *06*, 341-351.

(138) Suryanarayana, B., Graybush, R., and Autera, J. (1967) Thermal degradation of secondary nitramines: A nitrogen-15 tracer study of HMX. *Chem. Ind. London*, *52*, 2177-2178.

(139) Brill, T. B., and James, K. J. (1993) Kinetics and mechanisms of thermal decomposition of nitroaromatic explosives. *Chem. Rev.*, *93*, 2667-2692.

(140) Brill, T. B., and James, K. J. (1993) Thermal decomposition of energetic materials. 62. Reconciliation of the kinetics and mechanisms of TNT on the time scale from microseconds to hours. *J. Phys. Chem.*, *97*, 8759-8763.

(141) Gonzalez, A. C., Larson, C. W., McMillen, D. F., and Golden, D. M. (1985) Mechanism of decomposition of nitroaromatics. Laser-powered homogeneous pyrolysis of substituted nitrobenzenes. *J. Phys. Chem.*, *89*, 4809-4814.

(142) Fields, E. K., and Meyerson, S. (1967) Arylation by aromatic nitro compounds at high temperatures. *J. Am. Chem. Soc.*, *89*, 724-725.

(143) Cohen, R., Zeiri, Y., Wurzberg, E., and Kosloff, R. (2007) Mechanism of thermal unimolecular decomposition of TNT (2,4,6-trinitrotoluene): a DFT study. *J. Phys. Chem. A*, *111*, 11074-11083.

(144) Ng, W. L., Field, J. E., and Hauser, H. M. (1986) Thermal, fracture, and laser-induced decomposition of pentaerythritol tetranitrate. *J. Appl. Phys.*, *59*, 3945-3952.

(145) Ng, W. L., Field, J. E., and Hauser, H. M. (1976) Study of the thermal decomposition of pentaerythritol tetranitrate. *J. Chem. Soc. Perkin II*, 637-639.

(146) Liu, W.-G., Zybin, S. V., Dasgupta, S., Klapötke, T. M., and Goddard Iii, W. A. (2009) Explanation of the colossal detonation sensitivity of silicon pentaerythritol tetranitrate (Si-PETN) explosive. *J. Am. Chem. Soc.*, *131*, 7490-7491.

(147) Harris, N. J., and Lammertsma, K. (1997) Ab initio density functional computations of conformations and bond dissociation energies for hexahydro-1,3,5-trinitro-1,3,5-triazine. *J. Am. Chem. Soc.*, *119*, 6583-6589.

(148) Cao, Q. (2013) Dinitroamino benzene derivatives: a class new potential high energy density compounds. *J. Mol. Model.*, *19*, 2205-2210.

(149) Wiberg, K. B. (1968) Application of the pople-santry-segal CNDO method to the cyclopropylcarbinyl and cyclobutyl cation and to bicyclobutane. *Tetrahedron*, *24*, 1083-1096.

(150) Chen, Z.-X., and Xiao, H.-M. (2014) Quantum chemistry derived criteria for impact sensitivity. *Prop. Explos. Pyrotech.*, *39*, 487-495.

(151) Xiao, H. (1993) *Molecular orbital theory for nitro compounds*. National Defense Industry Press, Beijing.

(152) Boese, R., Klapötke, T. M., Mayer, P., and Verma, V. (2006) Synthesis and characterization of 1-azido-2-nitro-2-azapropane and 1-nitrotetrazolato-2-nitro-2-azapropane. *Prop. Explos. Pyrotech.*, *31*, 263-268.

(153) Jin, X., Hu, B., Lu, W., Gao, S., Liu, Z., and Lv, C. (2014) Theoretical study on a novel high-energy density material 4,6,10,12-tetranitro-5,11-bis (nitroimino)-2,8-dioxa-4,6,10,12-tetraaza-tricyclo [7,3,0,03,7] dodecane. *RSC Adv.*, *4*, 6471-6477.

(154) Klapötke, T. M., Penger, A., Pflüger, C., Stierstorfer, J., and Sućeska, M. (2013) Advanced open-chain nitramines as energetic materials: heterocyclic-substituted 1,3-dichloro-2-nitrazapropane. *Eur. J. Inorg. Chem.*, *2013*, 4667-4678.

(155) Altenburg, T., Klapötke, Thomas M., Penger, A., and Stierstorfer, J. (2010) Two outstanding explosives based on 1,2-dinitroguanidine: ammonium-dinitroguanidine and 1,7-diamino-1,7-dinitrimino-2,4,6-trinitro-2,4,6-triazaheptane. *Z. Anorg. Allg. Chem.*, *636*, 463-471.

(156) Chavez, D. E., Hanson, S. K., Veauthier, J. M., and Parrish, D. A. (2013) Electroactive explosives: Nitrate ester-functionalized 1,2,4,5-tetrazines. *Angew. Chem.*, *125*, 7014-7017.

(157) Head-Gordon, M., and Head-Gordon, T. (1994) Analytic MP2 frequencies without fifth-order storage. Theory and application to bifurcated hydrogen bonds in the water hexamer. *Chem. Phys. Lett.*, *220*, 122-128.

(158) Zhao, Y., and Truhlar, D. (2008) The M06 suite of density functionals for main group thermochemistry, thermochemical kinetics, noncovalent interactions, excited states, and transition elements: two new functionals and systematic testing of four M06-class functionals and 12 other functionals. *Theor. Chem. Acc.*, *120*, 215-241.

(159) Wodrich, M. D., Corminboeuf, C., Schreiner, P. R., Fokin, A. A., and Schleyer, P. v. R. (2007) How accurate Are DFT treatments of organic energies? *Org. Lett.*, *9*, 1851-1854.

(160) McLean, A. D., and Chandler, G. S. (1980) Contracted Gaussian basis sets for molecular calculations. I. Second row atoms, z=11–18. *J. Chem. Phys.*, *72*, 5639-5648.

(161) Reed, A. E., Curtiss, L. A., and Weinhold, F. (1988) Intermolecular interactions from a natural bond orbital, donor-acceptor viewpoint. *Chem. Rev.*, *88*, 899-926.

(162) Foster, J. P., and Weinhold, F. (1980) Natural hybrid orbitals. *J. Am. Chem. Soc.*, *102*, 7211-7218.

(163) Russell, T., Miller, P., Piermarini, G., and Block, S. (1992) Pressure/temperature/reaction phase diagrams for several nitramine compounds, In *Mater. Res. Soc. Symp. Proc.* p 199, Cambridge Univ Press.

(164) McCrone, W. C. (1950) Crystallographic data. 32. RDX (cyclotrimethylenetrinitramine). *Anal. Chem.*, *22*, 954-955.

(165) Main, P., Cobbledick, R. E., and Small, R. W. H. (1985) Structure of the fourth form of 1,3,5,7-tetranitro-1,3,5,7-tetraazacyclooctane (γ-HMX), $2C_4H_8N_8O_8{\times}0.5H_2O$. *Acta Crystallogr. Sect. C*, *41*, 1351-1354.

(166) Choi, C. S., and Boutin, H. P. (1970) A study of the crystal structure of β-cyclotetramethylene tetranitramine by neutron diffraction. *Acta Crystallogr. Sect. B*, *26*, 1235-1240.

(167) Cady, H. H., Larson, A. C., and Cromer, D. T. (1963) The crystal structure of α-HMX and a refinement of the structure of β-HMX. *Acta Crystallogr.*, *16*, 617-623.

(168) Cady, H. H., and Smith, L. C. (1962) Studies on the polymorphs of HMX, Los Alamos Scientific Laboratory of the University of California, Washington, DC.

(169) McCrone, W. C. (1950) Crystallographic data. 36. Cyclotetramethylene tetranitramine (HMX). *Anal. Chem.*, *22*, 1225-1226.

(170) Cobbledick, R. E., and Small, R. W. H. (1974) The crystal structure of the δ-form of 1,3,5,7-tetranitro-1,3,5,7-tetraazacyclooctane (δ-HMX). *Acta Crystallogr. Sect. B*, *30*, 1918-1922.

(171) Gallagher, H. G., and Sherwood, J. N. (1996) Polymorphism, twinning and morphology of crystals of 2,4,6-trinitrotoluene grown from solution. *J. Chem. Soc., Faraday Trans.*, *92*, 2107-2116.

(172) Golovina, N. I., Titkov, A. N., Raevskii, A. V., and Atovmyan, L. O. (1994) Kinetics and mechanism of phase transitions in the crystals of 2,4,6-trinitrotoluene and benzotrifuroxane. *J. Solid State Chem.*, *113*, 229-238.

(173) Duke, J. R. (1974) Crystallography of TNT, In Explosives Research and Development Establishment, Waltham Abbey, UK.

(174) Cady, H. H., and Larson, A. C. (1975) Pentaerythritol tetranitrate II: its crystal structure and transformation to PETN I; an algorithm for refinement of crystal structures with poor data. *Acta Crystallogr. Sect. B*, *31*, 1864-1869.

(175) Booth, A., and Llewellyn, F. (1947) 163. The crystal structure of pentaerythritol tetranitrate. *J. Chem. Soc.*, 837-846.

(176) Barnes, J., and Golnazarians, W. (1987) The 1: 1 complex of pyrene with 2, 4, 6-trinitrotoluene. *Acta Crystallogr. Sect. C, 43*, 549-552.

(177) Carper, W. R., Davis, L. P., and Extine, M. W. (1982) Molecular structure of 2,4,6-trinitrotoluene. *J. Phys. Chem., 86*, 459-462.

(178) Clarkson, J., Smith, W. E., Batchelder, D. N., Smith, D. A., and Coats, A. M. (2003) A theoretical study of the structure and vibrations of 2,4,6-trinitrotolune. *J. Mol. Struct., 648*, 203-214.

(179) Sorescu, D. C., Rice, B. M., and Thompson, D. L. (1999) Molecular packing and molecular dynamics study of the transferability of a generalized nitramine intermolecular potential to non-nitramine crystals. *J. Phys. Chem. A, 103*, 989-998.

(180) Millar, D. I. A., Marshall, W. G., Oswald, I. D. H., and Pulham, C. R. (2010) High-pressure structural studies of energetic materials. *Crystallogr. Rev., 16*, 115-132.

(181) Simpson, R. L. F., M. F. (1995) LLNL Small-Scale Drop-Hammer Impact Sensitivity Test, Department of Energy, Springfield, VA.

APPENDIX

Reactant, transition state, and product complexes in Chapters 2 and 3 were obtained through conformational searches and manual scans of selected reaction coordinates with visualization by a graphical user interface. Reactant complexes were constructed from scratch using GaussView software. SAPE networks consist of three- or four-water molecules to connect deprotonation and protonation sites to mimic solvent interaction. Water molecules were positioned to maximize hydrogen interaction in order for proton exchange to occur. Depending upon how far apart these sites were positioned, a linear three- or square four-water network was used. The square cluster (shown in Figure S1) reduces strain introduced in longer interactions which would otherwise result in higher activation barriers. A manual conformational search was performed on the reactant complex to find the unconstrained structure with the lowest total energy (E). From this conformation, a bond (i.e. H-O) was selected as the reaction coordinate and constrained and manually stretched/shortened (Figure S1) in increments of 0.01-0.5 Å until the maximum total energy on the potential energy curve (Figure S2) and one imaginary frequency (in the form of the motion of a proton transfer) was found. From this structure, a full, unconstrained transition state optimization was performed. The lowest energy product complex structure was found by the full, unconstrained optimization of a point along the scan of the reaction coordinate past the maximum/transition state structure. For the transition state and product complexes in each step in the reaction, ΔH, ΔG, and $\Delta G+\Delta G_{solv}^{\ddagger}$ were calculated from H, G, and the

solvation correction, G_{solv}, obtained from PCM calculations, of the reactant, transition state, and product complex (i.e., $\Delta H_{prod}=H_{prod}-H_{react}$).

Figure S1. A manual scan of a selected reaction coordinate.

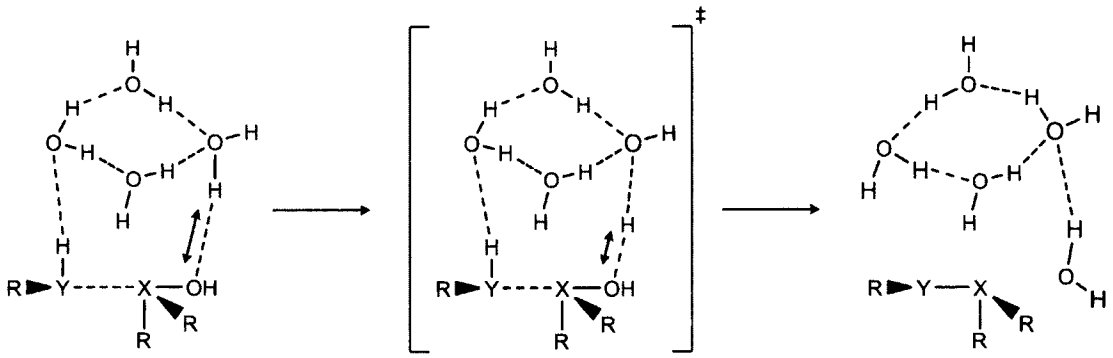

Figure S2. Potential energy curve.

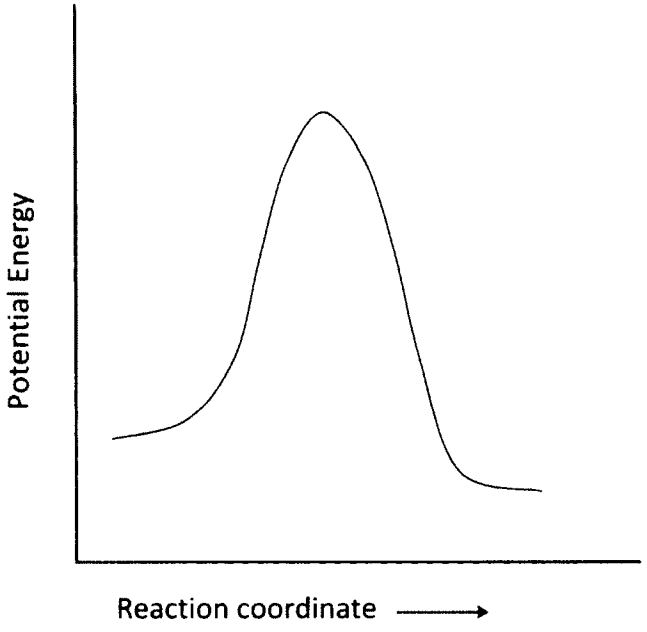

VITA

LENORA HARPER

EDUCATION

Ph.D. in Chemistry, Old Dominion University, Department of Chemistry & Biochemistry, 4541 Hampton Blvd. Norfolk, VA 23529, August 2015

B.S. Chemistry, Christopher Newport University, Newport News, VA, May 2009

PROFESSIONAL EXPERIENCE

Teaching Assistant for lecture and laboratory courses (ODU), Fall 2009-2014

Graduate Research Assistant with Dr. Craig A. Bayse (ODU), Spring 2010-Summer 2011

Newport News Shipbuilding Summer Intern, 2006-2009

PUBLICATIONS

Harper, L. K.; Antony, S.; Bayse, C. A. Thiol reduction of selenite and arsenite: DFT modeling of pathways to an As-Se bond. *Chem. Res. Toxicol.*, **2014**, *27*, 2119–2127.

Bayse, C. A.; Harper, L. K.; Ming, J. L.; Pike, R. D. Theoretical insights into the effect of amine and phosphine decoration on the photoluminescence of copper(I) and silver(I) coordination polymers. *Dalton Trans.*, **2014**, *43*, 11243-11251.

PRESENTATIONS

"Optimization of DFT Methods and Basis Sets to Investigate the Decomposition of Novel HEDMs." L. K. Harper and C. A. Bayse. Virginia Space Grant Consortium Student Research Conference, Hampton University, VA, April 11, 2014.

"SAPE modeling on biological reactions of sulfur and arsenic." Lenora K. Harper and Craig A. Bayse, Regional ACS Meeting, Richmond, VA, October 25-28, 2011.